

## Review—Radiation Damage in Wide and Ultra-Wide Bandgap Semiconductors

To cite this article: S. J. Pearton *et al* 2021 *ECS J. Solid State Sci. Technol.* **10** 055008

View the [article online](#) for updates and enhancements.



## Review—Radiation Damage in Wide and Ultra-Wide Bandgap Semiconductors

S. J. Pearton,<sup>1,\*</sup> Assel Aitkaliyeva,<sup>1</sup> Minghan Xian,<sup>2</sup> Fan Ren,<sup>2,\*</sup> Ani Khachatryan,<sup>3</sup>  
Adrian Ildefonso,<sup>3</sup> Zahabul Islam,<sup>4,a</sup> Md Abu Jafar Rasel,<sup>4</sup> Aman Haque,<sup>4</sup>  
A. Y. Polyakov,<sup>5</sup> and Jihyun Kim<sup>6,\*\*</sup>

<sup>1</sup>Department of Materials Science and Engineering, University of Florida, Gainesville, Florida 32611, United States of America

<sup>2</sup>Department of Chemical Engineering, University of Florida, Gainesville FL 32611, United States of America

<sup>3</sup>US Naval Research Laboratory, Washington, DC 20375, United States of America

<sup>4</sup>Department of Mechanical Engineering, The Pennsylvania State University, University Park, Pennsylvania 16802, United States of America

<sup>5</sup>National University of Science and Technology MISiS, 4 Leninsky Ave, Moscow, 119049, Russia

<sup>6</sup>Department of Chemical and Biological Engineering, College of Engineering, Korea University, Seoul, Republic of Korea

The wide bandgap semiconductors SiC and GaN are already commercialized as power devices that are used in the automotive, wireless, and industrial power markets, but their adoption into space and avionic applications is hindered by their susceptibility to permanent degradation and catastrophic failure from heavy-ion exposure. Efforts to space-qualify these wide bandgap power devices have revealed that they are susceptible to damage from the high-energy, heavy-ion space radiation environment (galactic cosmic rays) that cannot be shielded. In space-simulated conditions, GaN and SiC transistors have shown failure susceptibility at ~50% of their nominal rated voltage. Similarly, SiC transistors are susceptible to radiation damage-induced degradation or failure under heavy-ion single-event effects testing conditions, reducing their utility in the space galactic cosmic ray environment. In SiC-based Schottky diodes, catastrophic single-event burnout (SEB) and other single-event effects (SEE) have been observed at ~40% of the rated operating voltage, as well as an unacceptable degradation in leakage current at ~20% of the rated operating voltage. The ultra-wide bandgap semiconductors Ga<sub>2</sub>O<sub>3</sub>, diamond and BN are also being explored for their higher power and higher operating temperature capabilities in power electronics and for solar-blind UV detectors. Ga<sub>2</sub>O<sub>3</sub> appears to be more resistant to displacement damage than GaN and SiC, as expected from a consideration of their average bond strengths. Diamond, a highly radiation-resistant material, is considered a nearly ideal material for radiation detection, particularly in high-energy physics applications. The response of diamond to radiation exposure depends strongly on the nature of the growth (natural vs chemical vapor deposition), but overall, diamond is radiation hard up to several MGy of photons and electrons, up to 10<sup>15</sup> (neutrons and high energetic protons) cm<sup>-2</sup> and >10<sup>15</sup> pions cm<sup>-2</sup>. BN is also radiation-hard to high proton and neutron doses, but h-BN undergoes a transition from sp<sup>2</sup> to sp<sup>3</sup> hybridization as a consequence of the neutron induced damage with formation of c-BN. Much more basic research is needed on the response of both the wide and ultra-wide bandgap semiconductors to radiation, especially single event effects.

© 2021 The Electrochemical Society ("ECS"). Published on behalf of ECS by IOP Publishing Limited. [DOI: [10.1149/2162-8777/abfc23](https://doi.org/10.1149/2162-8777/abfc23)]

Manuscript submitted March 30, 2021; revised manuscript received April 21, 2021. Published May 17, 2021. *This paper is part of the JSS Focus Issue on Solid State Electronic Devices and Materials.*

Power losses within electrical control systems represent a significant waste of energy. As an example, within a decade, over 80% of all US electricity is predicted to flow through power electronics. Since currently almost 2/3 of this power is lost to heat in switching and transmission losses, as shown in Fig. 1,<sup>1</sup> there is a need for more efficient power electronic devices and circuits with smaller form-factors than existing Si-based systems.<sup>1-18</sup> The main limitations of Si devices at high voltages are high power losses, low switching frequency and poor high-temperature performance.<sup>2-5,7-21</sup> Wide bandgap (WBG, gaps from ~2 eV up to ~3.5 eV) and ultra-wide bandgap (UWBG, gap >3.5 eV) semiconductors are promising in view of this increasing electrification of society. Among these, SiC and GaN are already commercialized<sup>2-5,7-9,11,14</sup> while the UWBG materials, diamond, Ga<sub>2</sub>O<sub>3</sub>, high Al-AlGa<sub>N</sub> (up to pure AlN) and BN are in various stages of development.<sup>6,13,14,16-21</sup>

SiC and GaN and the developing ultra-wide bandgap materials are ideal platforms for the new generation of power electronics thanks to the combination of excellent transport properties and the high critical electric field. Figure 2 shows a summary of the lattice constants and energy bandgaps of a large number of elemental and compound semiconductor families. This gives an idea of which ternary compounds can be grown lattice-matched to commercially available substrates, which reduces dislocation densities due to

mis-matched growth. The advantage of having larger bandgaps relative to Si is shown in Fig. 3, where it is seen that the lowering of the on-state resistance of power switching devices as a function of breakdown voltage is very significant as the bandgap of the semiconductor is increased.<sup>2-7</sup> This has major advantages in terms of reducing power switching losses.

Beyond applications such as more electric power grids, and autonomous vehicles, there is tremendous interest in radiation-hard electronics for space-borne applications. Spacecraft operating beyond Earth's magnetosphere are subject to space weather, including the solar wind, which is a constant barrage of radiation and charged particles capable of severely damaging the physical and electrical components of a spacecraft.<sup>22,23</sup> The charged particles from the solar wind get trapped inside the Earth's magnetosphere, forming the Van Allen radiation belts that further expose transiting spacecraft to concentrated levels of charged particles and high-energy radiation.<sup>22,23</sup> New systems are already using increasingly complex and diverse materials (compared to the traditional Si-based systems) and devices in the post-Moore electronics landscape.<sup>24</sup> Defense systems have to transition to lower-cost sensors (capable of rapid and effective decision making, while being complex and unpredictable) integrated on distributed platforms (that are agile and resilient) to improve global persistent awareness.<sup>22,23</sup>

In future defense systems which incorporate devices and ICs intended for use in high-traffic areas (e.g. low-Earth orbit), identifying all failure mechanisms in electrical components will be one of the main challenges. As we assimilate more complex device architectures, understanding of their radiation response (e.g. to single particle-induced displacement damage), damage production

\*Electrochemical Society Fellow.

\*\*Electrochemical Society Member.

<sup>a</sup>Present address: Department of Materials Science and Engineering, University of Wisconsin-Madison, Madison, Wisconsin 53706, United States of America.

<sup>z</sup>E-mail: [spcar@mse.ufl.edu](mailto:spcar@mse.ufl.edu)

## U.S. energy consumption by source and sector, 2019

(Quadrillion Btu)

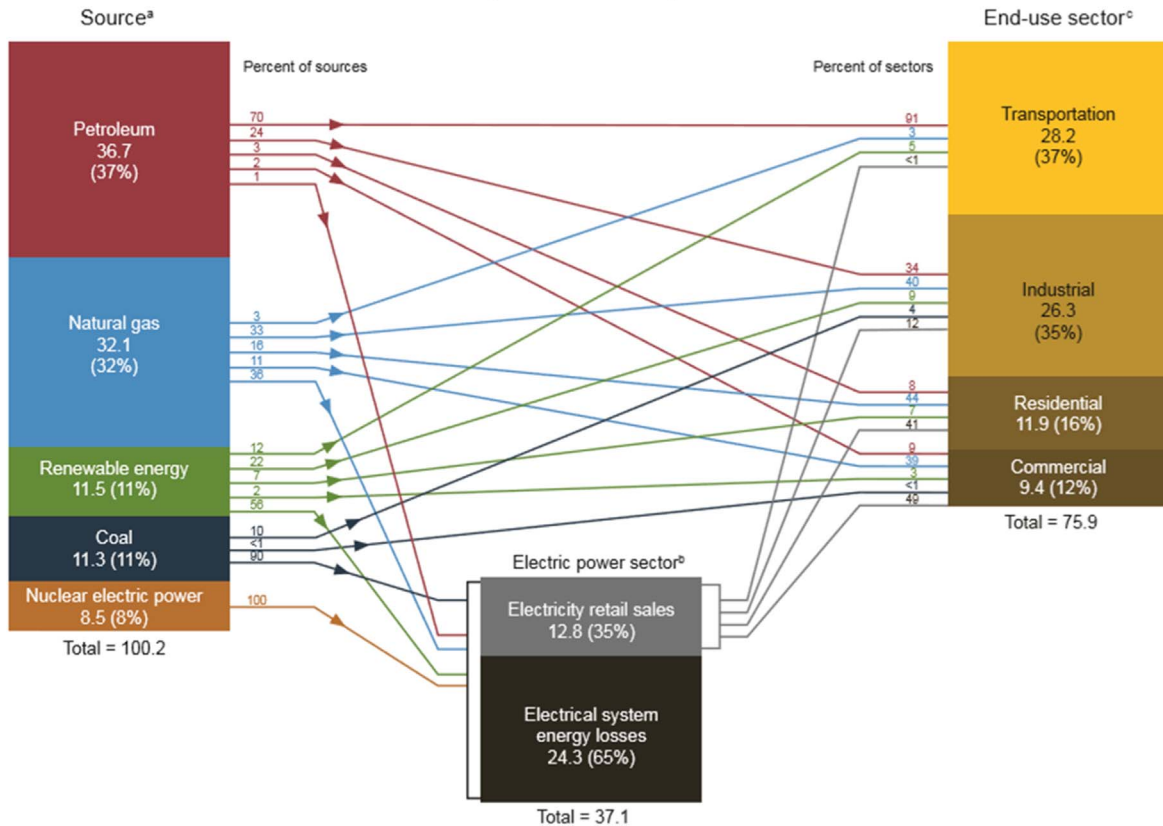


**Figure 1.** Details of the energy consumption in the United States in 2019 by source and sector (adapted from US Energy Information Administration, <https://www.eia.gov/energyexplained/us-energy-facts/>).

mechanisms, and damage thresholds (in terms of flux, radiation type, and energy) will be critical to their implementation in advanced aircraft and space-borne systems and better lifecycle predictions for swarm-based or distributed platforms.<sup>25–34</sup> Such understanding cannot be attained without a renewed emphasis on the ability to test devices in charged particle, photon, and/or neutron environments that appropriately stress vulnerable devices and coupling experimental data with sophisticated modeling and simulation.

In critical defense applications and autonomous vehicles, there is an increasing transition from high-voltage Si power devices, which are limited in current ratings and power efficiency, to commercial wide bandgap (WBG) power devices. SiC and GaN power devices are now used in the automotive, wireless, and industrial power markets, but their adoption into space and avionic applications is hindered by their susceptibility to permanent degradation and catastrophic failure from heavy-ion exposure.<sup>13,35–67,68,69</sup>

The European Space Agency is currently employing a new generation of space communication systems based on GaN HEMTs in its Proba-V satellite, so far delivering greatly improved data transmission rates and working reliability,<sup>33</sup> as well as in its Biomass satellite due for launch in 2024. Efforts to space-qualify WBG power devices have revealed that they are susceptible to damage from the high-energy, heavy-ion space radiation environment (galactic cosmic rays) that cannot be shielded.<sup>63–67</sup> Higher voltage devices are more susceptible to these effects;<sup>70–155</sup> as a result, to date, there are space-qualified GaN transistors now available, but limited to 300 V. Recent radiation testing of 600 V and higher GaN transistors has shown failure susceptibility at about 50% of the rated voltage, or less.<sup>155</sup>

Similarly, SiC power devices have undergone several generations of advances commercially, improving their overall reliability, but

catastrophically fail at less than 50% of their rated voltage.<sup>93–101</sup> SiC components have demonstrated susceptibility to radiation damage under heavy-ion single-event effects testing, reducing their utility in the space galactic cosmic ray (GCR) environment. In SiC-based Schottky diodes, catastrophic single-event burnout (SEB) and other single-event effects (SEE) have been observed at ~40% of the rated operating voltage, as well as an unacceptable degradation in leakage current at ~20% of the rated operating voltage.<sup>63–67,93–101</sup> SEE caused by terrestrial cosmic radiation (neutrons) have also been identified by industry as a limiting factor for the use of SiC-based electronics in aircraft.<sup>65,93</sup> Currently, small satellite applications require a Total Ionizing Dose (TID) resilience of 30 krad (Si) and Single Event Latch-up (SEL) hardened up to 80 MeV cm<sup>2</sup> mg<sup>-1</sup> linear energy transfer.<sup>155,156</sup> Since SiC and GaN are much more mature technologies than the ultra-wide bandgap semiconductors,<sup>157–175</sup> it can be anticipated that the latter will require a detailed understanding of the effects of space radiation before systems based on them can be reliably deployed.

Radiation hardening comes with a cost. As with Si power MOSFETs, electrical performance will suffer from hardening techniques. The two primary failure radiation damage concerns in current generations of electronics for space applications are (i) Single event upset, in which incident ionizing radiation results in the flipping of a bit from 0 to 1 or vice versa. While this may be a problem for data loss or operation, it does not lead to permanent damage of the device and (ii) Total dose failure, in which irradiation leads to the creation of a sufficient density of defects. These then lead to degradation of the electrical properties to the point of permanent failure.

The current verification, testing and qualification methodologies for radiation effects (ASTM, JEDEC, Mil STD and ESCC) are all at

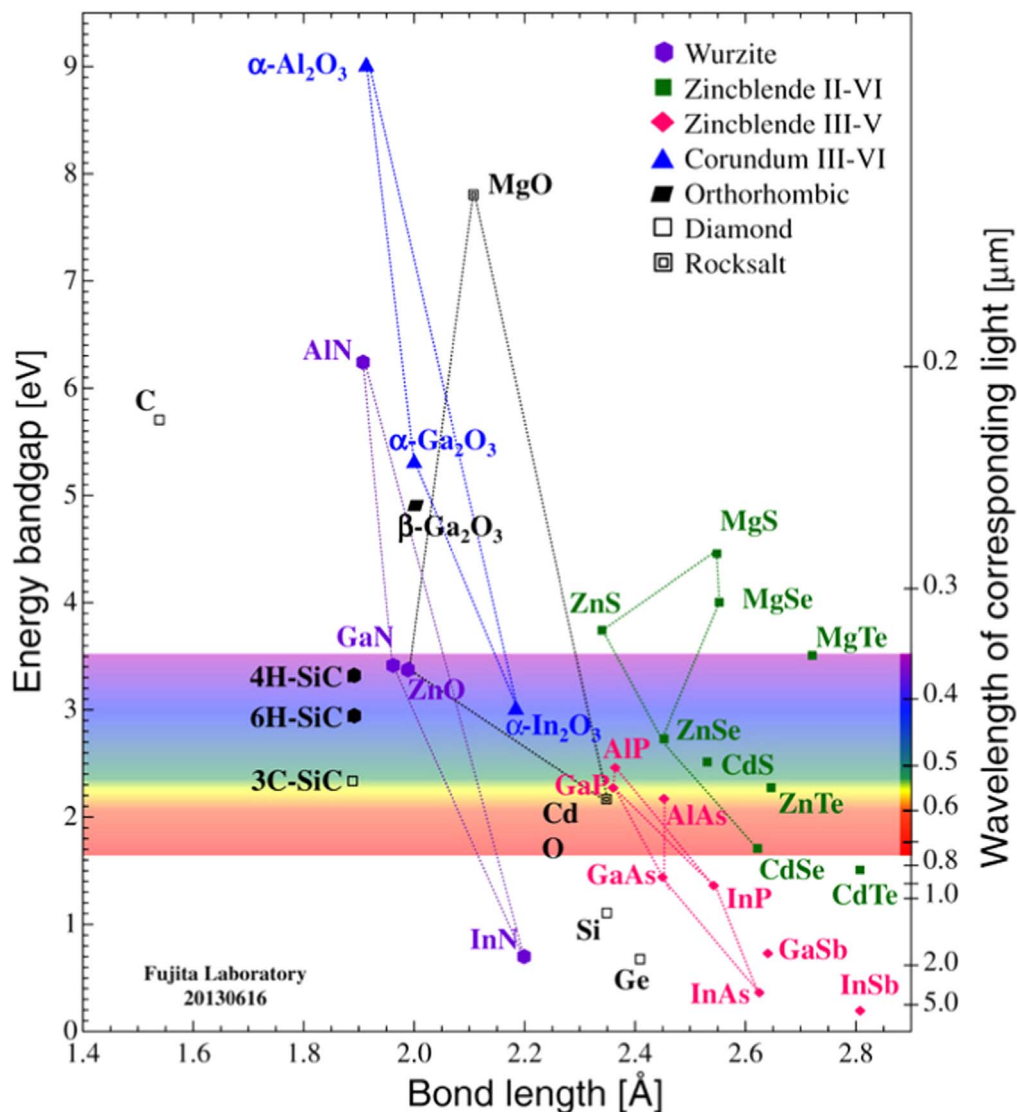


**Figure 2.** Relationship between energy bandgap and bond length for various compound semiconductors promising for practical applications (adapted from Fujita, Japanese Journal of Applied Physics, **54**, 030101 (2015), copyright IOP. All of the wide bandgap and ultra-wide bandgap materials of interest here can be grown in bulk form.

least 7 years old and need urgent updating. To do so, the fundamental science. As an example, understanding the degradation mechanism provides may be used eventually to harden the vulnerable technology. The performance gap between commercial and radiation-hardened electronics continues to widen, increasing the incentive to use commercial technologies and the corresponding need to test the SEE performance of these parts to ensure they will function as required. The rapid development of electronics technologies in the post-scaling era has led to device topologies and materials different than those used in conventional planar CMOS. Now each new generation of microelectronics technology can differ significantly from the last, and each generation will need to be evaluated for SEE performance to see if it is a promising candidate for future radiation hardening to rogue galactic cosmic rays. The possibility of single event effects in critical avionics drives the need for redundancy.

In terms of modelling, there's a disconnect in the length scales of much is what is available, because the existing multi-scale approaches are not relevant at both smaller and longer length scales. On the device side, TCAD models are used to simulate changes in devices, while GEANT-4 and equivalent are used for large-scale detectors and other systems. This is an area where much progress can be made.

In this paper we will review radiation damage results for SiC, GaN, high-Al AlGaIn, Ga<sub>2</sub>O<sub>3</sub>, diamond and BN. Each of these materials have aspects unique to itself, beyond the generally strong atomic bonding that makes them less susceptible to displacement damage than Si.

### Total Dose and Single Event Upset

The two primary failure radiation damage concerns in current generations of electronics for space applications are,<sup>25–30</sup>

- Single event upset, in which incident ions result in an ionized trail of charge that can flip a bit from 0 to 1 or vice versa. While this may be a problem for data loss or operation, it does not lead to permanent damage of the device.
- Total dose failure, in which irradiation by gamma rays or high energy particles leads to the creation of a sufficient density of displacement damage (structural defects, including vacancies, interstitials, defect clusters, dislocation cluster loops). These defects then lead to degradation of the electrical properties to the point of permanent failure.

The next generation of device structures will be sufficiently small (a typical volume being  $30 \times 30 \times 30$  nm) that the damage resulting



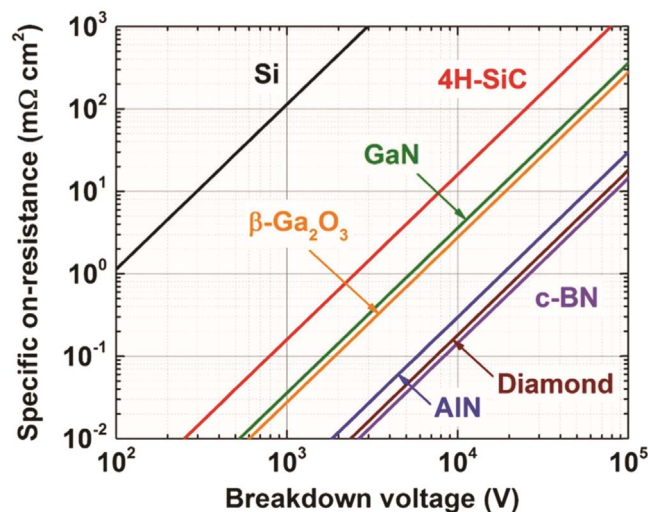


**Figure 3.** Specific on-resistance vs breakdown voltage for different semiconductors. The on-resistance decreases with increasing bandgap, allowing higher breakdown operation at the same on-resistance or lower on-resistance at the same breakdown voltage.

from a single gamma ray or high energy ion can result in the failure of the device. We term this a single event failure. A point on nomenclature is also salient here—“upsets” are usually related to memory or logic circuits, whereas single event “effects” are more generally applied to single devices as well as circuits. Defect generation and charge transition are the fundamental mechanisms that govern radiation effects and mitigation in electronic materials.

**Damage processes in semiconductors.**—In addition to growth-related defects, radiation-induced defects in materials are produced through electronic (ionizing and charge transfer) effects and nuclear displacement damage.<sup>166,176–194</sup> There may also be damage to insulators used to apply voltage to the gate of a transistor structure. Inelastic linear energy transfer (LET) to the electronic structure (also known as electronic stopping power) from high energy particles, as well as from photons (X-rays and lasers), results in the creation of energetic electrons (i.e., ionization and excitation) that initially dissipate their energy in a cascade of electron-electron energy transfers (superheating) that result in the production of electron-hole (e)–(h) pairs (the time scale is  $<fs$ );<sup>34–39</sup> (2) the transfer of much of this energy via electron-phonon coupling to the atomic structure creating a local thermal spike (the time scale is  $<300 fs$ ); and (3) the formation of localized electronic excitations that can rupture or change the nature of covalent/ionic bonds, enhance defect and atomic mobilities and increase system energy.

One common issue in radiation damage studies is the nomenclature used and how it differs between device engineers and materials scientists and physicists.<sup>32</sup> Especially in detector and space physics, a different terminology is employed for the same quantities. Linear Energy Transfer (LET) is used for total or electronic stopping power. Since in this field the interest is mostly in MeV and GeV charged particles, the two are essentially the same. Similarly, what is commonly termed the Non Ionizing Energy Loss (NIEL) is the same thing as Nuclear Stopping Power used by ion implantation specialists.

In the initial stages of entering the material under irradiation, the incident ions lose energy mainly by electronic stopping, and move in fairly straight paths, although, for very light ions like H and He, the occasional nuclear collisions with heavy target atoms are so strong that the path can be better likened with a random walk.<sup>195</sup> When the ion has slowed down sufficiently, the collisions with nuclei become more and more probable, finally dominating the slowing down. When atoms receive significant recoil energies, they will be removed from their lattice positions, and produce a cascade of further

collisions in the lattice. These collision cascades are the main cause of damage production. Ions create mainly point defects, which are most commonly created right after irradiation. A point defect is defined as a defect without a significant extent in space and differs from line or volume defects that extend in 1, 2 or 3 dimensions, such as dislocations, stacking faults or precipitates, respectively.

The final stage of irradiation almost always includes many-body collisions between atoms.<sup>195</sup> Due to both nuclear and electronic stopping, the high-energy ions and recoils slow down and eventually reach thermal velocities ( $<1 eV$ ). At this stage they collide with several atoms at the same time, known as many-body collisions. Athermal defect recombination occurs when atoms regenerate back into a perfect crystal, i.e. do not produce lattice damage. The efficient recombination of displaced atoms is a strong function of the temperature at which the irradiation is carried out and also depends strongly on the bandgap and type of atomic bonding within the semiconductor.<sup>25,27–30</sup>

The strength of chemical bonds is of the order of  $\sim 2\text{--}5 eV$ . Hence radiation where the particles have an energy high enough to break chemical bonds and leave them permanently broken, damages a material. In metals and usually in semiconductors, essentially all this displacement damage is produced by the atomic recoils regardless of whether they come from  $\alpha$ ,  $\beta$ ,  $\gamma$  particles or neutrons. For protons, electronic stopping dominates over nuclear for all energies. Damage is very commonly given in the form of displacements-per-atom (dpa). The damage recovery after irradiation often occurs in distinct stages with increasing annealing temperature.

A critical issue for many devices is the transient ionization-induced processes associated with high LET particles and intense pulses of photons.<sup>25,27–30,34</sup> The confined dimensions ( $<10 nm$  radius in the case of charged particles), short time frame (0.1 to 100 ps) and extreme temperatures (1000–10,000 degrees) of the ionization-induced thermal spike defy simple dynamics or thermally activated approaches, but they have a strong influence on defect production and device degradation.<sup>27–30</sup> Even the strike of a single ion causes the creation of free charge carriers and atomic defects through ionization in the electrical devices that can temporarily or permanently disrupts its functionality, as in single event effects and single event burnout, respectively. At high ion energies and intense lasers (or gamma pulses), the energy transferred to the atomic structure via electron-phonon coupling can cause an intense transient thermal spike that can cause a shock wave, local heating or melting followed by a fast quench, and defect formation.<sup>27–30</sup> In the case of single ions, the thermal spike has a cylindrical geometry, while for an X-ray burst or lasers, the thermal spike has a planar geometry relative to the surface.

Another source of degradation in electronic devices is the charge trapping in the gate dielectric and its interface with the semiconductor layer, which can also lead to lowering of the insulator breakdown voltage. Defects formed during manufacturing or by irradiation, as well as interfaces, may trap electrons and holes, resulting in charged defect states. At low ion fluences ( $<10^{12}$  ions  $cm^{-2}$ , depending on ion energy and mass), damage regions from individual ions do not overlap, and the response to ions of specific mass and energy can be characterized in situ or ex situ using the known density of ion events and a variety of techniques,<sup>44,196–211</sup> such as scanning transmission electron microscopy (STEM) to determine the nature and concentration of damage/defects. While amorphous tracks are not expected to form in the wide bandgap and ultra-wide bandgap semiconductors, local compositional variations, defects and strain fields are expected along the ion trajectories. A displaced interstitial will undergo many collisions until its energy is reduced to values corresponding to lattice temperature. In process some interstitials remain in stable configuration and some anneal immediately.

**Why use GaN, SiC, AlN, Ga<sub>2</sub>O<sub>3</sub> diamond and BN?**—The properties of these semiconductors are compared to those of Si in Table 1.<sup>2–6</sup> The new materials offer a higher electric breakdown field

**Table I. Properties of wide and ultra-wide bandgap semiconductors compared to Si.**

Material	Bandgap (eV)	Dielectric constant, $\epsilon$	Electron mobility, $\mu$ (cm <sup>2</sup> V <sup>-1</sup> s <sup>-1</sup> )	Critical Electric Field, $E_C$ (MV cm <sup>-1</sup> )	Baliga figure of merit, $\epsilon\mu E_C^3$
Si	1.1	11.7	1350	0.3	1
4H-SiC	3.3	9.7	1000	2.5	340
GaN	3.4	9.0	1200	3.3	870
$\beta$ -Ga <sub>2</sub> O <sub>3</sub>	4.6–4.9	10	200	8	3400
$\alpha$ -Ga <sub>2</sub> O <sub>3</sub>	5.2–5.3	10	200	8.5	3800
Diamond	5.5	5.5	2800	10	4500
2H-AlN	6.1	8.5	300	10	8500
h-BN	5.97	5.0	50	~10	8000
c-BN	6.4	5.0	<200	~12	10000

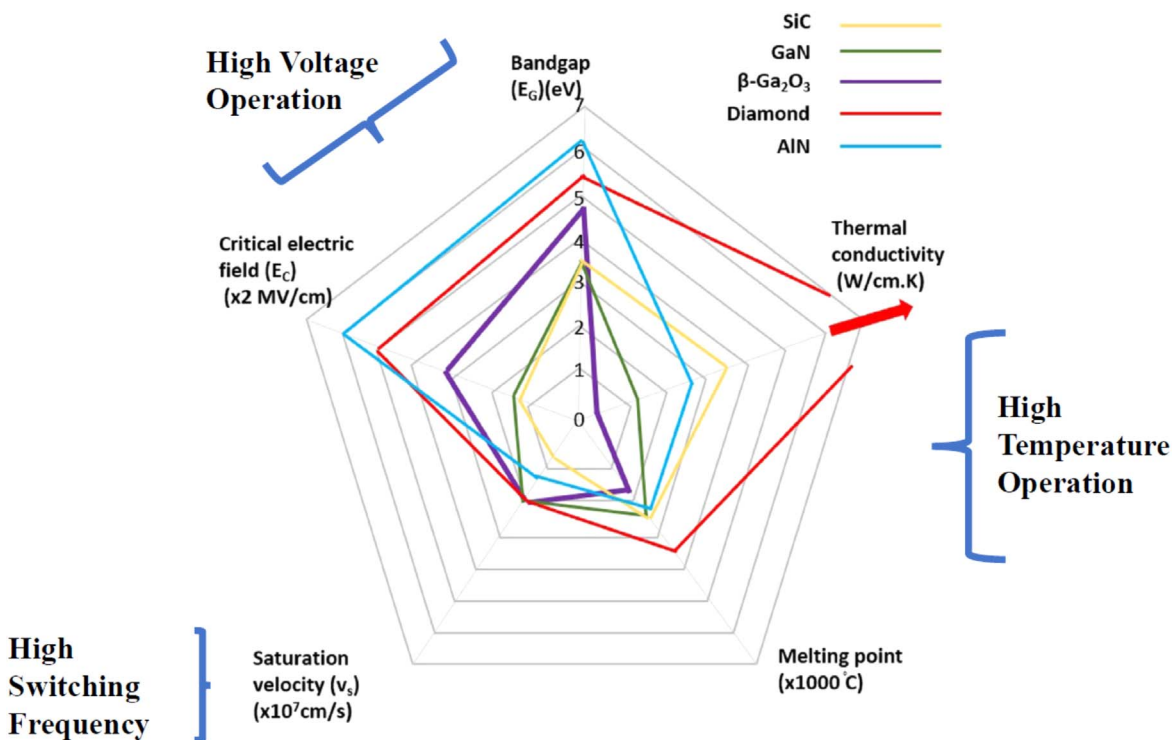


**Figure 4.** Spider diagram of different parameters of wide and ultra-wide bandgap semiconductors and relative capabilities under different operating conditions of interest.

that enable greater voltage blocking capability, thinner layers and allows deeper doping concentration. Therefore, it results in lower conduction losses and a low drift resistance than Si devices. The high critical fields allow the operation of power switching devices at much high voltages and currents than with Si and the wide bandgap allows for higher temperature operation. The Baliga figure of merit is a commonly employed metric to evaluate the potential for different semiconductors in power device applications.<sup>2-6</sup> The magnitude of this parameter depends on the third power of critical electric field, which in turn depends on the bandgap to a power of roughly 2.7.<sup>16</sup> Therefore, an increase in bandgap makes a huge impact on the power figure of merit. Figure 4 shows a spider diagram of the relative magnitude of various parameters of interest in the most common wide bandgap and ultra-wide bandgap semiconductors for high power, high temperature device applications. Materials such as SiC, diamond and AlN have excellent thermal conductivities and are well-suited to high temperature applications, whereas GaN and Ga<sub>2</sub>O<sub>3</sub> have low thermal conductivities and require extensive thermal management approaches to achieve stable operation at high powers. Similarly, the wider the bandgap, the more potential the particular semiconductor has for high voltage applications.

Wide-bandgap (WBG, gaps from  $\sim 2$  eV up to  $\sim 3.5$  eV, e.g., GaN and 4H-SiC) and ultrawide-bandgap (UWBG, gap  $> 3.5$  eV, e.g., AlGa<sub>2</sub>N, AlN, c-BN, and  $\beta$ -Ga<sub>2</sub>O<sub>3</sub>) semiconductors are deployed or considered for use in high-power, high-frequency devices for defense and military applications such as radar, counter-measures, high altitude aircraft, sensors and imaging systems onboard satellites, data communication and networking guided weapons, jamming, and spacecraft.

More energy efficient power electronics could improve the efficiency and reliability of power grids and industrial processes. The newer semiconductors allow robust power electronics that withstand higher operating temperatures, have increased durability, a smaller form factor, and higher efficiency. Low cost, efficient power electronics will lead to more affordable electric and hybrid-electric transportation, greater integration of renewable power sources, and higher efficiency electric motors for use in heavy

industries and consumer appliances. Improved power electronics could yield up to a 20% reduction in U.S. electricity consumption.

The semiconductors have different lattice symmetries, as shown in Fig. 5 for diamond (top), hexagonal GaN (center) and 4H-SiC (bottom). These materials have predominantly covalent bonding, while the two main polymorphs of Ga<sub>2</sub>O<sub>3</sub>, namely the  $\beta$  and  $\alpha$  forms also have a strong component of ionic bonding. The type of bonding also influences the breakdown mechanism of the semiconductor under single event upset conduction. Typically covalently bonded materials will fail by an avalanche breakdown caused by impact ionization,<sup>4</sup> resulting from the acceleration of carriers by the electric field, to the point where they have sufficient kinetic energy to ionize atoms in the semiconductor host. By contrast, in ionically bonded materials, the possibility of other dielectric breakdown mechanisms occurring is significant.<sup>51</sup> The effects of bond-breaking and the possible high-temperature anharmonicity of phonons on breakdown are unexplored in Ga<sub>2</sub>O<sub>3</sub>. For example, it would be important to distinguish between avalanche breakdown and time-dependent destructive dielectric breakdown if trap-assisted processes are insignificant. The structure of the two main polymorphs are shown in Fig. 6 and their characteristics in Table II.

To give some idea of the current state of the art, SiC inverters involving SiC MOSFETs with SiC Schottky diodes) prototypes have been demonstrated with a blocking voltage of 6.5 kV/200 A and 15 kV/10 A.<sup>5,9,11,14</sup> SiC products use packaging approaches that allow operating temperatures to 210 °C, a significant increase since SiC devices became available commercially in 2001. SiC unipolar diodes and SiC MOSFETs are now available with breakdown voltages of 1700 and 3300 V, respectively and current handling capabilities up to 750 A and some manufacturers are working on a next generation of 6500 V devices.<sup>14</sup>

GaN was first commercialized for light-emitting diodes and laser diodes in the mid-1990s prior to the market for power electronics. GaN has a relatively high electron mobility which allows high switching frequencies, but a major drawback is the low thermal conductivity, similar to that of Si, requiring advanced thermal management approaches. GaN power devices are currently limited

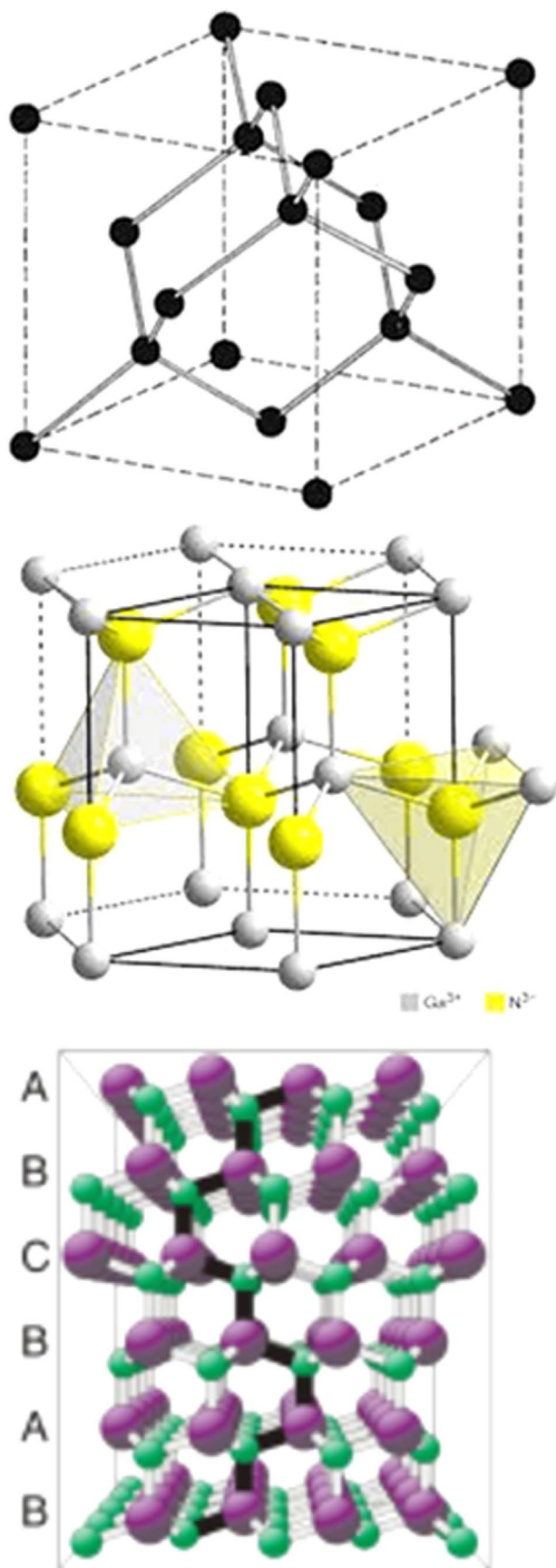


**Figure 5.** Crystal structure of diamond (top), GaN (center) and 4H-SiC (bottom).

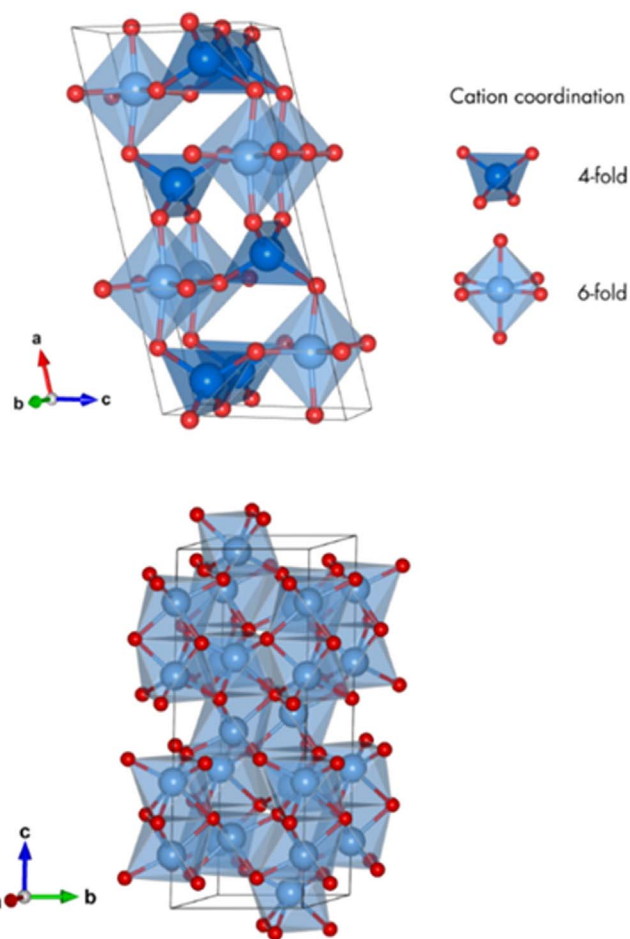


**Figure 6.** Stick-and-ball model of monoclinic  $\beta$ -Ga<sub>2</sub>O<sub>3</sub> (top) and rhombohedral  $\alpha$ -Ga<sub>2</sub>O<sub>3</sub> (bottom). The gallium atoms are indicated as blue spheres and the oxygen atoms as red ones.

to 650 V, 150 A, with rapid development of 1200 V, 180 A devices.<sup>3,4,8</sup> GaN power devices have similar prices to SiC devices for the same characteristics.<sup>9,15</sup> A lower price for GaN devices is possible because they can be developed on Si substrates. The displacement energies for Ga and N atoms during irradiation are estimated to be 20.5 and 10.8 eV, respectively.<sup>2,4</sup>

We include AlN and in particular high Al content AlGaN as an addition to GaN technology. Pure AlN has a wider bandgap than diamond (6.2 eV), with excellent thermal stability, high thermal conductivity (340 W m<sup>-1</sup> K<sup>-1</sup>) and large critical electric field (12 MV cm<sup>-1</sup>). The development of growth processes for large area, high quality substrates and doping processes is needed. The AlGaN alloy has exceptional properties, combining advantages of GaN and AlN, such as high bandgap (3.4–6.0 eV), high breakdown field, high electron mobility ( $\sim 1000$  cm<sup>2</sup> V<sup>-1</sup> s<sup>-1</sup>), high saturation velocity ( $> 10^7$  cm s<sup>-1</sup>), and facile n-type doping. Future AlGaN development needs include larger area substrates, reproducible growth quality and low resistance contacts.<sup>16</sup>

For Ga<sub>2</sub>O<sub>3</sub>, the  $\beta$ -phase is the most common of the five polymorphs ( $\alpha$ ,  $\beta$ ,  $\gamma$ ,  $\delta$  and  $\epsilon$ ).<sup>6,13,20,55</sup> This most stable beta crystal structure is attracting interest for power electronics devices and is stable through the whole temperature range up to the melting point.  $\beta$ -Ga<sub>2</sub>O<sub>3</sub> has a C-centered monoclinic unit cell with space group C2/m. Large diameter bulk crystals of this material are commercially available and the wide bandgap makes it promising for both power electronics and solar-blind UV detection,<sup>46–51,68</sup>  $\beta$ -Ga<sub>2</sub>O<sub>3</sub> has a large bandgap of approximately 4.9 eV and an estimated critical electric



**Table II.** Basic parameters for the two most common polymorphs of Ga<sub>2</sub>O<sub>3</sub> (after Hassa, dissertation on Epitaxy and Physical Properties of Group-III Sesquioxide Alloys, University of Leipzig, 2021).

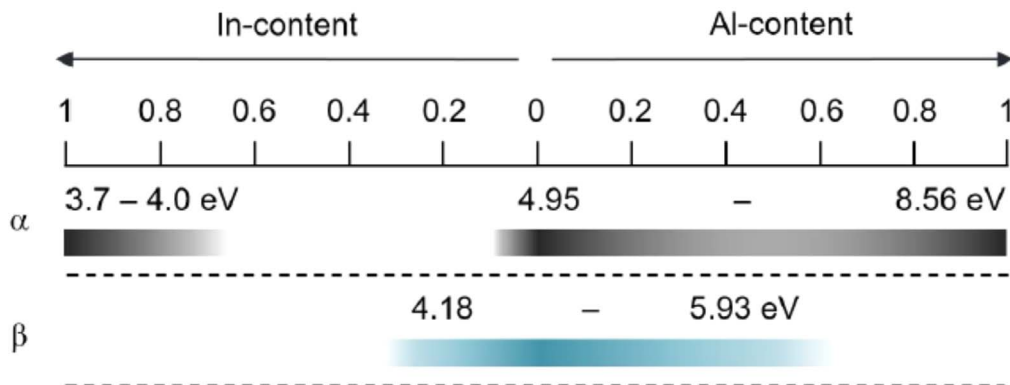
Polymorph	Space group	Lattice constants (Å)	Oh: Td	Optical bandgap (eV)
$\beta$ monoclinic	C2/m	a = 12.214 b = 3.037 c = 5.798 $\beta = 103.83^\circ$	1:1	4.6–4.9
$\alpha$ rhombohedral	R3c	a = 4.9825 c = 13.433	1:0	5.2–5.3

field ( $E_C$ ) strength of  $8 \text{ MV cm}^{-1}$ . The large bandgap of  $\beta$ -Ga<sub>2</sub>O<sub>3</sub> allows high temperature device operation and this large critical field allows high voltage operation (relative to maximum breakdown) and the most common device structure reported to date has been Schottky rectifiers.<sup>6,13,55</sup> This material also has potential in devices with low power loss during high frequency switching in the GHz regime and is found to be radiation-hard.<sup>44,208–222</sup> Similarly, Ga<sub>2</sub>O<sub>3</sub>-based photodetectors are attracting interest for their promise as truly solar-blind deep ultraviolet (UV),<sup>46–51,68</sup> photodetectors exhibiting cut-off wavelengths below 280 nm. These would have applications in detection of UV wavelengths for military applications, air purification, space communication, ozone-layer monitoring and flame sensing.

The materials of the group-III sesquioxides, which include indium, gallium, and aluminum oxide (In<sub>2</sub>O<sub>3</sub>, Ga<sub>2</sub>O<sub>3</sub>, Al<sub>2</sub>O<sub>3</sub>), are characterized by ultra-wide bandgap energies and an appearance transparent to the human eye with absorption edges deep into the ultraviolet (UV) band.<sup>46–51,68</sup> The possibility of alloying these materials among each other enables precisely tunable bandgap energies in a broad range and thus the realization of applications where a tailored bandgap is required, such as solar blind UV-photodetectors. The sesquioxides have different thermodynamically stable crystal structures, namely, the corundum-structured  $\alpha$ -Al<sub>2</sub>O<sub>3</sub>, the monoclinic  $\beta$ -Ga<sub>2</sub>O<sub>3</sub> or the cubic bixbyite In<sub>2</sub>O<sub>3</sub> structure, respectively. As a result, phase separation can occur in the alloys observable at certain cation compositions. Ga<sub>2</sub>O<sub>3</sub> can also be alloyed with In or Al to form ternary alloys, namely (In<sub>x</sub>Ga<sub>1-x</sub>)<sub>2</sub>O<sub>3</sub> and (Al<sub>x</sub>Ga<sub>1-x</sub>)<sub>2</sub>O<sub>3</sub>, whose bandgaps span a very large range.<sup>6,51</sup> The current miscibility limits and the range of optical bandgaps achieved in these two alloy systems are presented in Fig. 7. The phase limits vary for the different crystal structures and confine the potential bandgap ranges. At this stage, there is essentially no information on the response of these alloys to radiation. The  $\alpha$  polytype has an even larger bandgap and might find a niche role in ultra-high power devices.<sup>6</sup>

Diamond has high breakdown field, high thermal conductivity, high electron mobility and low dielectric constant.<sup>19</sup> Synthetic electronic grade single crystals became commercially available after the establishment of epitaxial growth by chemical vapor deposition (CVD) in the 2000's. Single crystal diamond has a cubic symmetry, consisting of two interpenetrating face-centered cubic lattices, one displaced from the other by  $a_0(1/4, 1/4, 1/4)$ , where  $a_0$  is the lattice constant.<sup>19</sup> The short sp<sup>3</sup> C-C bonds are 154 pm in length, giving a lattice constant 356.7 pm. The density of diamond is  $3.52 \text{ g cm}^{-3}$ , with an atomic density of  $1.76 \times 10^{23} \text{ cm}^{-3}$ , the highest of any solid. Pure diamond also has the highest thermal conductivity at room temperature of any material,  $2300 \text{ W m}^{-1} \text{ K}^{-1}$ , more than 15 times that of Si. It is also the hardest of all naturally-occurring materials and is typically high purity with a band gap of 5.47 eV. The practical application of diamond devices has been constrained by lack of availability of single crystal wafer with large size, dislocation free, and low resistivity. It has a high atomic displacement energy (42 eV atom<sup>-1</sup>) and a high stability to radiation. The classification of different types of diamond depending on their nitrogen and boron content is given in Table III.

BN is the second highest hardness material and has low chemical reactivity.<sup>4</sup> Boron nitride (BN) does not exist in nature and is therefore produced synthetically, two different BN structures are well-known: The wurtzite type w-BN and the rhombohedral phase r-BN.<sup>4</sup> The former is the high-pressure phase of h-BN and c-BN can be formed when r-BN is exposed to high pressure. However, both wBN and r-BN are metastable phases at ambient conditions, and the growth of single-crystalline bulk material is realizable only in h-BN as well as c-BN. In its cubic structure (c-BN), BN is isoelectronic with diamond and both n-type (Si) and p-type doping (Be) are possible. c-BN has a bandgap of 6.4 eV, and a breakdown field  $\sim 15 \text{ MV cm}^{-1}$ . It also has the second-highest theoretical thermal conductivity of all materials (2145 W/(m.K) for isotopically pure material). However, the development of BN is slow due to the need for improved growth processes with high quality and large area.

**Figure 7.** Approximate miscibility limits and corresponding optical bandgap energies for the  $\alpha$  and  $\beta$  polymorphs of the group-III sesquioxides. (adapted from Anna Hassa dissertation Epitaxy and Physical Properties of Group-III Sesquioxide Alloys, Der Fakultät für Physik und Geowissenschaften der Universität Leipzig).

**Table III. Type classifications of diamond according to their IR absorption spectra (after Matthew Dale, Color Centers in Diamond, thesis University of Warwick, 2015).**

Type	Subtype	Description	References
I		N conc > 1ppm	
	Ia	N present in aggregated form	
	IaA	N <sub>S</sub> -N <sub>S</sub> pairs dominate	a)
	IaB	N <sub>S</sub> -N <sub>V</sub> pairs dominate	b,c)
	IaA/B	both N <sub>S</sub> -N <sub>S</sub> and N <sub>S</sub> -N <sub>V</sub> pairs present	
II	Ib	N <sub>S</sub> centers dominate	d)
		No N or B detectable	
	IIa	No N detectable	
	IIb	B conc>N conc	e,f)

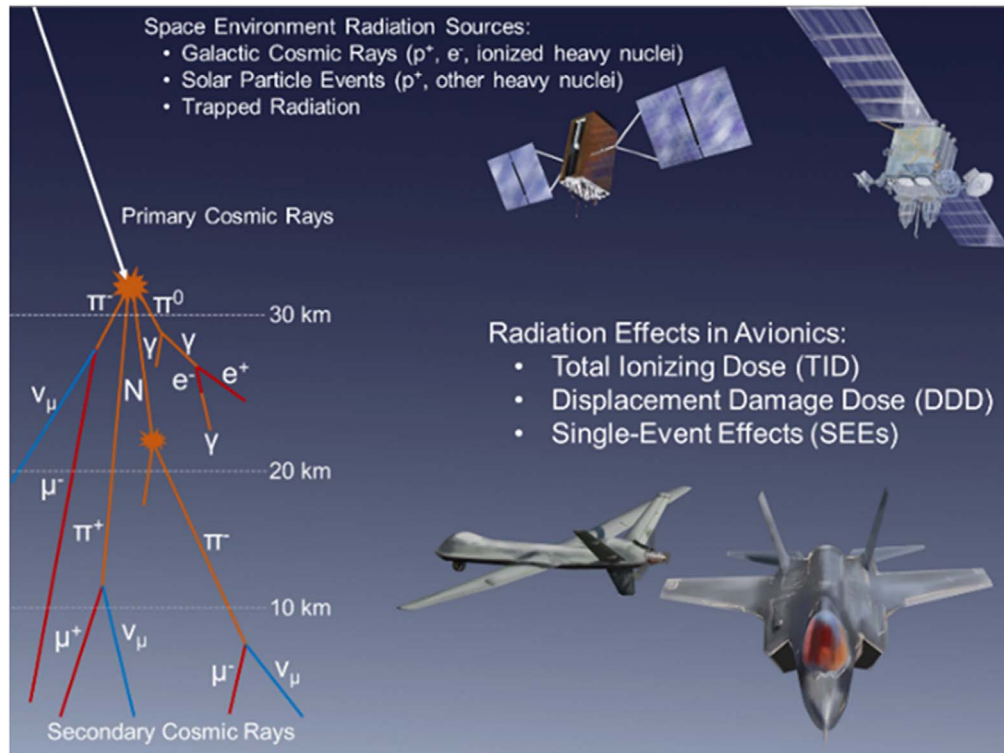
a) G. Davies, Journal of Physics C: Solid State Physics **9**, L537 (1976). b) J. Loubser, J. A. Van Wyk, Diamond conference, Reading (unpublished), 1981. c) R. Jones, P. R. Briddon, S. "Oberg, Philosophical Magazine Letters **66**, 67–74 (1992). d) R. M. Chrenko, H. M. Strong, R. E. Tuft, Philosophical Magazine **23**, 313–318 (1971). e) A. T. Collins, A. W. S. Williams, Journal of Physics C: Solid State Physics **4**, 1789–1800 (1971). f) R. M. Chrenko, Physical Review B **7**, 4560 (1973).

**Damage mechanisms.**—The electronics in aircraft and spacecraft are especially vulnerable to radiation effects due to the lack of shielding from the atmosphere. A schematic is shown in Fig. 8 for aircraft. The avionics in such aircraft are transitioning to having part of their systems being GaN and SiC and so it is important to understand the effects of radiation exposure on these materials. Figure 9 shows a schematic of the main damage mechanisms in wide bandgap semiconductors for protons and alpha particles.<sup>111</sup> This is basically the NIEL or displacement damage, creating primary point defects and their complexes.<sup>57,223–230</sup> These typically act as traps or recombination centers with energy levels in the bandgap and these can reduce the effective carrier concentration by trapping electrons or holes and removing them from the conduction process in the semiconductor. This increase in charged defects also decreases the carrier mobility, with this having an even large effect on

conductivity than the reduction in carrier concentration. This leads to a key measure of the magnitude of the radiation damage induced, namely, the carrier removal rate.<sup>133</sup> This is a parameter that can be used to compare the relative amount of change expected in a semiconductor exposed to different types of radiation. In the case of MOS gate devices, there is also the possibility of damage to the gate insulator. While MOS gates are the standard in Si devices, the absence of high-quality gate oxides on most of the wide bandgap and ultra-wide bandgap semiconductors means that only SiC routinely uses this approach and most devices use metal gates.<sup>222–239</sup>

**Range and energy loss parameters.**—The main component of radiation in solar flares and in the Van Allen belts are high energy protons and alpha particles, so these are often used to determine the effects of radiation on GaN and SiC devices. Figure 10 shows the average distance, the projected range, travelled by protons and alpha particles in these materials as a function of ion energy. The higher density of GaN leads to shorter projected ranges. For comparison, the results for diamond are shown in Fig. 11.

The total stopping power can be then written as  $S = dEdx = S_n + S_e$ . The simulated (from the SRIM code)<sup>193</sup> energy loss profiles for two different energies of protons in GaN and SiC are shown in Fig. 12. Similar data is shown in Fig. 13 for the energy losses of 1.8 and 40 MeV protons in diamond. These energies span the range of typical protons available in Van de Graaff generators and the inner Van Allen belt approximately 2,000 miles above the terrestrial surface consists largely of highly energetic protons, with energy exceeding 30 MeV. The outer Van Allen belt contains charged particles from atmospheric and solar origin. The solar wind is composed mainly of He<sup>+</sup> ions, while the protons in the outer belt have much lower energies than those in the inner belt. The maximum loss occurs near the end of the ions range as the ions slow down and undergo more NIEL. Note that the energy loss near the surface is actually lower for higher energy ions, meaning that devices such as High Electron Mobility Transistors whose active regions are close to the surface will be less affected by high energy ions. Note that most of the energy loss under these conduction is due to ionization and heat production as the ions slow down.

**Figure 8.** Schematic of radiation effects on aircraft.

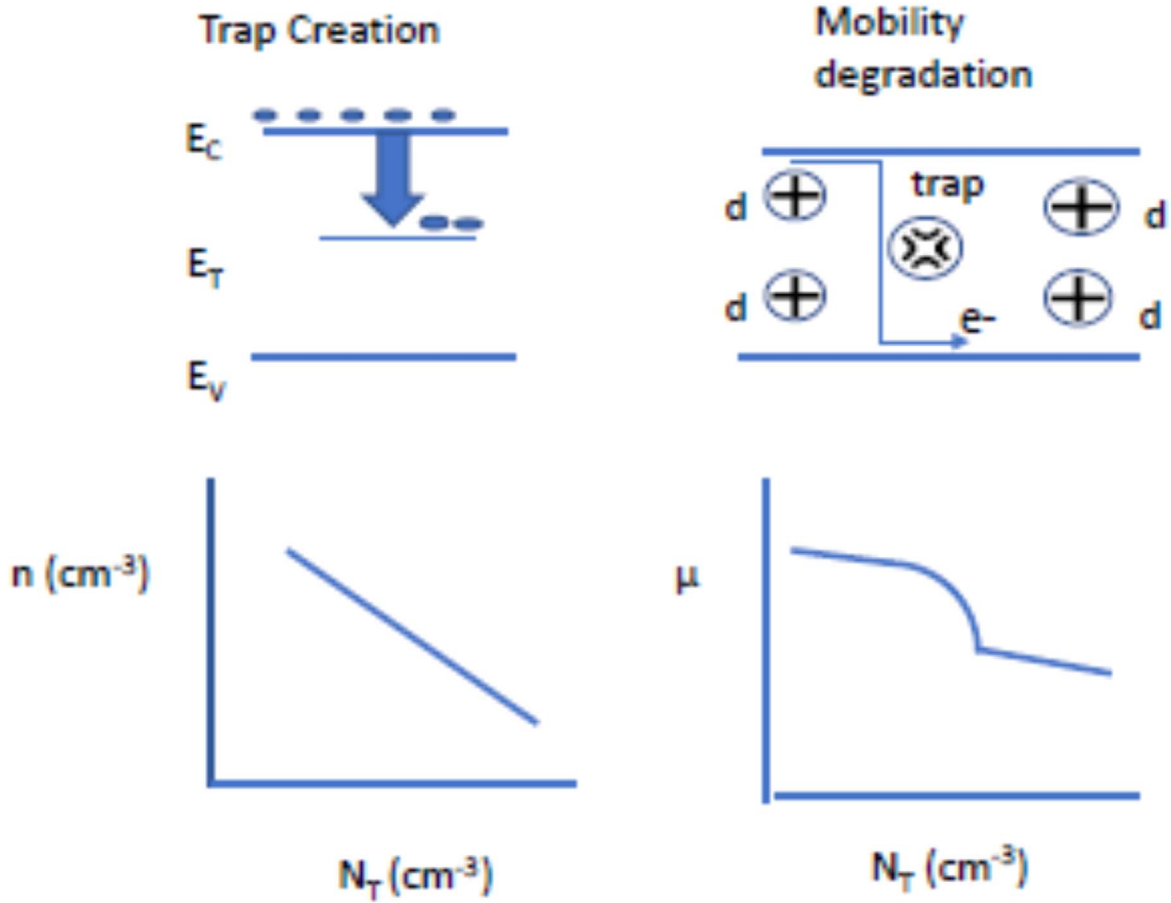


**Figure 9.** Main device bulk degradation mechanisms by irradiation in doped semiconductors. Displacement damage produces traps that reduce the effective carrier concentration and also degrade mobility because of the increase in charged scattering centers.

Figure 14 shows the variation with energy of energy loss to both ionization and nuclear stopping (non-ionizing energy loss) for both protons and alpha particles in diamond, showing that electron stopping (ionization and heat production) dominates. The same trends are observed for all the wide bandgap and ultra-wide bandgap materials discussed in this paper.

For protons and other ions, the Total Ionizing Dose (TID) is equal to the product of Linear Energy Transfer (LET) and fluence. The tolerance of devices is expressed in TID (Gray or Rad; 1 Gy = 100 rad = 1 J kg<sup>-1</sup>). Most modern CMOS circuitry usually can withstand >10–20 krad ionizing doses (good for low Earth orbits below the Van Allen belts) due to their thinner gate oxides. TID or total ionization damage is cumulative damage as in insulators wherein electrons and holes produced by ionization are fixed and charged regions are induced; i.e., the material does not return to its initial state. In the context of silicon devices with gate oxide layers, the changes induced are due to energy deposition in form of ionization from electrons, gamma and X-rays (via photoelectric, Compton and pair-production), protons and ions and leads to threshold Shifts, excess leakage current and functional failures. Figure 15 shows the LET as a function of energy in diamond, while Fig. 16 shows the same dependences for GaN for different ions, calculated from TRIM. We also show the LET values for these same ions in h-BN in Fig. 17.

Non-ionizing energy loss (NIEL), often called Displacement Damage (DD) depends on the particle fluence  $\Phi$  (number of ions cm<sup>-2</sup>). The units of NIEL are (keV cm<sup>2</sup> g<sup>-1</sup>) and the DD dose is given by the product of NIEL  $\times \Phi$ .<sup>32</sup> This produces a cumulative bulk damage, i.e., a disordered crystal lattice long term effects with permanent changes in semiconductor properties due to energy deposition in non-ionizing interactions by neutrons, protons, ions (especially

slow ones near end of range) and electrons. The production of defects results in progressive device degradation, which may be similar to TID effects. The displacement energy threshold determines the defect concentration for incident electrons with energies <750 keV.<sup>25–30,32</sup> The concentration  $N_d$  of Frenkel pairs

$$N_d = A.E/2E_d,$$

where A is displacement efficiency, E is energy given up in creating atomic displacements. For higher energy or heavier particles, this approximation is less accurate. The effects scale with particle fluence and often the tolerance of devices is expressed in fluence of 1 MeV neutron equivalents. For Si, the risk begins at fluence >10<sup>11–12</sup> 1 MeV neutrons cm<sup>-2</sup>.

Most levels introduced by radiation in semiconductors are deep in the bandgap.<sup>57,227–239</sup> When ionized, they compensate the intentionally incorporated doping and reduce the free carrier concentration according to the formula  $n = n_0 - K_N N_T \Phi$  where  $n_0$  is the initial concentration of electrons,  $n$  is the electron concentration after irradiation, and  $K_N$  is the carrier removal rate.  $K_N$  is proportional to the introduction rate of acceptor centers  $d N_T/d\Phi$  and the probability of their occupancy by electrons (the deeper the level, the higher the probability of its occupancy). The creation of deep traps by irradiation reduces the carrier concentration and also introduces additional charge scattering centers that reduce the carrier mobility. An example of energy losses to the different processes for protons in GaN of a variety of energies typical of solar flares and the Van Allen belts is given in Table IV.

SEE occur when a single ionizing particle deposits enough energy in a sensitive volume to cause spontaneous damage in a device or circuit.<sup>80–88</sup> There is a threshold amount of ionization

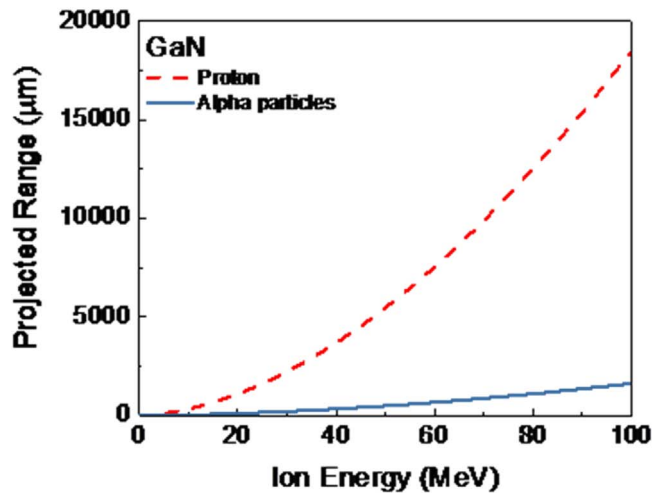
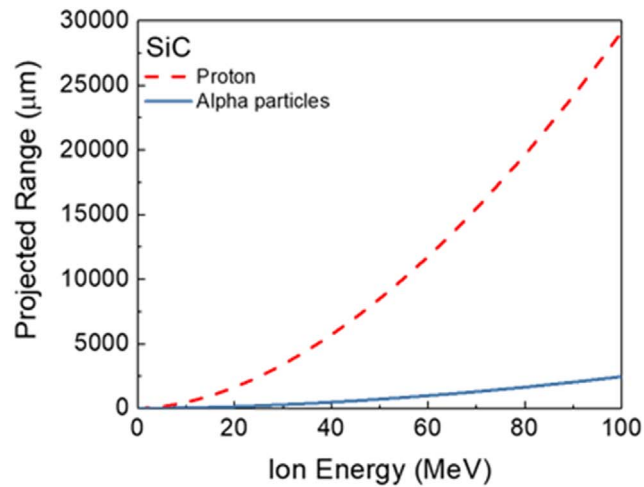


**Figure 10.** Projected range of  $^1\text{H}^+$  and  $^4\text{He}^+$  in 4H SiC (top) and GaN (bottom) calculated from SRIM.

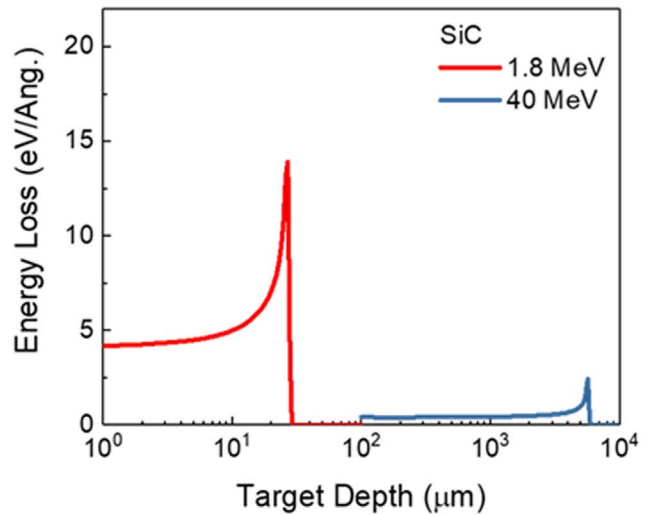
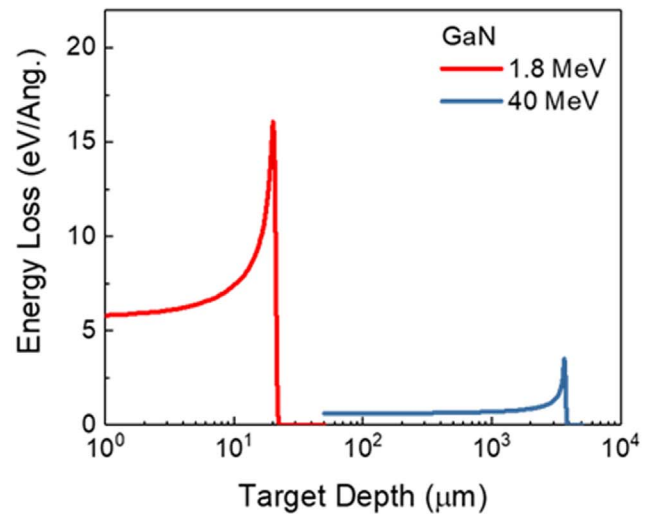


**Figure 12.** Energy loss as a function of depth for 1.8 MeV and 40 MeV protons in GaN (top) and 4H-Si (bottom), calculated from SRIM.

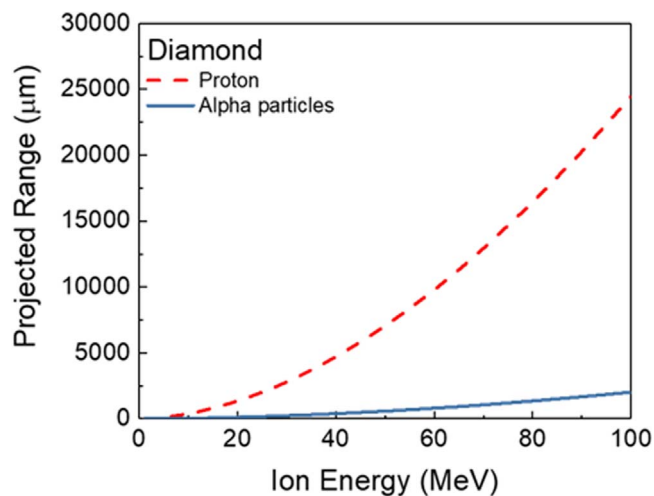


**Figure 11.** Projected range of  $^1\text{H}^+$  and  $^4\text{He}^+$  in diamond calculated from SRIM.

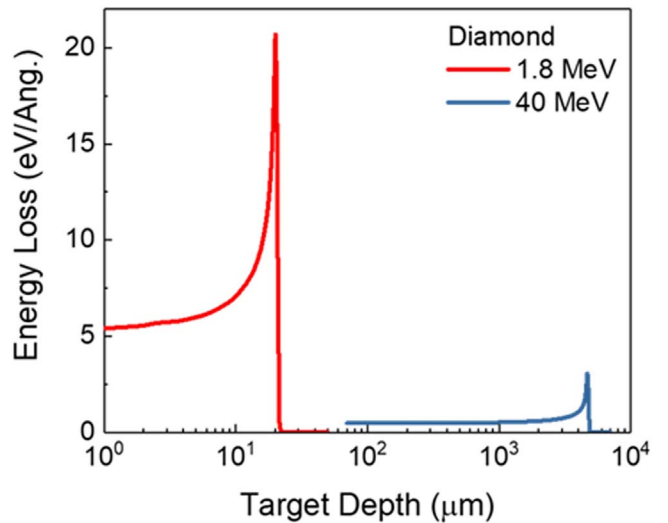


**Figure 13.** Energy loss as a function of depth for 1.8 MeV and 40 MeV protons in diamond calculated from SRIM.

needed to cause this disruption due to heavy ions (e.g. primary galactic high charge and energy cosmic rays), neutrons, protons, and heavier ions. The effects on electronics depend on technology and design, but may include destructive SEE, burnout and data

corruption. The rate of these effects scale with particle flux and the tolerance of devices is expressed in cross-section ( $\text{cm}^2$ ) = NSEE/fluence. This cross section is determined as a function of LET and



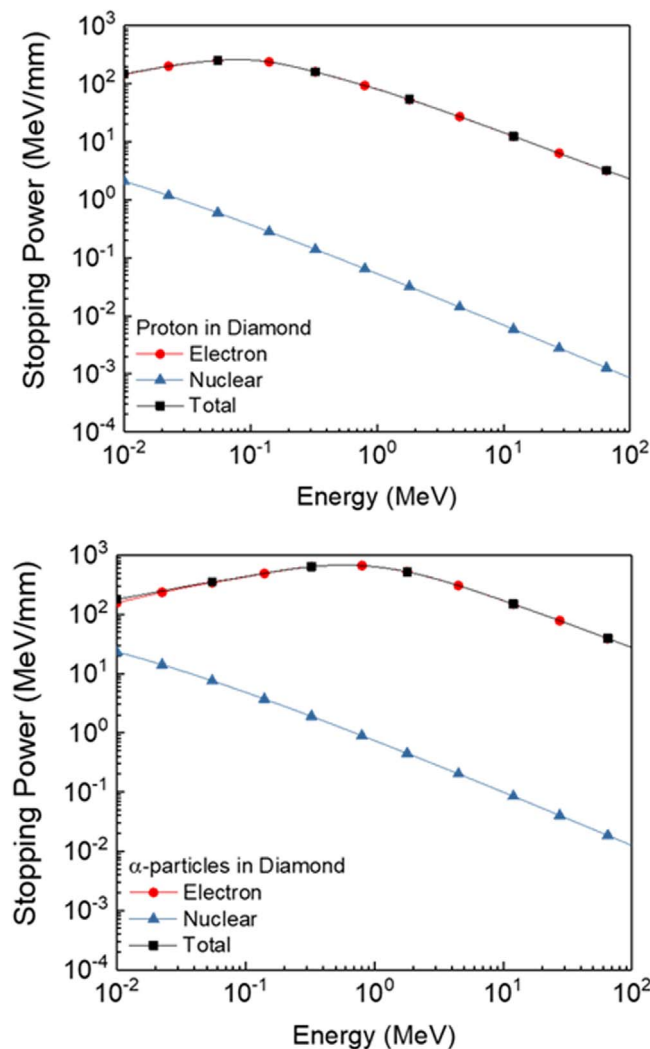


**Figure 14.** Electronic and nuclear stopping powers for  $^1\text{H}^+$  (top) and  $^4\text{He}^+$  (bottom) in diamond.

depends on the specific ionization level of the impinging ion for energy transfers  $> \text{LET}_{\text{threshold}}$ . Table V provides a summary of the characteristics of SEE, TID and NIEL in semiconductors.

There has been an extensive literature on total dose and single event upsets in both SiC and GaN.<sup>63–67,70,71–155,240,156–210</sup> In the following sections we provide a summary of the reported results.

**SiC.**—A study of total dose neutron irradiation at conditions that might be encountered in nuclear reactor on SiC carrier concentration and electron mobility as a function of 1 MeV equivalent neutron fluence in SiC ( $\Phi_{1\text{MeV}}$ , SiC equivalent) found that resistivity doubled for  $\Phi_{1\text{MeV}}$ , SiC eq =  $2.7 \times 10^{16} \text{ cm}^{-2}$ , while the resistivity recovered (i.e. decreased) by only 8% from its post-irradiation values after 2 h, 175 °C annealing.<sup>71–75</sup> The carrier concentration in the irradiated area decreased linearly with  $\Phi_{1\text{MeV}}$ , SiC eq, with a carrier removal rate of  $\sim 48.5 \pm 6.3 \text{ cm}^{-1}$ . Within experimental uncertainty, the carrier concentration recovered to its pre-irradiation values after 2 h of annealing at 175 °C.<sup>71–75</sup> Concurrently, the Hall mobility decreased linearly with  $\Phi_{1\text{MeV}}$ , SiC equivalent dose and this mobility was further decreased by 27% after annealing at 175 °C for 2 h.<sup>71–75</sup>

Radiation effects in commercial 1200 V, 24 A SiC Power MOSFETs exposed to  $\text{Co}^{60}$  TID effects at room temperature and 125 °C found that these components remained operational after a radiation dose of more than 100 krad.<sup>43–45,63,67,92</sup> The gamma ray irradiation gave rise to changes in current-voltage and capacitance-voltage characteristics.

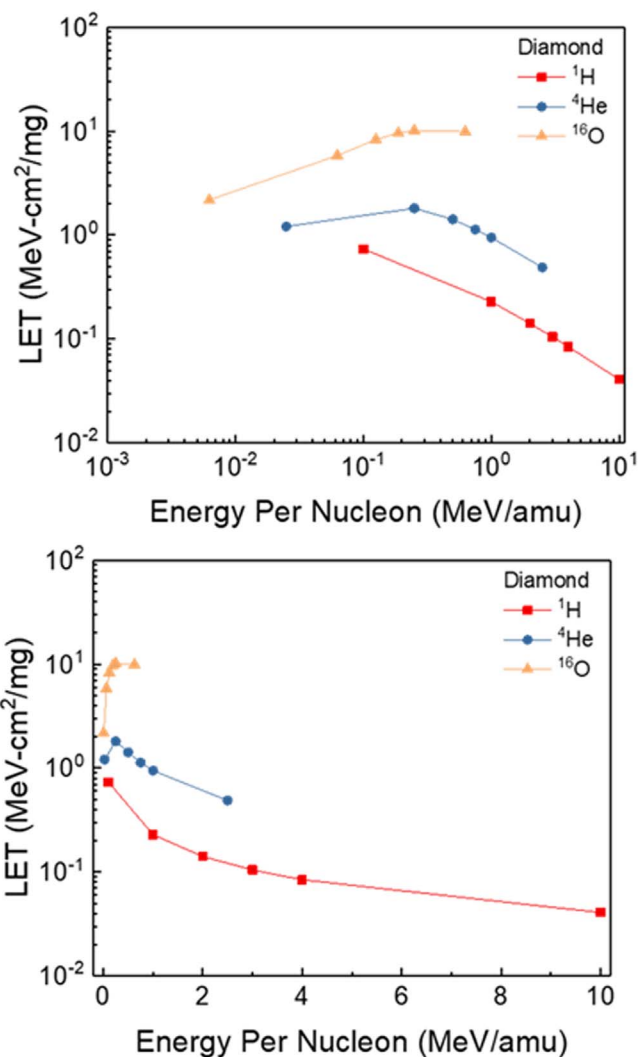


**Figure 15.** LET for diamond with ions of  $^1\text{H}$ ,  $^4\text{He}$  and  $^{16}\text{O}$ , shown on two different scales. The LET is the surface value due to ionization loss in the TRIM simulations.

Specifically, threshold voltage decreased, resulting in increased current drive. The irradiation caused increases in interface state densities, as well as input, output and reverse transfer capacitances with increasing accumulated doses.<sup>239–245</sup>

Displacement damage effects<sup>24,72,99</sup> on forward bias I-V of SiC commercial 4H-SiC Schottky diodes exposed to 203 MeV protons revealed that the diodes showed excellent resistance to radiation damage at fluences up to  $2.5 \times 10^{14} \text{ p cm}^{-2}$ . There were only minor changes in the reverse bias I-Vs with the reverse leakage decreasing with increasing irradiation fluence, while in forward bias, the sheet resistance  $R_S$  increased as fluence increases. The changes in  $R_S$  were interpreted as due to changes in the effective dopant density due to carrier removal by defects.

The effects of the collision cascade density on radiation damage in SiC remain poorly understood.<sup>93–109</sup> The damage buildup and defect interaction dynamics in 3C-SiC bombarded at 100 °C with either continuous or pulsed beams of 500 keV Ne, Ar, Kr, or Xe ions led to the conclusion that bombardment with heavier ions, which create denser collision cascades, results in a decrease in the dynamic annealing efficiency and an increase in both the amorphization cross-section constant and the time constant of dynamic annealing.<sup>42–45</sup> The cascade density behavior of these parameters is non-linear and appears to be uncorrelated. These results demonstrate an important role of the collision cascade density in dynamic radiation defect

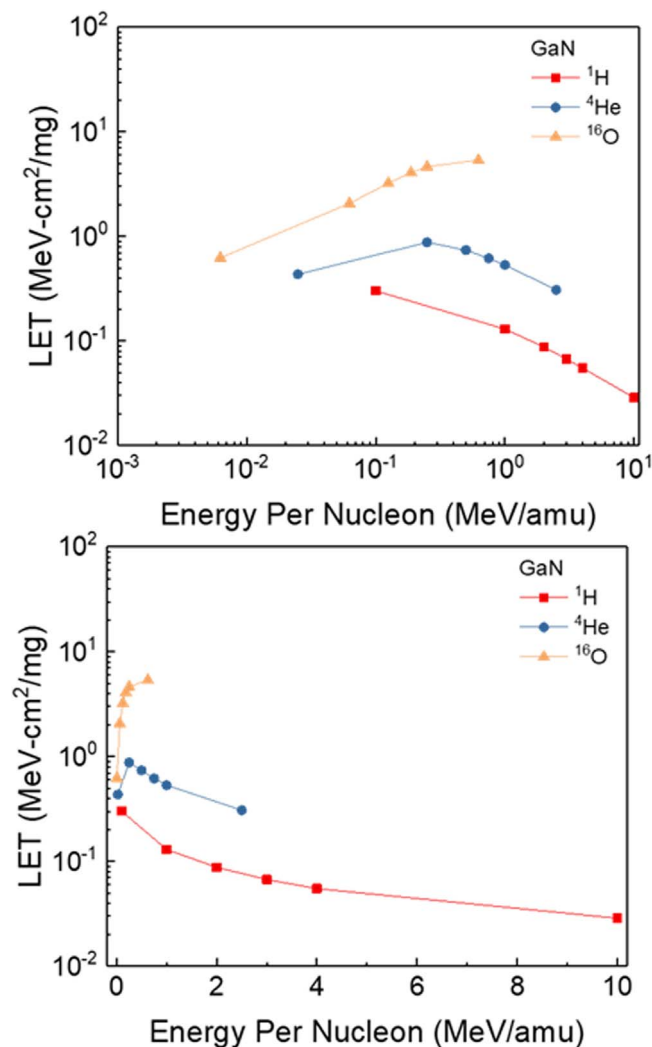


**Figure 16.** LET for GaN with ions of  $^1\text{H}$ ,  $^4\text{He}$  and  $^{16}\text{O}$  on two different scales. The LET is the surface value due to ionization loss in the TRIM simulations.

processes in 3C-SiC. Figure 18 shows the dose dependencies of relative disorder at the maximum of the bulk defect peak for 3C-SiC bombarded at 100 °C with continuous beams of 500 keV Ne, Ar, Kr, or Xe ions.<sup>38</sup>

Single event burnout (SEB) in SiC devices is destructive, but developing an understanding of the SEB cross section and FIT rate requires hardware/ test facility beam access.<sup>63,80–88</sup> The sensitive volume and secondary particle spectrum created by neutron-induced reactions must be established as part of a quantitative understanding of the effect on device performance. SiC power MOSFETs are found to be susceptible to heavy-ion irradiation and experience SEB at ground level due to terrestrial neutrons. Heavy ion data has been used to determine the threshold energy for SEB under biased operation of the devices.<sup>63,80–98</sup> This requires 3-D TCAD modelling and heavy ion simulations to estimate the sensitive volume and identify range/energy particles necessary for initiating SEB. Simulations using the radiation transport tool Monte Carlo radiative energy deposition (MRED) have been used to identify secondary particles from neutron-induced nuclear reactions in SiC which deposit energy exceeding threshold energy criterion in the sensitive volume. An analysis of the MRED simulations was then used to generate SEB cross section and calculate the sea-level failures in time (FIT) rate, which is compared to data.<sup>63,67,70–75</sup> The FIT rate is a standard industry value defined as the Failure Rate ( $\lambda$ ) per billion hours.

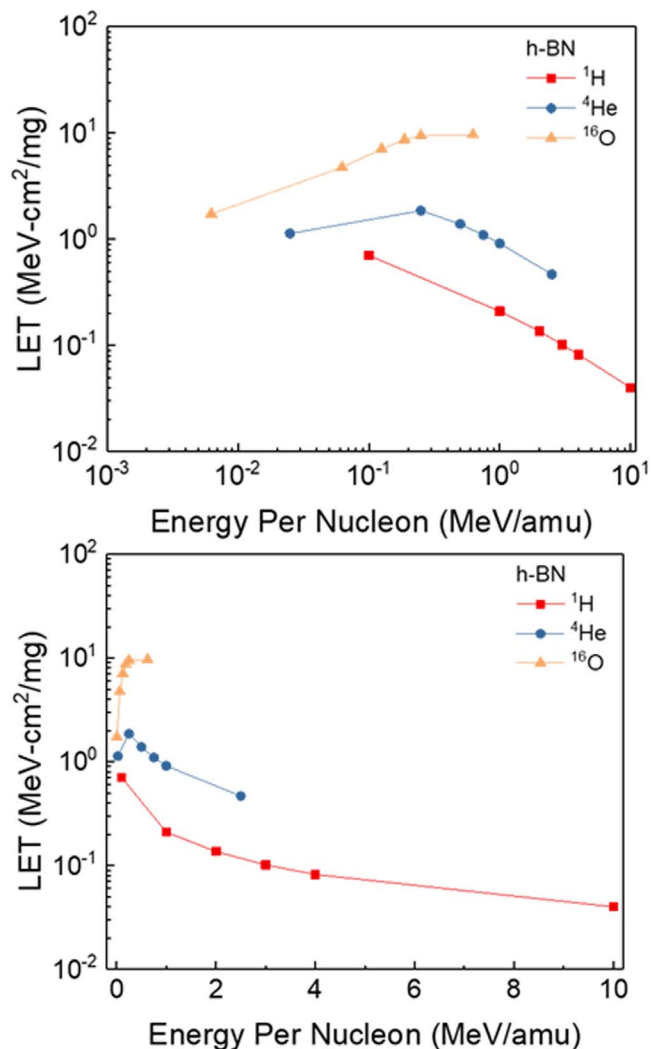


**Figure 17.** LET for h-BN with ions of  $^1\text{H}$ ,  $^4\text{He}$  and  $^{16}\text{O}$  on two different scales. The LET is the surface value due to ionization loss in the TRIM simulations.

SiC power metal-oxide-semiconductor field effect transistors (MOSFETs) are space-ready in terms of typical reliability measures. However, single event burnout (SEB) due to heavy-ion irradiation often occurs at voltages 50% or lower than specified breakdown. Failure rates in space are estimated for burnout of 1200 V devices based on the experimental data for burnout and the expected heavy-ion linear energy transfer (LET) spectrum in space.<sup>72,78,93,94</sup> Figure 19 shows cumulative failure rate for SiC power MOSFETs as a function of 70 MeV proton dose.

For lower LET ions, including protons, SEBs were observed and there was no leakage current increase just before these occurred.<sup>97–101</sup> The phenomenon is unique for SiC devices. The collected charge spectra obtained with heavy ion irradiation were similar to those for Si power MOSFETs. The data suggests that radiation effect immunity might be enhanced by the same techniques used for Si power MOSFETs. However, in addition to the charge multiplication effect, the increased leakage current was observed before catastrophic failures were triggered under some high LET conditions. The leakage current increase was observed at much less than the rated voltage during heavy ion irradiation and the behavior was similar to SiC SBDs.<sup>97–101</sup>

Figure 20 compares the effect of neutron irradiation on the forward I-V characteristics of 4.5-kV Si and 4H-SiC diodes.<sup>70</sup> Both devices show gradual degradation of the ON-state characteristics, however, the increase of forward turn-on voltage of the 4H-SiC

**Table IV.** Typical energy losses for different energy protons in GaN.

Energy Loss	1.8 MeV	15 MeV	40 MeV	100 MeV
Ionizing energy loss (keV/ion)	114	26	12	6.5
NIEL (eV/ion)	3	0.3	0.1	0.05
Max fluence (cm <sup>-2</sup> )	10 <sup>12</sup>	5 × 10 <sup>10</sup>	10 <sup>11</sup>	10 <sup>13</sup>
Total ionizing dose (rads)	10 <sup>6</sup>	2 × 10 <sup>4</sup>	1.5 × 10 <sup>4</sup>	8 × 10 <sup>5</sup>

diode is significantly smaller but at higher current densities.<sup>70,72–75</sup> The effect of displacement damage from neutron irradiation on static characteristics of Si and 4H-SiC p-i-n diodes produces various deep levels which reduce carrier lifetime, compensate for the n-base doping and increase leakage current.<sup>70,72–75</sup> Although the number of introduced defects in 4H-SiC is higher and the lifetime degradation and carrier compensation proceed faster than in Si, the lower thickness and higher doping level of the SiC n-base compensate for these negative effects. The SiC diode then exhibits substantially higher resistance to neutron irradiation at higher fluences when the Si diode loses its ON-state carrier modulation capability.<sup>70,72</sup>

The effect of very high energy protons (>50 MeV) has also been explored, and the responsible spallation fragments produced that could trigger single event burnout have been identified by simulations.<sup>44</sup> The most probable ion species responsible to cause SEBs were identified as Na and Al, based on the Geant4 simulations.<sup>44</sup> SiC Junction Barrier Schottky Diodes exposed to 50 MeV and 90 MeV protons up to a fluence of 5 × 10<sup>10</sup> cm<sup>-2</sup> exhibited a decrease in the reverse leakage current with fluence and no SEB occurring. The change in leakage current was found to be due to an increase of barrier height and the reduction of carrier concentration.<sup>211</sup>

**GaN.**—GaN-based devices are tolerant to ionizing radiation because conventional GaN HEMTs do not have gate oxides, and instead they use Schottky gate contacts. However, defects at the AlGaN-GaN interface, as well as introduction of gate oxide layers (both MOS-HEMTs and MIS-HEMTs) can increase susceptibility to TID. The radiation response of GaN devices partially depends on the distance between the 2D-channel and Si, on which some of these devices are grown. This may explain some of the normalized breakdown voltage dependency trend of GaN HEMTs. Additionally, GaN HEMTs are significantly overdesigned compared to SiC devices, due to their lack of avalanche capability. This may make them “appear” more single event tolerant.

Proton damage on the steady-state and dynamic response of PECVD passivated GaN HEMTs before and after 2 MeV proton irradiation was explained by degradation of 2DEG mobility and sheet carrier density.<sup>134–136</sup> At 6 × 10<sup>14</sup> H<sup>+</sup>/cm<sup>2</sup>, 2DEG mobility degrades by >30%, 2DEG sheet carrier density by ~10%. Results in decrease in Fermi level of the GaN, also decreases number of mobile electrons in 2DEG.

The dependence of proton energy on degradation of AlGaN/GaN MOSHEMTs, showed significant suppression of MOSFET current after dose of 10<sup>15</sup> cm<sup>-2</sup> 10 MeV protons-equivalent to hundreds of years in low earth orbit, and recovery stages after 450 °C–500 °C anneal. Similar results were obtained for alpha particles, while electrons were less damaging.<sup>129–136</sup>

The high gate leakage and drain current collapse in conventional Schottky gate metal devices limits the stability and performance of HEMTs. To solve these problems, MOSHEMTs can be employed to reduce the gate leakage current and passivate surface traps, with Sc<sub>2</sub>O<sub>3</sub>, MgO, SiO<sub>2</sub> and Si<sub>3</sub>N<sub>4</sub>, as the most effective gate dielectrics. Al<sub>2</sub>O<sub>3</sub> deposited by atomic layer deposition (ALD) has also been used as the gate oxide due to its advantages in excellent conformability, low defect density, low stress, and excellent adhesion. Moreover, Al<sub>2</sub>O<sub>3</sub> has a high dielectric constant (k ~ 10), high breakdown field (5–10 MV cm<sup>-1</sup>), excellent thermal stability, and chemical stability against reaction with AlGaN. Figure 21a shows

the reduction in drain-source current after 10 MeV proton irradiation, while 21(b) shows the relationship between carrier removal rate and proton energy in these MOSHEMTs. As noted previously, the damage in the active layers is reduced for higher proton energies because they are close to the surface and the energy loss by the protons is reduced.<sup>129–136,153</sup>

For 10 MeV electron irradiation of n-GaN MOCVD and epitaxial lateral overgrowth (ELOG) layers, the irradiation produced compensation of n-type conductivity and the carrier removal rate increased substantially with starting donor concentration. The main compensating defect was an 0.15 eV electron trap. Once the Fermi level crossed this level, two centers at 0.2 eV and 1 eV contribute to compensation. After high doses, Fermi level in moderately doped GaN pinned near Ec-1 eV. The carrier removal rate in ELOG n-GaN was lower than MOCVD samples with similar doping level.<sup>167–171</sup>

For gamma rays, annealing at 200 °C results in a partial recovery of diffusion length, drain current and transconductance and this is dependent on the dose. Devices that show the most recovery are those exposed to the lowest dose of gamma rays. Those exposed to high doses show no recovery. The experimental dependence of minority carrier diffusion length (L) with temperature can be explained by  $L = L_0 \exp(-\Delta E_a / 2kT)$  where L is the diffusion length, L<sub>0</sub> is a scaling factor, k is Boltzmann constant, and ΔE<sub>a</sub> is the thermal activation energy related to carrier recombination.<sup>117–139</sup>

In addition to a reduction in carrier concentration in the channel of the MOSHEMTs, the electron mobility is also reduced electron mobility due to introduction of charged trap states. mobility reduction. This is shown in Fig. 22, along with the sheet carrier reduction.

Figure 23 shows a comparison of the carrier removal rates for different types of radiation in GaN, as a function of energy. Protons are the most damaging, followed by neutrons, electrons and gamma rays. In the latter case, it has been suggested that interactions between radiation-induced point defects and threading dislocations (TDs) affect the evolution of radiation damage.<sup>154,182</sup>

The carrier removal rate in GaN for light particles is well accounted for by the introduction of simple defects.<sup>109,131,132</sup> The carrier removal rate in nitrides depends on radiation type, growth method and the dislocation density and distribution. For fast neutrons which create large recoil cascades, carrier removal is by disordered regions in which the Fermi level in the core is pinned between the Ga<sub>i</sub> donor level and the N<sub>i</sub> acceptor level. There were no significant dose rate effects on the carrier loss rate in AlGaN/GaN HEMTs during either 10 MeV electron or 10 MeV proton irradiation to total doses of 10<sup>13</sup> cm<sup>-2</sup> (protons) or 10<sup>15</sup> cm<sup>-2</sup> (electrons) over a range of almost two orders of magnitude in dose rate for both types of radiation.<sup>109,131,132</sup> These are all metal gate devices and comparable experiments for MOS-gated HEMTs have yet to be done to see if there is either enhanced low dose rate sensitivity (ELDRS) or time-dependent effects due to oxide trapped charge, interface states or hydrogen.

For high-Al content (Al > 50%) AlGaN/GaN HEMTs, there has been heavy ion and proton data showing SEB, TID, and displacement damage response.<sup>234</sup> There was little effect of 2.5 MeV protons in either these HEMTs or those with conventional Al contents (22%–25%). The burnout voltages decreased with increasing LET, falling to 25% of nominal breakdown voltage for ions with LET of 34 MeV·cm<sup>2</sup> mg<sup>-1</sup> (range > 20 μm). Burnout events begin with heavy ion strike between gate and drain. Initiates cascade resulting

**Table V. Summary of radiation effects in semiconductors.**

Type of Radiation Effect	Type of Exposure	Energy Transfer	Type of Radiation
Single Event Effects, SEE	Single interaction-temporary or permanent damage to electronic devices	Sudden large $\Delta E$ ionization deposited in the active volume or sudden high $\Delta E$ transfer to a single nucleus	heavy charged ion and protons
Total Ionization Dose, TID	Long term exposure to ionizing radiation-  Causes charge build-up in insulators leading to device failure	Small $\Delta E$ ionization deposited uniformly and delivered  over a long period. Gammas, X-rays, protons, and electrons are the main sources of ionizing dose effects	Charged particles such as protons, and electrons, also neutrons. Neutron radiation is not an ionizing radiation, but the neutron-knock on atoms are usually ionizing.
Displacement Damage, NIEL	Long term exposure to non-ionizing radiation-causes displacement defects in semiconductors (introduction of deep band-gap traps)	Accumulation of small $\Delta E$ transfers to atomic nuclei (Coulomb, nuclear interactions).	protons, neutrons, high energy electrons



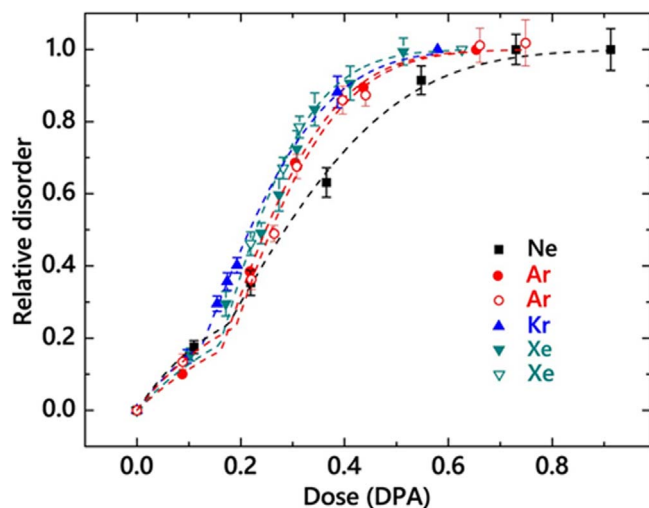


**Figure 18.** Dose dependencies of relative disorder at the maximum of the bulk defect peak for 3C-SiC bombarded at 100 °C with continuous beams of 500 keV Ne, Ar, Kr, or Xe ions (closed symbols) with a of  $1.9 \times 10^{13} \text{ cm}^{-2} \text{ s}^{-1}$  and (open symbols) with lower  $F$ s of  $4 \times 10^{12} \text{ cm}^{-2} \text{ s}^{-1}$  for Xe ions and  $8.4 \times 10^{12} \text{ cm}^{-2} \text{ s}^{-1}$  for Ar ions. Dashed lines are results of fitting with a stimulated amorphization model (reprinted from Bayu Aji,<sup>64</sup> Scientific Reports, open access).

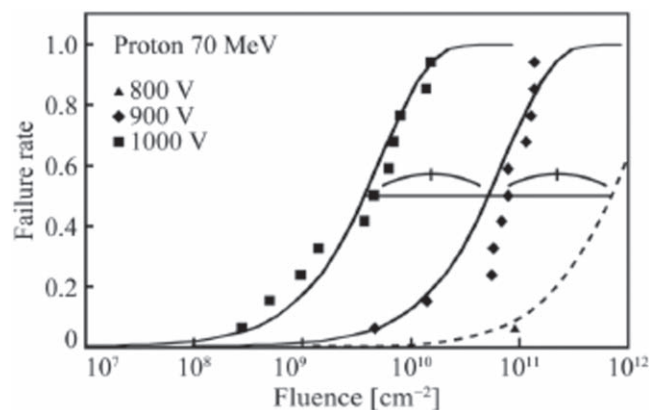


**Figure 19.** Cumulative failure rate of SiC power MOSFETs as a function of proton fluence at different energies (reprinted with permission from Ref. 65, Mizuta, IEEE Trans NS 61,1924 (2014), copyright IEEE).

in damage manifested elsewhere in device. Research prototypes of AlGaIn HEMTs have exhibited reduced SEB threshold in simulated space environments.<sup>234</sup>

Heavy ion irradiation of AlGaIn/GaN high electron mobility transistor (HEMTs) devices with swift heavy ions (SHIs) at different fluences produced a significant deterioration of structural and electrical properties of the devices.<sup>199</sup> With typical energies in the MeV and above range per nucleon, SHIs lose their energy in the target primarily via electronic interactions. In semiconductors, this often induces ionization spikes along their paths that promote the formation of latent tracks and surface effects. Moreover, it has been reported that SHI radiation can lead to the recovery of pre-damaged material, including the recrystallisation of amorphous materials.

Positive threshold voltage  $V_{th}$  was found to increase by about 85% as a result of irradiation with 1540 MeV  $^{209}\text{Bi}$  ions at fluence of  $1.7 \times 10^{11} \text{ ions cm}^{-2}$ , while this threshold voltage value was increased by 55% after irradiation with 2300 MeV  $^{129}\text{Xe}$  at a fluence of  $4 \times 10^{11} \text{ ions cm}^{-2}$ . The maximum saturation drain current  $I_{ds}$  was decreased by about two orders of magnitude in the device after irradiation with  $^{209}\text{Bi}$  ions.<sup>199</sup> Quasi-continuous tracks

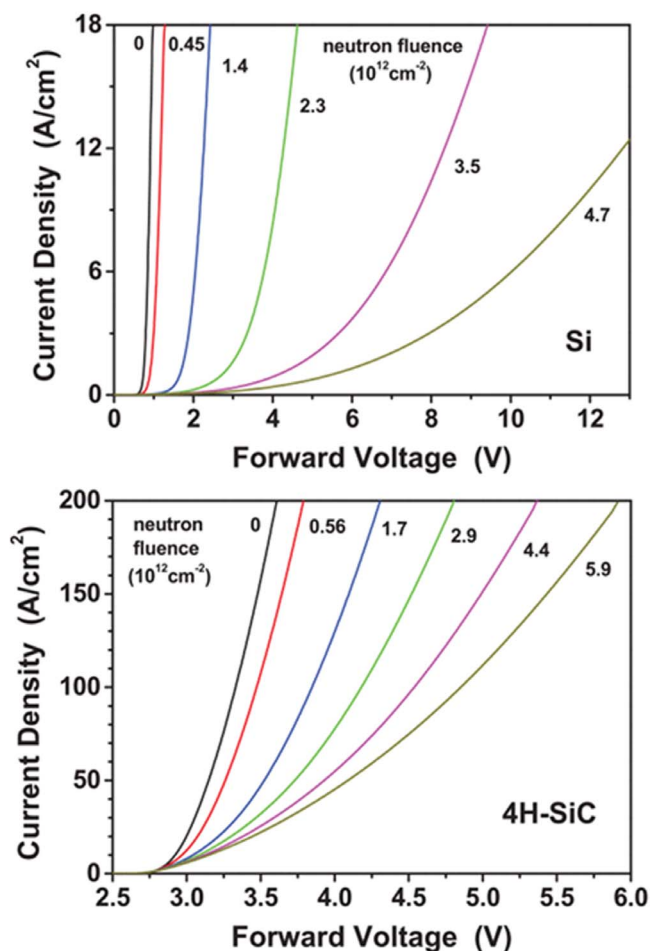


**Figure 20.** Effect of neutron irradiation on forward I–V curves of 4.5-kV silicon (top) and 4H-SiC (bottom) diodes measured at room temperature. (after Hazdra,<sup>70</sup> copyright IEEE).

were observed visually in the devices after irradiation with  $^{209}\text{Bi}$  ions. The observed defects and disorders induced in the devices by SHI irradiation were found responsible for the decrease in carrier mobility and sheet carrier density, and finally, these defects resulted in the degradation of electrical characteristics of HEMTs.

The effect of low- to medium-energy ions in GaN is relatively well understood,<sup>109,131,132</sup> while the damage created in the high-energy radiation regime is less clear. In space, the latter is of special interest when studying the influence of the so-called HZE (high atomic number  $Z$  and high energy) ions, a crucial component of the galactic cosmic radiation (GCR) and solar radiation spectra. Although less abundant than proton and gamma radiation, HZE ions (such as Fe and Si) have a very high ionization power and relatively high fluxes. This likely not only accelerates the degradation but also can cause single-event catastrophic failure of devices.

**In-Situ TEM of GaN HEMTs During Irradiation.**—Energetic particle irradiation of HEMTs has also been examined with in situ TEM.<sup>197–199</sup> HEMTs were irradiated ex situ normal to the surface with 1.5 MeV Au<sup>+</sup> ions using the 6 MV HVE Tandem accelerator at Sandia National Laboratories. Cross-sectional images are shown in Fig. 24. Irradiation can induce defects in the device layer as shown in Fig. 24a by yellow-colored arrowhead and dotted box. At 10 V drain bias, this area further degrades as shown in Fig. 24b. A change in contrast near the gate is also observed due to the high gate leakage as marked by the yellow color dotted rectangular region. At 10.2 V bias, the irradiated device fails due to the high gate leakage current,

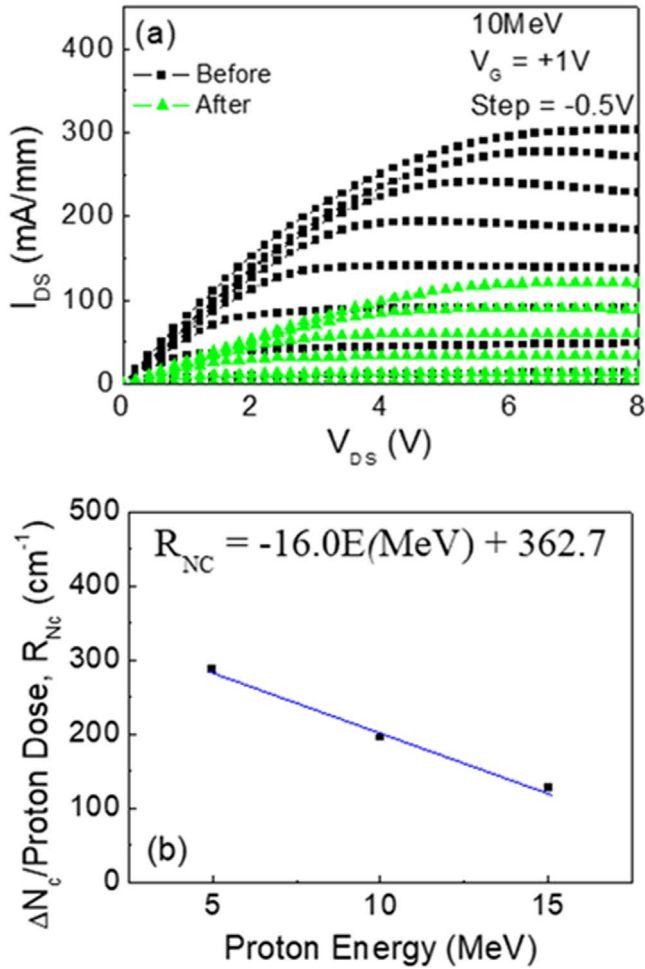


**Figure 21.** (a) Reduction in drain-source current of AlGaIn/GaN MOSHEMTs after irradiation with 10 MeV protons and (b) carrier removal rate in the channel of the HEMTs as a function of proton energy. (adapted from L. Liu, J. Vac. Sci. Technol. B 31, 042202 (2013),<sup>130</sup> copyright American Vacuum Society.

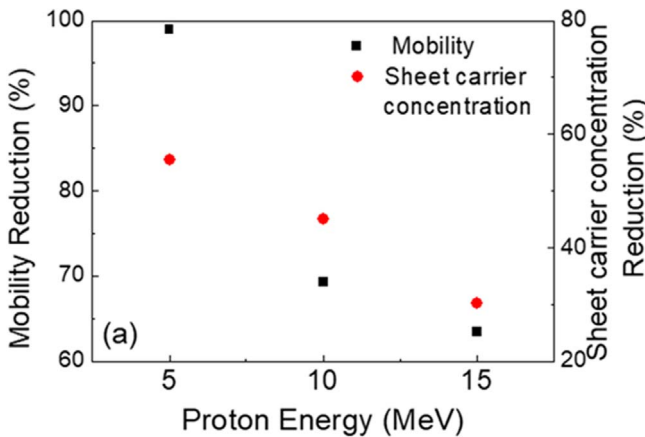


**Figure 22.** Reduction in electron mobility and sheet carrier density in proton irradiated AlGaIn/GaN MOSHEMTs as a function of proton energy for fixed fluence.

which further creates permanent damage in the buffer layer near the gate area.<sup>197–199</sup> A breaching between the passivation layer and the buffer layer is also observed. This could be attributed to the defects formation and surface roughness increment due to the ion irradiation at the interface.

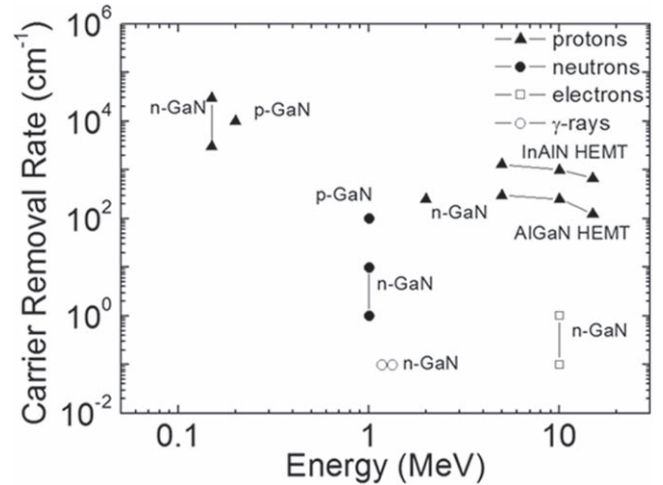


**Figure 23.** Summary of carrier removal rates for different types of radiation in GaN.

**Pulsed-laser approaches to SEE in GaN.**—SEE by heavy ions generated by the impact of galactic cosmic rays, solar particles or energetic n and p are typically simulated terrestrially using a cyclotron. Two common ions used to evaluate radiation tolerance are Xe (LET  $\sim 50$ ) and Au ( $\sim 85$  MeV $\cdot$ cm<sup>2</sup> mg<sup>-1</sup>). The use of lasers to simulate SEE enables the generation carriers in well-defined locations in complex circuits.<sup>80–88</sup> This has proven indispensable for single-event effects (SEE) and radiation hardness and while not a complete replacement for heavy-ion experiments, it is both versatile and convenient.

Both single-photon absorption (SPA) and two-photon absorption (TPA) pulsed-laser systems allow for rapid-feedback of radiation studies at fraction of cost of conventional heavy-ion broad beam testing. SPA pulsed-lasers inject charge carriers directly into the surface of the structure, whereas TPA pulsed-lasers use sub-bandgap photons to create electron-hole pairs (EHP) deep within device. SPA employs lasers with photon energies  $>E_G$ . Ability to tune photon energy, allows tailoring of generated carrier distribution (CD) to the specific semiconductor material. The spatial extent of the CD is dictated in the radial direction by focused laser spot size.<sup>80–88</sup>

As an example from the literature, single-event transients were generated with focused, pulsed X-rays in a MIS-gate AlGaIn/GaN HEMT. Measured transients reveal current flow between source/drain, in contrast to Schottky-gate HEMTs. Single event effects in AlGaIn/GaN HEMTs<sup>80–88</sup> employed a 293 nm (4.23 eV) laser to inject charge into HEMTs. At this wavelength, e-h pairs injected into GaN as well as AlGaIn barrier. Spot size of the laser  $\sim 0.5$   $\mu$ m and the pulse width is 1 ps. The spot size is dependent on wavelength—at 293 nm the FWHM spot size is  $\sim 0.3$   $\mu$ m, while at 590 nm, it is  $\sim 0.7$   $\mu$ m. Irradiated HEMTs had SETs with long tail with lifetime of 20–30 ns. For pristine SET lifetime was shorter,  $\sim 7$ –9 ns. Transients of a non-irradiated HEMT for the SPA experiment at a discrete location between the gate and drain were recorded and exponential fits for the transient were consistent with defect states with lifetimes 20–30 ns. The laser can be scanned across the device, creating map of peak amplitudes or maps of collected charge. On unirradiated HEMTs, maximum collected charge appears in a line located nearby not directly adjacent to the gate metal. At certain locations, there appears to be a spot where there is a higher signal. After irradiation, single event transients of irradiated HEMTs have longer slow decaying tails, which lead to enhancement of the collected charge.

Figure 25 shows a schematic of a typical laser injection system for SEE experiments. Application of a sub-micron spot size ultraviolet (UV) pulsed laser light for single event transients (SETs) investigation.<sup>80–88</sup>

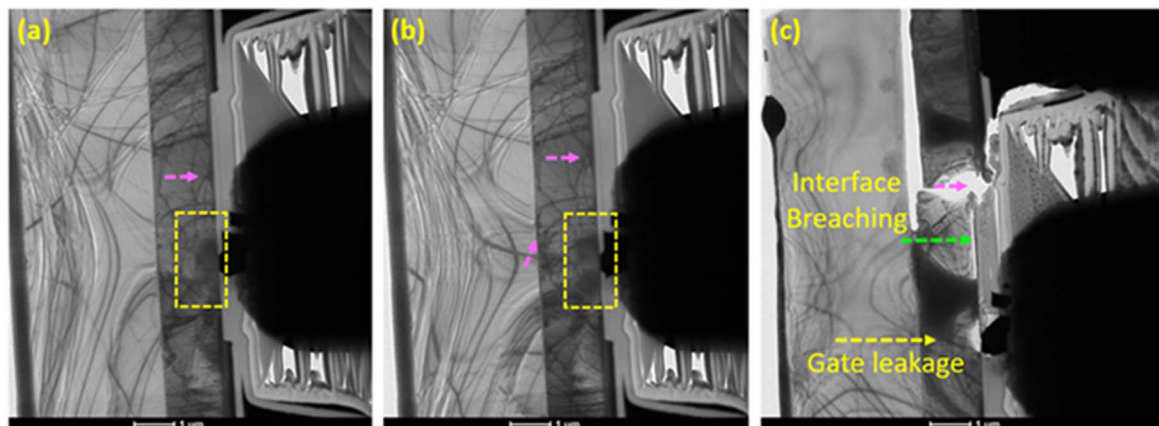


**Figure 24.** In-situ TEM images of GaN HEMT under off-state biasing conditions. The HEMT was irradiated at 45 dpa: (a) Before biasing, (b) Biasing at drain voltage 10 V, and (c) Failure at 10.2 V,<sup>197</sup> adapted from Z.Islam,<sup>197</sup> copyright IOP.

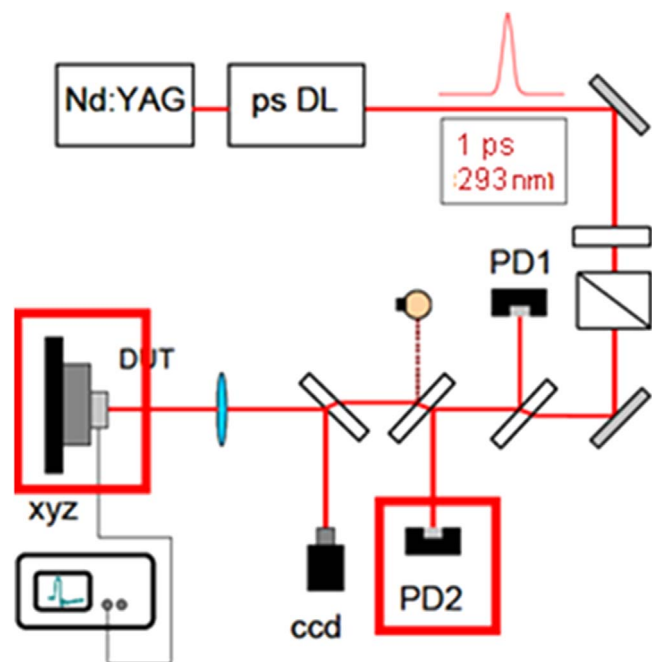


**Figure 25.** Schematic diagram of pulsed laser setup used for non-destructive single event characterization of the GaN HEMTs.

Application of a sub-micron spot size ultraviolet (UV) pulsed laser light for single event transients (SETs) investigation allows high precision spatial mapping of defects and traps in AlGaIn/GaN device (probing of dislocations). The shapes of the SETs tell us about the quality of the material—“hot spots” that are attributed to the presence of lattice defects that modify the electric field in the drain at the edge of the gate and reveals information about trap density and lifetime. Typical devices show slow decaying tails-for proton irradiated device the tails is 30 ns, for pristine one  $\sim 8$  ns with the preliminary conclusion being that these are traps due to nitrogen vacancies. Examples are shown in Fig. 26, showing the excellent spatial resolution that is possible.<sup>87</sup> We used 100 nm/step for these XY scans to save time, but our stage can have as low as 10 nm/step.

**Ga<sub>2</sub>O<sub>3</sub>.—Neutron and gamma-ray damage in Ga<sub>2</sub>O<sub>3</sub>.—**Arehart et al.<sup>215</sup> irradiated n-Ga<sub>2</sub>O<sub>3</sub> with 2 MeV neutrons to a fluence of  $4 \times 10^{15} \text{ cm}^{-2}$ . This produced a decrease in reverse current in rectifier structures and a loss of carriers at a rate of  $\sim 20 \text{ cm}^{-1}$ . The most significant change in the properties of the material was the introduction of a deep trap state at  $E_C-1.88 \text{ eV}$  observed in deep

level transient spectroscopy measurements, ascribed to an oxygen-vacancy related state. Inelastic neutron scattering becomes important for neutron energies above 1 MeV, i.e. scattering of a neutron such that the kinetic energy is not preserved, but goes into an excitation of the (potential) energy of the nucleus.

Ga<sub>2</sub>O<sub>3</sub> has also been investigated as a radiation detection material for fast (14 MeV) neutrons, utilizing the  $^{16}\text{O}(\text{n},\alpha)^{13}\text{C}$  reaction. Two other semiconductors, diamond and 4H-SiC, have previously been investigated as nuclear detectors under extreme conditions, involving temperatures up to 700 °C for 4H-SiC and 200 °C for diamond. The fast neutrons could be detected under these conditions, but the resolution was insufficient for spectroscopy.

Wong et al.<sup>241</sup> examined the gamma-ray irradiation tolerance of Ga<sub>2</sub>O<sub>3</sub> MOSFETs to doses of 230 kGy (SiO<sub>2</sub>). Hysteresis in the transfer characteristics was negligible after exposure to the highest dose, while degradation in the gate oxide were found to limit the overall radiation resistance.<sup>241–244</sup>

**Proton damage in Ga<sub>2</sub>O<sub>3</sub> rectifiers.**—Yang et al.<sup>207</sup> subjected vertical rectifiers fabricated on epi Ga<sub>2</sub>O<sub>3</sub> on bulk  $\beta$ -Ga<sub>2</sub>O<sub>3</sub> to 1.5 MeV electron irradiation at fluences from  $1.8\text{--}14.3 \times 10^{15} \text{ cm}^{-2}$ . The electron irradiation caused a reduction in carrier concentration with a carrier removal rate of  $4.9 \text{ cm}^{-1}$ . This compares to a carrier removal rate of  $\sim 300 \text{ cm}^{-1}$  for 10 MeV protons in the same material. The 2kT region of the forward current-voltage characteristics increased due to electron-induced damage, with a more than 2 order of magnitude increase in on-state resistance at the highest fluence. There was a reduction in reverse current, which scaled with electron fluence. The on/off ratio at  $-10 \text{ V}$  reverse bias voltage was severely degraded by electron irradiation, decreasing from approximately  $10^7$  in the un-irradiated reference diodes to approximately  $2 \times 10^4$  for the highest fluence of  $1.43 \times 10^{16} \text{ cm}^{-2}$ . The reverse recovery characteristics showed little change even at this highest fluence, with values in the range 21–25 nsec for all rectifiers. The changes in device characteristics were accompanied by a decrease in electron diffusion length from 325 to 240  $\mu\text{m}$  at 300 K.

**Proton damage in Ga<sub>2</sub>O<sub>3</sub> nanobelt transistors.**—Proton damage in back-gated field-effect transistors (FETs) fabricated on exfoliated quasi-two-dimensional  $\beta$ -Ga<sub>2</sub>O<sub>3</sub> nanobelts was studied for devices exposed to fluences of 10 MeV protons.<sup>218</sup> Figure 27 (top) shows an SEM image of the nanobelt transistor structure, in which the exfoliated nanobelt is positioned between Ti/Au source and drain contacts and SiO<sub>2</sub>/Si metallized with Ti/Au is used as the backgate. These devices were then exposed to 10 MeV proton beams, as shown at the bottom of Fig. 27. The radiation damaged FETs showed a decrease of 73% in the field-effect mobility and a positive shift of threshold voltage after proton irradiation at a fluence of  $2 \times 10^{15} \text{ cm}^{-2}$ , which corresponds to approximately  $10^5$  times the



## AlGaIn/GaN Schottky-Gate HEMT on Si

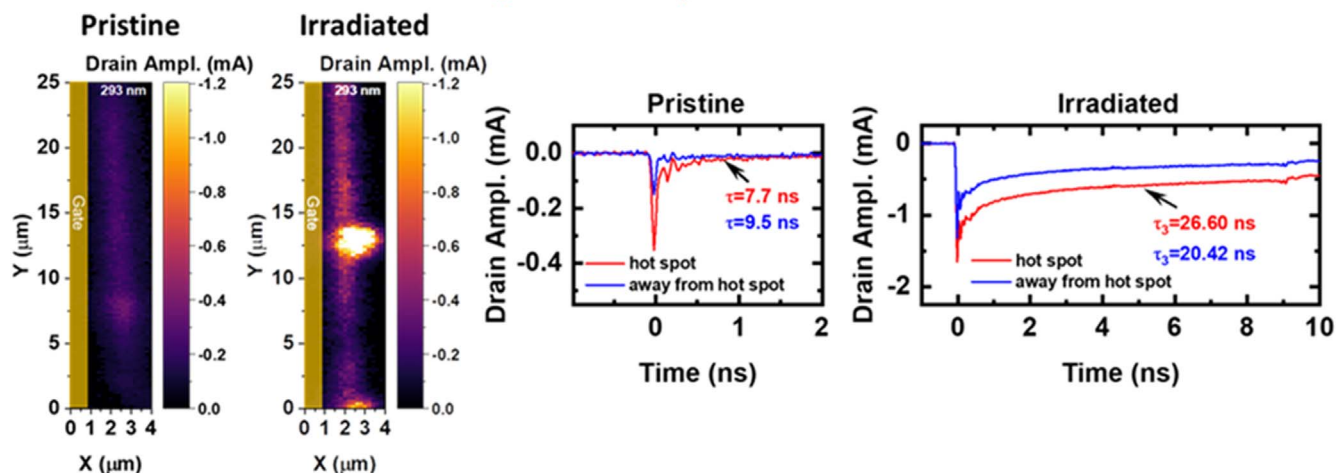


Figure 26. Typical current transients during laser injection of carriers into an AlGaIn/GaN HEMT, from Khachatryan,<sup>87</sup> copyright IEEE.

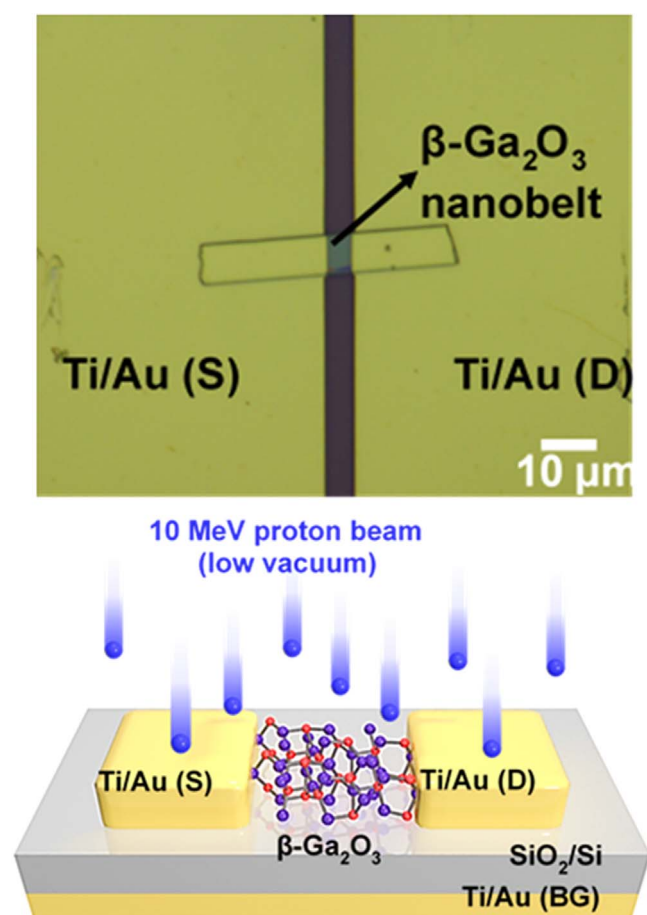


Figure 27. Optical image of single Ga<sub>2</sub>O<sub>3</sub> nanobelt transistor (top) and the experimental configuration for studying effect of proton damage on the characteristics of these devices (bottom). Reprinted with permission from G. Yang, ACS Applied Materials and Interfaces (2017),<sup>112</sup> copyright American Chemical Society.

intensity of a solar proton event. The on/off ratio of the exfoliated  $\beta$ -Ga<sub>2</sub>O<sub>3</sub> FETs was maintained even after proton doses of up to  $2 \times 10^{15} \text{ cm}^{-2}$ . The data are summarized in the drain-source characteristics of Fig. 28, which show the effect of proton dose.<sup>218</sup> Note that doses of  $1\text{--}2 \times 10^{15} \text{ cm}^{-2}$  both lead to significant suppression of the

drain current. The radiation-induced damage in  $\beta$ -Ga<sub>2</sub>O<sub>3</sub>-based FETs was significantly recovered after rapid thermal annealing at 500 °C. This annealing temperature is also similar to those needed for removal of plasma-induced dry etch damage in Ga<sub>2</sub>O<sub>3</sub>.<sup>219</sup>

**Proton damage in Ga<sub>2</sub>O<sub>3</sub> photodetectors.**—The cut-off wavelength of  $\beta$ -Ga<sub>2</sub>O<sub>3</sub> is  $\sim 250 \text{ nm}$ , which means it is intrinsically solar-blind and DUV photodetectors made from this material do not require any supplementary filters. Planar thin film  $\beta$ -Ga<sub>2</sub>O<sub>3</sub> photodetectors were irradiated with 5 MeV protons at doses from  $10^{13}\text{--}10^{15} \text{ cm}^{-2}$  and the resulting effects on photocurrent, responsivity, quantum efficiency and photo-to-dark current ratio (PDCR) at 254 nm wavelength were measured at both 25 and 150 °C. The devices were subjected to doses of 5 MeV protons between  $10^{13}\text{--}10^{15} \text{ cm}^{-2}$  at 25 °C. These doses are equivalent to many decades of exposure in low earth orbit. Protons of this energy completely traverse the Ga<sub>2</sub>O<sub>3</sub> film and pass into the sapphire substrate. The energy loss and damage profile were calculated from the SRIM code. This Monte Carlo code (Transport of Ions in Matter)/SRIM (Stopping and Range of Ions in Matter) is widely used to obtain information about vacancy production rates. SRIM can also be employed to calculate NIEL. The SRIM output gives the vacancy production rate as a function of position as the incident proton slows down in the target material. Combining these data with the total energy loss data, the vacancy production rate as a function of proton energy can be found.

The dark current increased in proportion with the implant dose, leading to a decrease in the ratio of photocurrent to dark current.<sup>244</sup> The increase in photocurrent relative to the dark current measured under exposure to this light can be explained by the presence of defect levels within the bandgap. The photo-to-dark current ratio decreased from  $\sim 60$  in the control samples to  $\sim 9$  after proton doses of  $10^{15} \text{ cm}^{-2}$  for illumination with 254 nm photons and correspondingly lower numbers for 365 nm illumination. Ga<sub>2</sub>O<sub>3</sub> photodetectors were subject to fluences of 5 MeV protons from  $10^{13}\text{--}10^{15} \text{ cm}^{-2}$ . The non-ionizing energy loss of the protons as they traverse the Ga<sub>2</sub>O<sub>3</sub> layers creates states in the gap that increase the photocurrent but decrease the photo-to-dark current ratio as the proton fluence increases.

**Defects created by proton implantation into Ga<sub>2</sub>O<sub>3</sub>.**—To understand the defects created in Ga<sub>2</sub>O<sub>3</sub>, H or D was introduced by ion implantation at room temperature with multiple doses and energies (up to 180 keV) to obtain H or D concentrations of approximately  $1 \times 10^{20} \text{ cm}^{-3}$  in a layer 1200 nm in depth.<sup>233</sup> All of the crystals used had  $(\bar{2}01)$  surface orientation, with  $[0\ 1\ 0]$  and  $[1\ 0\ 2]$  edges.



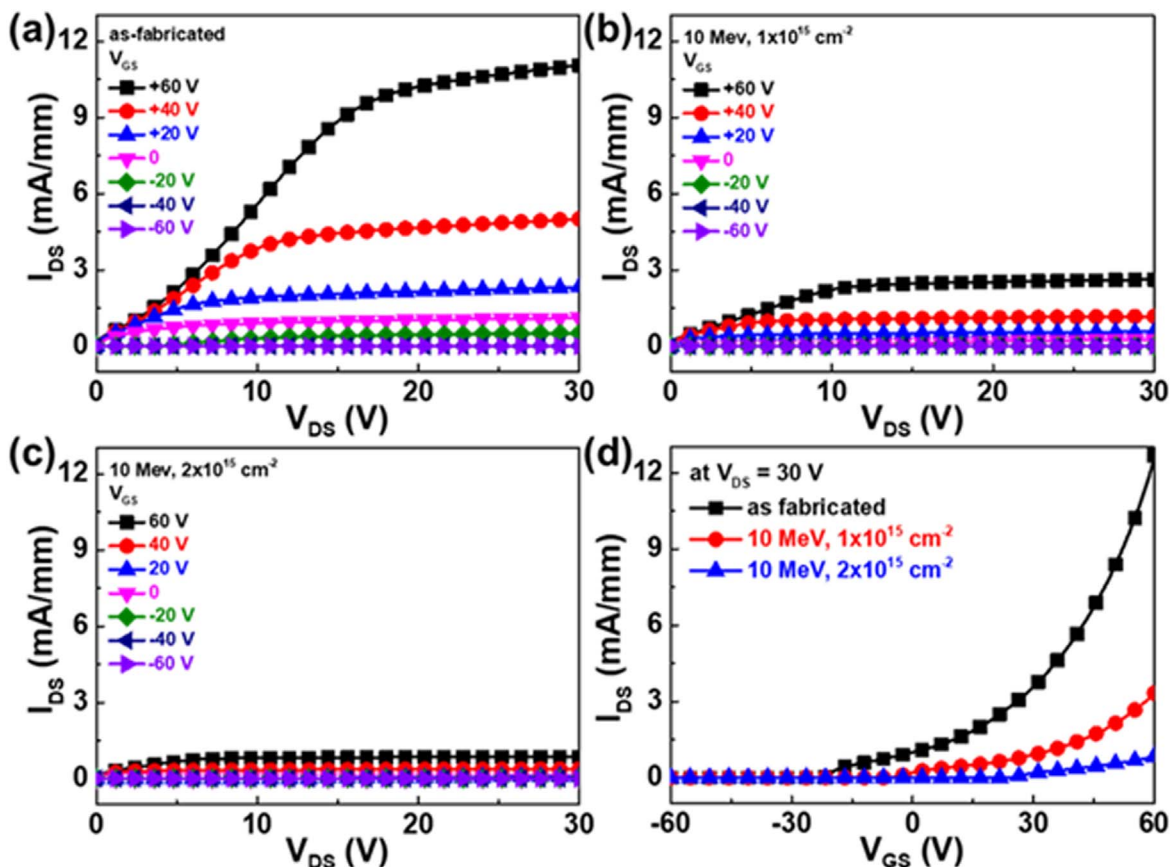


**Figure 28.** Output characteristics ( $I_{DS}$  vs  $V_{DS}$ ) of  $\beta$ -Ga<sub>2</sub>O<sub>3</sub> nanobelt FET before and after 10-MeV proton irradiation at different doses: (a) as-fabricated, (b)  $1 \times 10^{15} \text{ cm}^{-2}$ , and (c)  $2 \times 10^{15} \text{ cm}^{-2}$ , (d) transfer characteristics ( $I_{DS}$  vs  $V_{GS}$ ) of  $\beta$ -Ga<sub>2</sub>O<sub>3</sub> nanobelt FET at  $V_{DS} = 30 \text{ V}$  before and after 10-MeV proton irradiation at different doses. Reprinted with permission from G. Yang, ACS Applied Materials and Interfaces (2017),<sup>112</sup> Copyright 2017, American Chemical Society.

Fourier Transform Infrared Spectroscopy (FTIR) experiments were carried out to examine temperature- and polarization-dependent effects as well as relative H- and D-concentrations.<sup>233</sup> The results of experiment, coupled with detailed theoretical calculations, show no evidence of interstitial atomic hydrogen (H<sub>i</sub>); instead, the defects observed appear to be in a family that involves H trapped at a Ga vacancy, the primary member involving a particular two-H configuration.<sup>233</sup> For samples in which hydrogen or deuterium was inserted by annealing in those ambients of H<sub>2</sub> or D<sub>2</sub> gas, we observe strong absorption lines at 3437 and 2545 cm<sup>-1</sup>. If the samples were annealed in H<sub>2</sub> and D<sub>2</sub> simultaneously, these OH and OD lines become split into two lines.<sup>233</sup> This requires these are defects that contains two equivalent H atoms, not one. This, and the fact that the lines are completely polarized, leads to the model where two H atoms are bonded to a Ga vacancy. When the samples are implanted with hydrogen, additional absorption peaks are observed beyond the usual 3437 and 2545 cm<sup>-1</sup> lines. As they are annealed, these defects become converted into the 3437 and 2545 cm<sup>-1</sup> lines at 400 °C. These lines are stable up to 700 °C where they are then converted into other new lines. All of these lines have the same polarization properties which suggests they have related structures.<sup>233</sup>

#### Summary for Ga<sub>2</sub>O<sub>3</sub>

EPR results of neutron irradiated, bulk samples suggested that octahedral gallium monovacancy defects were the main defects produced.<sup>225</sup> Proton irradiation introduces two main paramagnetic defects in Ga<sub>2</sub>O<sub>3</sub>, which are stable at room temperature.<sup>217,220–224</sup> The high introduction rate shows them to be primary defect related. Their g-tensor properties are characteristic for oxygen hole centers, but their g-tensor values are not compatible with the model of an

undistorted gallium monovacancy on a tetrahedral or an octahedral site (EPR1 center) or a self-trapped hole center (EPR2 center). The tetrahedral vacancy on the other hand has a complex lowest energy  $V_{\text{Ga(tetra)}} - \text{Ga}_i - V_{\text{Ga(tetra)}}$  configuration.<sup>220–224</sup>

Ingebrigtsen et al.<sup>220</sup> suggested that charge carrier removal can be explained by Fermi-level pinning far from the conduction band minimum (CBM) due to gallium interstitials (Ga<sub>i</sub>), vacancies (V<sub>Ga</sub>), and antisites (Ga<sub>O</sub>), while migration and subsequent passivation of V<sub>Ga</sub> via hydrogen-derived or V<sub>O</sub> defects may be responsible for the recovery. V<sub>O</sub> on the different crystallographic sites are deep donors with the (2+/0) transitions between 1.4–2.6 eV below the CBM for the distinct crystallographic O sites, with the shallowest levels corresponding to the four-fold coordinated O<sub>III</sub> site. Oxygen interstitials (O<sub>i</sub>) exhibit different site preferences and electronic behavior depending on the Fermi level. The split-interstitial configurations (O<sub>si</sub>) preferably form on the O<sub>i</sub> site and act as deep donors that are most favorable for Fermi levels up to approximately 1 eV below the CBM.<sup>221,222</sup> Above that, other interstitial configurations (O<sub>i</sub>) that behave as deep acceptors are favorable and are the preferred state in *n*-type conditions.<sup>223,224</sup> For proton irradiation, complete charge carrier compensation occurs for irradiation doses of  $\sim 10^{14} \text{ cm}^{-2}$ , implying little dynamic annealing of the generated defects. Most of the trapped charge carriers can be restored with relatively low temperature annealing.

Johnson et al.<sup>230</sup> employed direct microscopic observation of an unusual formation of point defect complexes in  $\beta$ -Ga<sub>2</sub>O<sub>3</sub> using high resolution scanning transmission electron microscopy (STEM). Each complex involves one cation interstitial atom paired with two cation vacancies. These divacancy–interstitial complexes are predicted by density functional theory to be compensating acceptors.

Kyrtsos et al.<sup>231</sup> reported that the migration barriers for the diffusion of the gallium vacancies are lower than the migration

barriers for oxygen vacancies by 1 eV on average, suggesting that the gallium vacancies are mobile at lower temperatures.

Figure 29 shows compilation of carrier removal rates in  $\text{Ga}_2\text{O}_3$  for different types and energy of radiation. The data reported to date shows that the carrier removal rates in  $\text{Ga}_2\text{O}_3$  are basically comparable to those in GaN.

**Diamond.**—The mechanisms for radiation damage in diamond are the same as in the other materials discussed in this review,<sup>245–267</sup> namely, neutrons create ballistic displacement of atoms, charged particles lose energy by creating displacements, ionization and phonons, whereas gammas lose energy by Compton scattering, which dominates up to  $\sim 20$  MeV, then pair production becomes significant. It is the scattered Compton electrons, or the electron-positron pairs, that do the damage. Gamma rays have very small cross-section for interaction.

Diamond-based radiation monitors are now routinely used in high-energy physics experiments such as at the Large Hadron Collider (LHC).<sup>245,247</sup> They are used to provide a precision measurement of the luminosity of the accelerator and detect particles close to an interaction point at the LHC. Diamond detectors are exposed to hadron fluences of up to  $1.5\text{--}3 \times 10^{16} \text{ cm}^{-2}$  during a 5- to 10-year operation.<sup>245,250,253</sup> Diamond has a minimum lattice displacement energy of 43 eV compared to Si with 25 eV. The radiation tolerance of diamonds grown by CVD to 70 MeV protons, fast reactor neutrons (energy  $> 0.1$  MeV), or 200 MeV pions has been reported.<sup>247</sup> By calculating the damage constant for these different types of radiation, it was found that 70 MeV protons are 2.60 times more damaging than 24 GeV protons, fast reactor neutrons were 4.3 times more damaging than 24 GeV protons and 200 MeV pions are 3.2 times more damaging than 24 GeV protons. For proton irradiations, diamond was to be more radiation tolerant than Si, while a comparable radiation tolerance against neutrons was observed.

Radiation hardness studies of diamond detectors have measured the change in charge collection efficiency (CCE) after exposing it to a fluence of damaging particles.<sup>249–254</sup> The reduction of CCE was measured as a function of particle fluence ( $\Phi$ ) or displacement damage dose (Dd). The latter represents the total energy of incident particle spent on the non-ionizing processes per unit mass of detector material,<sup>266</sup>  $Dd = \Phi \cdot NIEL$ . At low fluence, the decrease is expressed as  $CE = 1 - K_{ef} \cdot Dd$ , where  $K_{ef}$  is the equivalent damage factor. The change of detector properties depends not only on the total number and type of damaging particles but also on detector geometry and distribution of defects and ionization created by irradiations. Thus, the damage factor is valid for one particular detector under particular experimental conditions.<sup>249–254</sup>

In diamond, the vacancy has an activation energy for migration of 2.3 eV and is immobile below  $\sim 850$  K.<sup>256–259</sup> The interstitial has an activation energy for migration of 1.6 eV and is immobile below  $\sim 600$  K. If irradiation is performed above  $\sim 850$  K, there should be no surviving primary damage. Annealing under stress can potentially be used to change the annealing rates of some defects relative to others. As seen in Fig. 30, interstitials disappear at  $\sim 600$  K by migration to traps, whereas vacancies disappear at  $\sim 900$  K, mainly by migration to N traps. Mainwood et al.<sup>256–259</sup> reported that polycrystalline CVD diamond shows much greater damage than single crystal diamond due to limited recombination of defects.<sup>261–267</sup> Similarly, the presence of N-doping increases the residual damage. A standard configuration of nitrogen in diamond is as a pair of nearest-neighbor nitrogen atoms. When an irradiated diamond is annealed at  $\sim 1000$  K, a vacancy becomes mobile and can react with this pair. This appears to retard recombination of irradiation -produced defects. The highest concentrations of  $\text{N}_V^-$  and  $\text{N}_2\text{V}^-$  produced were 72 ppm and 24 ppm respectively. The production of  $\text{N}_V^-$  and  $\text{N}_2\text{V}^-$  were both dose-limited.  $\text{N}_V^-$  started annealing out at approximately  $1400^\circ\text{C}$  and almost completely annealed after annealing at  $1600^\circ\text{C}$ , as shown in Fig. 31.<sup>267</sup>

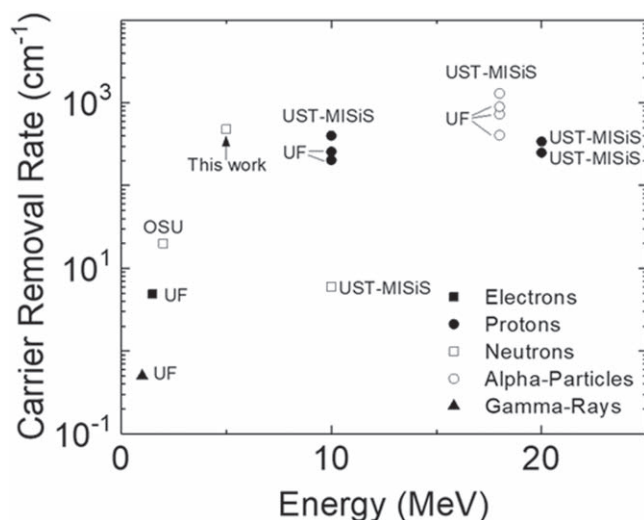


**Figure 29.** Carrier removal rates in  $\text{Ga}_2\text{O}_3$  as a function of energy for different forms of radiation.

**BN.**—Hexagonal boron nitride (h-BN) irradiated with 140 MeV protons to a fluence of  $\sim 6 \times 10^{20} \text{ p/cm}^2$  at  $\sim 200^\circ\text{C}$  was found to resist damage from bombardment at the doses impinging normal to the crystallographic planes (or along the crystallographic  $c$ -axis).<sup>268</sup> High dose irradiation appeared to cause shifting of phase transitions over temperature regimes that  $\text{h-BN} \rightarrow \text{w-BN}$  transitions occur.<sup>269,270</sup> Klein<sup>271</sup> reported the pressure phase transition from h-BN to wurtzitic BN was effected by ion irradiation. Irradiation with energetic  $\text{Au}^+$  results in a phase transition at a considerably lower pressure than for non-irradiated hBN samples, though the initial pressure for the transformation is not affected by heavy ion bombardment.<sup>272–274</sup> Cubic BN has a high degree of radiation hardness, up to fluences of  $\sim 1.5 \times 10^{13} \text{ ions cm}^{-2}$ . Neither hBN and cBN amorphize by ion bombardment at this fluence.

Hexagonal boron nitride neutron damaged at an integral flux of  $2.40 \times 10^{12} \text{ n cm}^{-2} \text{ s}^{-1}$  for up to 4 hours underwent a transition from  $\text{sp}^2$  to  $\text{sp}^3$  hybridization as a consequence of the neutron induced damage with the formation of cubic boron nitride (c-BN) spots.<sup>272–274</sup> In addition to c-BN, also a certain degree of amorphization was achieved by h-BN at a neutron fluence of  $8.64 \times 10^{15} \text{ n cm}^{-2}$ . The Wigner or stored energy in the radiation-damaged h-BN showed the neutron damage was partly irreversible and insensitive to the thermal annealing up to  $630^\circ\text{C}$ . Electron spin resonance (ESR) found two kinds of paramagnetic defective structures centered on  $^{11}\text{B}$  atoms.<sup>272–274</sup>

There has also been anecdotal evidence that neutron irradiated BN becomes more fragile. The weakening is attributed to the production of helium and hydrogen via the  $(n, \alpha)$ ,  $(n, p)$ ,  $(p, \alpha)$ , and  $(p, p)$  reactions. In the case of boron there is a particularly large  $(n, \alpha)$  cross section for the boron-10 isotope, which makes up approximately 20% of natural boron.

**Current testing standards.**—Table VI shows a selection of some existing testing standards or guidelines from the major industry standards associations. Noteworthy is the fact that many of these are more than 10 years old and it would be a worthwhile effort to revisit the status of some of these and to make new standards, given the rapid changes in materials and device technologies. Currently, the main options prior to radiation testing are to search databases such as the ESA Components Radiation Effects Database, the NASA GSFC and NASA JPL databases, as well as recent Nuclear and Space Radiation Effects Conference Proceedings published annually in the December issues of the IEEE Transactions on Nuclear Science, and the RADECS proceedings and the Radiation Data Workshops from NSREC and RADECS. These may give some

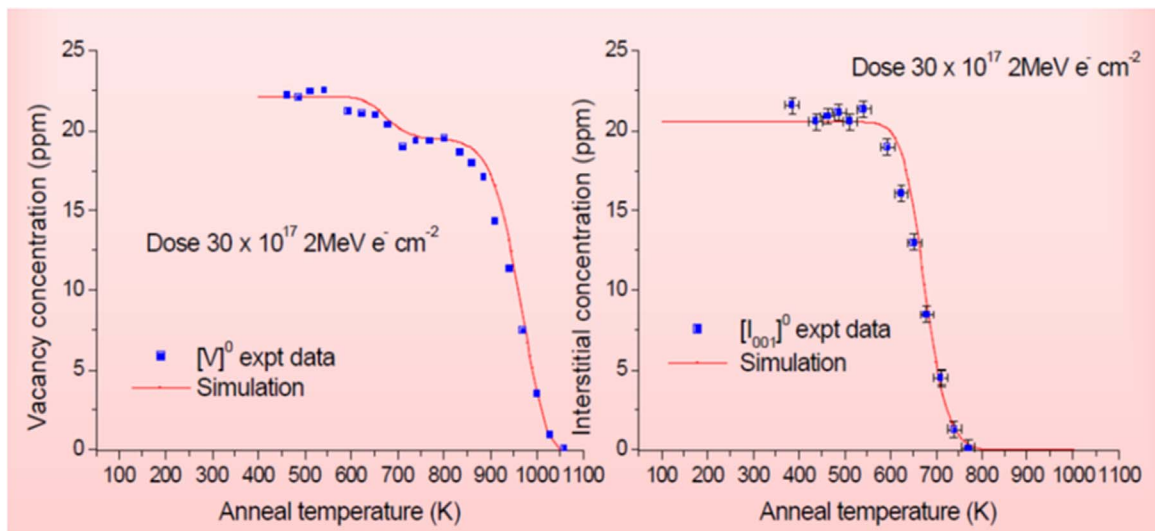


**Figure 30.** Vacancy and interstitial concentrations in electron irradiated diamond as a function of annealing temperature (adapted from “The mechanisms of radiation damage of diamond,” Alison Mainwood, Mark Newton and Brendan Campbell, presented at 1st Workshop on Radiation hard semiconductor devices for very high luminosity colliders, CERN 28–30 November, 2001).

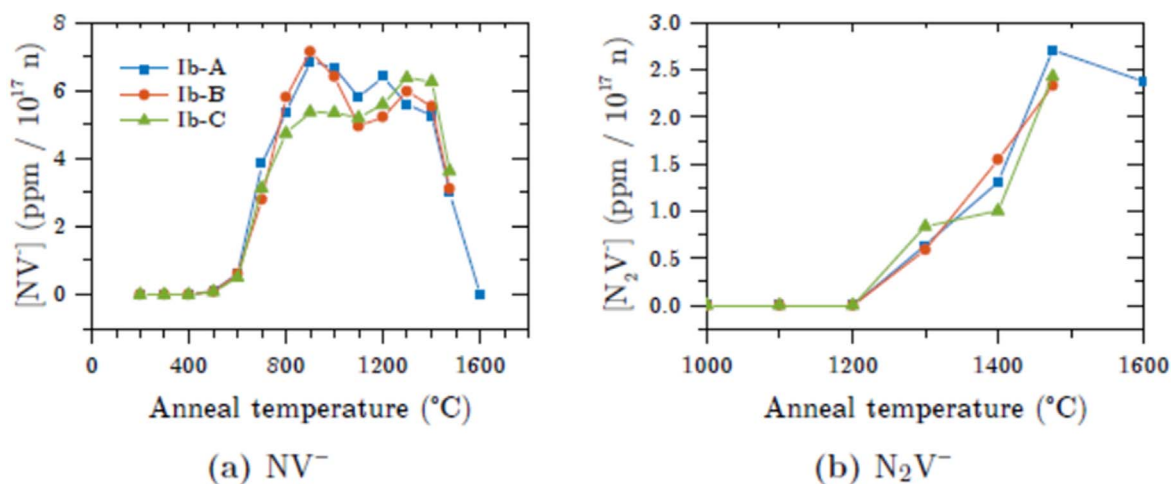


**Figure 31.** Concentration of NV<sup>−</sup> (a) and N<sub>2</sub>V<sup>−</sup> (b) determined by EPR. The concentrations have been normalized to the neutron dose to illustrate the dose dependence. (after dissertation of M.W. Dale,<sup>262</sup> University of Warwick URL: <http://wrap.warwick.ac.uk/80044>).

recent information as to the likely trends to be encountered, but this is a fragmented situation and having a sustained effort to standardize radiation testing would be welcome for device manufacturers whose products are to be utilized in terrestrial or space radiation environments.

### Conclusions

For radiation studies in the wide and ultra-wide bandgap semiconductors, there still remains a lack of standardized testing and differences in nomenclature between specialists and device technologists. There do not appear to be any show-stoppers in either total displacement dose or TID regimes in any of the wide bandgaps. For ionizing particles such as protons, electrons and  $\alpha$  particles, the damage region contains traps which reduce conductivity and  $\mu$  and at high enough doses, severe degradation of devices. By contrast, neutron irradiation creates Gossick zones- displacement damage from the other forms of radiation more typically point defects. In all technologies, gamma rays degrade only MOS structures under most conditions. There is a paucity of SEE data on wide bandgap devices and a lack of biased TDD and TID data on devices.

For SiC, the response of SiC diodes to particle radiation is different to Si power diodes.<sup>65,71,74,75</sup> SiC Schottky power diodes exhibit SEB, as in Si, but at biases below the SEB threshold. SiC Schottky devices exhibit gradual degradation under heavy-ion exposure, making evaluation of effects such as SEB more difficult.<sup>93–103</sup> Gradual leakage current increases are typically observed with increasing heavy-ion fluence, and are a function of the ion current and bias voltage during exposure. TCAD simulations suggest degradation occurs due to a thermal spike generated by synergy of heavy-ion strike and applied  $V_B$ . Heavy ion-induced SEB in 1200-V SiC power MOSFETs exhibits a decrease in SEB onset voltage for linear energy transfers  $>10 \text{ MeV cm}^{-2} \text{ mg}^{-1}$ . TCAD simulations show the origin is that a parasitic bipolar junction transistor turn-on creates carrier avalanche, resulting in catastrophic SEB. However, experimentally it is now believed that the failure is caused by heating in a small volume, leading to high temperatures and lattice damage (not a parasitic BJT feedback). Ion-induced leakage current degradation, and single-event burnout may be manifestations of the same device mechanisms in both SiC power diodes and MOSFETs. In all cases there is a migration of the electrical field from the front body-drain interface to the back

**Table VI. Examples of current radiation testing standards.**

Type of Test	Organization	Existing Standard, Guidelines or Method	Year Established
SEE proton testing	JEDEC	JESD234 Test Standard for the Measurement of Proton Radiation SEE in Electronic Devices	2013
Recommended method for measuring $\alpha$ -emissivity in materials utilized in manufacturing of semicon- ductors	ESCC	ESCC 25100 SEE Test Method and Guidelines	2014
	JEDEC Solid State Technology Association	JESD 221 Alpha Radiation Measurements in Electronic Materials	2011
Testing SEE for Terrestrial Effects	JEDEC Solid State Technology Association	JESD89 Measurement and Reporting of $\alpha$ Particle and Terrestrial Cosmic Ray-Induced Soft Errors in Semiconductor Devices	2005, addenda 2007
SEE Heavy Ion Testing	ASTM	ASTM F1192–11 Standard Guide for the Measurement of Single Phenomena Induced by Heavy Ion Irradiation of Semiconductor Devices	2018
	JEDEC Solid State Technology Association	JESD57 Test Procedures for the Measurement of SEE in Semiconductor Devices from Heavy Ion Irradiation	currently in revision
	ESCC	ESCC25100 Single Event Effects Test Method and Guideline	2014
SEB/SEGR Heavy Ion Test	MIL-STD	MIL-STD-750, Method 1080 Single Event Burnout and Single Event Rupture	2007
Neutron-Induced Displacement Damage in Si and GaAs Devices	ASTM	ASTM E1854-19 Standard Practice for Ensuring Test Consistency in Neutron-Induced Displacement Damage of Electronic Parts	2019
Annealing of Neutron-Induced Damage in Si Devices	ASTM	ASTM F980-16 Standard Guide for Measurement of Rapid Annealing of Neutron-Induced Displacement Damage in Si Devices	2016
Characterization of Particle Irradiation of Materials in Terms of NIEL	ASTM	ASTM E3084-17 Standard Practice for Characterizing Particle Irradiations of Materials in Terms of Non-Ionizing Energy Loss (NIEL)	2017
Exposure of Si or GaAs Components (ICs, transistors, and diodes) to Neutron Radiation	ASTM	ASTM F1190-18 Standard Guide for Neutron Irradiation of Unbiased Electronic Components	2018



epi-drain  $n^+$  interface, with a peak exceeding the critical electric field of SiC. This leads to avalanche generation, which enables high short-duration power densities during an approximate 20 psec window after the ion strike. The degradation effect in junction barrier Schottky SiC diodes seems to be independent of the length of the epitaxial region for different voltage-rated diodes. Heavy-ion data suggest that a common mechanism is responsible for SEB in 1200-V power MOSFETs and JBS diodes. Similarly, heavy-ion data suggest a common mechanism is also responsible for leakage current degradation in both devices. This mechanism, based on ion-induced, highly localized energy pulses, is demonstrated in simulations and shown to be capable of causing degradation and SEB for both the MOSFETs and JBS diodes.

For GaN, older results in the literature appear to be dominated by defects/impurities in starting epi, leading to differences between HEMTs processed in different labs. This has been a major drawback to GaN studies and emphasizes the need for controlled studies in state-of-the-art material with quantified purity and uniformity. The carrier removal rate by protons, electrons and neutrons in heterostructures increases in sequence  $\text{AlN/GaN} < \text{AlGaIn/GaN} < \text{InAlN/GaN}$ , consistent with average bond strengths. Proton damage in AlGaIn/GaN HEMTs results in reductions in mobility and increases in threshold voltage that lead to reductions in peak transconductance and drain current. The reduction in mobility can be much greater in magnitude than the changes in the other parameters, e.g., Liu et al.<sup>132</sup> measured 40% reduction in mobility and only a 0.1 V shift (3% change) in threshold voltage and 13% reduction in drain saturation current for a specific case of proton radiation. In other cases, there is a reported decrease in carrier concentration by a factor of two and a decrease in mobility by a factor of a thousand.<sup>129,130</sup>

The carrier removal rate for protons and electrons are accounted for by introduction of simple defects.<sup>135–142</sup> Defects created at the interface in HEMTs introduce scattering centers near the 2DEG, leading to a decrease in  $\mu$  and traps that result in a reduction in  $n_s$ , which causes a reduction in  $I_s$  and  $g_m$ , and an increase in  $R_{ON}$ , and positive threshold voltage shift.<sup>143–153</sup> MOSHEMTs are found to degrade at the same rate as metal gate HEMTs for protons and electrons. There is no evidence of enhanced-low-dose-rate sensitivity (ELDRS) in GaN. Generally, semi-ON or ON-state bias condition leads to greater  $V_T$  shifts and  $g_m$  degradation than unbiased proton irradiation. There is a need for combined irradiation/voltage-stress tests for space applications. For gamma irradiation, the populations of radiation-induced defects and their charge states evolve over periods of days, even at room temperature. This leads to conflicting results in the literature, such as in Schottky diodes, where it has been observed that gamma-rays induced changes to current-voltage characteristics, ideality factor, and point defects. Some studies report an increase in leakage current after doses around 200 kGy, but smaller doses of 30 kGy showed decreases in this current. Similarly, after irradiation, the ideality factor can exhibit increases, decreases or no change. Thus, attention must be paid to the time elapsed between irradiation and characterization.

Radiation damage in diamond is more significant for low energetic protons, neutrons, alphas and MeV ions. Defect recombination is efficient and independent of knock-on energy, with only 50% of displacements resulting in defects.<sup>275,276</sup> Diamond-based detectors should withstand a high radiation environment maintaining its unique properties such as fast response, collection efficiency, energy resolution. Radiation hardness is a fundamental property of this material.

There are only a few studies in BN and more detailed results await advances in bulk crystal synthesis.

Overall, there is still a lack of single event studies and an understanding of how irradiation alters the breakdown mechanism in new commercialized structures such as SiC and GaN vertical power diodes. As shown in Fig. 32, breakdown may occur because of impact ionization of atoms by carriers, or by tunneling or direct impact ionization of trap states. The first of these typically has a

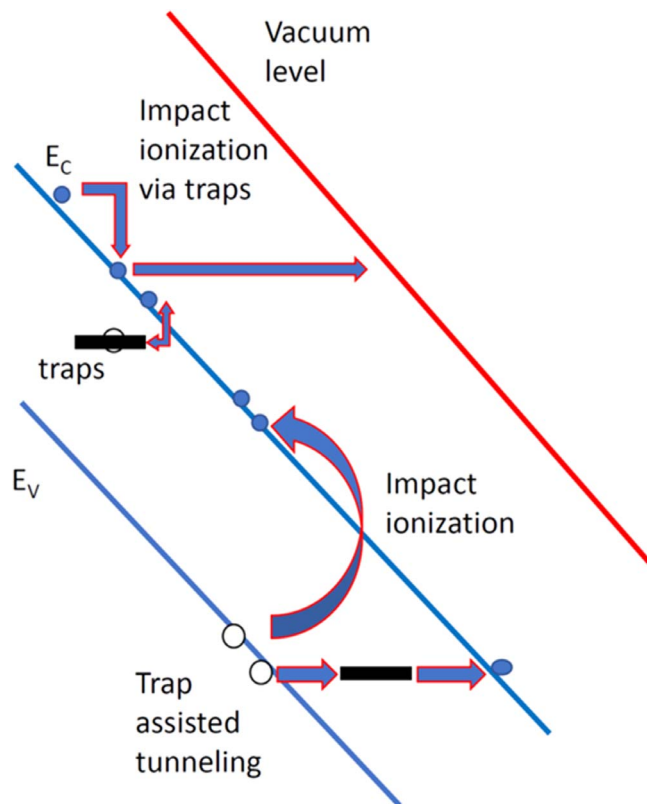


**Figure 32.** Schematic of common breakdown mechanisms in wide bandgap semiconductors. The current under reverse bias condition can increase due to avalanche multiplication from impact ionization, by tunneling or by ionization of trap states.

positive coefficient of temperature, so that the reverse breakdown increases with temperature. As defects are introduced by irradiation, it would be expected that this temperature coefficient will switch to negative as the breakdown mechanism changes to tunneling of defect ionization. More studies of total dose exposures under biased conditions, and a search for enhanced-low-dose-rate-sensitivity (ELDRS) in an ionizing radiation environment.<sup>275</sup> The low dose rate enhancement factor (LDR EF), which is the ratio of the relative degradation at low and high dose rate, is a standard figure-of-merit for ELDRS and has not been established for the wide bandgap and ultra-wide bandgap semiconductor devices. The device is considered ELDRS sensitive if the EF for any parameter is  $>1.5$ , according to the current U.S. military test standard. Finally, the coupled effects of electronic and nuclear energy deposition on damage accumulation in ion irradiated wide bandgap and ultra-wide bandgap semiconductors needs to be more fully understood.<sup>272–279</sup>

Finally, we propose a list of areas where more research is needed for the wide bandgap materials, that can also be eventually applied to the ultra-wide bandgap semiconductors as their technology matures. Avionics are susceptible to degradation, transient upset and eventual failure due to radiation effects from energetic particles from the cosmic ray flux and solar radiation.<sup>280,281</sup> These are classed as total ionizing dose (TID), displacement damage dose (DDD) and the instantaneous response of the electronics to single ionizing particles, called single-event effects (SEEs). Radiation testing of electronics is costly and time-consuming, and there is a limit to how much “hardening” can be employed due to weight and performance tradeoffs. A recent National Academies study<sup>282</sup> recommended stabilized funding for radiation test facilities, joint roadmap development by commercial device suppliers and reinvigoration of the workforce. For avionics, the numbers are stark- even when there is no significant space weather, high-latitude flights produce a dose rate analogous to a chest X-ray every 12.5 h, every 25 h for midlatitudes,

and every 100 h for equatorial latitudes at flight altitudes of 37,000 ft (~11 km). The dose rate doubles every 2 km altitude increase.<sup>280,281</sup>

In Si technology, BJTs with pn junctions are easier to damage compared to MOSFETs, digital applications are more readily disrupted, and small gate dimension FETs tolerate lower doses of radiation. With MOSFETs, there are I-V shifts due to charge generated in the gate oxide and threshold voltage shifts due to interface state increase. What is missing to establish the same level of understanding in wide bandgap semiconductors? These are questions that need additional research.<sup>283–294</sup>

1. what is the effect of mixed radiation environments more typical of what avionics will encounter?
2. what is the effect of temperature on SEE response?
3. what are the “intrinsic” carrier removal rates in SiC and GaN as a function of radiation type?
4. what information is needed to update the relevant MIL, JEDEC, ASTM and ESCC standards to make them relevant to modern avionics?
5. in power devices, are MOSFETs more easily damaged than rectifiers?
6. what is the role of hydrogen, either in gate dielectrics or in forming defect-H complexes?
7. what are the latent damage effects of ion testing?
8. Is there a synergistic effect between total dose and SEE, through increased off-state leakage due to cumulative ion strikes below disruption threshold?
9. what is the worst-case ion condition for SEE testing?
10. does gate stress in rf devices exacerbate dose or ion effects?
11. is barrier height lowering caused by heat generation during heavy ion irradiation a significant effect in SiC and GaN rectifiers?
12. what is worst case: static or dynamic mode operation?
13. are there any device specifications (e.g. the electric field profile, contact metal) that act as “predictors” of more severe radiation effects?
14. does electrical aging increase susceptibility to radiation-induced failure?
15. are there new experimental and computational studies on atomic and electronic defects in SiC and GaN, and certainly on the ultra-wide bandgap semiconductors, that will complete our understanding of defect generation, defect energy levels and threshold displacement energies?
16. what are the threshold displacement energies for the ultra-wide bandgap semiconductors?<sup>293,294</sup>
17. can we develop an improved potential to take into account energy partitioning that occurs to fairly low energies in these materials?<sup>289,290</sup> A significant portion of the primary knock-on atom energy can go to electrons, rather than displacements.
18. can we develop new modeling approaches that cover not only total dose effects due to defect generation from ballistic displacement, but more understanding of the SEEs that occur from heavy ions or pulsed lasers. These involves high electronic excitation densities and significant thermal spikes.<sup>288–294</sup> The thermal spikes from ions and lasers can be simulated using two-temperature MD approaches, but high electronic excitation densities that survive the thermal spike are currently a challenge.

### Acknowledgments

Work performed as part of Interaction of Ionizing Radiation with Matter University Research Alliance (IIRM-URA), sponsored by the Department of the Defense, Defense Threat Reduction Agency under award HDTRA1-20-2-0002. The content of the information does not necessarily reflect the position or the policy of the federal government, and no official endorsement should be inferred. The work at

NRL was partially supported by the Office of Naval Research. The work at Korea University was supported by the National Research Foundation (NRF) of Korea (2020M3H4A3081799) and by the Korea Institute of Energy Technology Evaluation and Planning (20172010104830). The work at NUST MISiS was supported in part by Grant № K2-2020-011 under the Program to increase Competitiveness of NUST MISiS among the World Leading Scientific and Educational centers (Program funded by the Russian Ministry of Science and Education). The authors at UF acknowledge informative discussions with Prof. William Weaver of University of Tennessee on many aspects of energy loss processes.

### ORCID

S. J. Pearton  <https://orcid.org/0000-0001-6498-1256>

Adrian Ildelfonso  <https://orcid.org/0000-0003-0533-3982>

A. Y. Polyakov  <https://orcid.org/0000-0001-6898-6126>

Jihyun Kim  <https://orcid.org/0000-0002-5634-8394>

### References

1. US Energy Information Administration, <https://www.eia.gov/energyexplained/us-energy-facts/>.
2. H. Amano, Y. Baines, E. Beam, M. Borga, T. Bouchet, P. R. Chalker, M. Charles, K. J. Chen, N. Chowdhury, and R. Chu, *J. Phys. D: Appl. Phys.*, **51**, 163001 (2018).
3. Y. Zhang, A. Dadgar, and T. Palacios, *J. Phys. D: Appl. Phys.*, **51**, 273001 (2018).
4. J. Y. Tsao et al., *Adv. Electron. Mater.*, **4**, 1600501 (2018).
5. A. Sharma, S. J. Lee, Y. J. Jang, and J. P. Jung, *J. Microelectron. Packag. Soc.*, **21**, 71 (2014).
6. E. Ahmadi and Y. Oshima, *J. Appl. Phys.*, **126**, 160901 (2019).
7. E. A. Jones, F. F. Wang, and D. Costinett, *IEEE J. Emerg. Sel. Top. Power Electron.*, **4**, 707 (2016).
8. N. Keshmiri, D. Wang, B. Agrawal, R. Hou, and A. Emadi, *IEEE Access*, **8**, 70553 (2020).
9. S. Das, L. D. Marilino, and K. O. Armstrong, *Wide Bandgap Semiconductor Opportunities in Power Electronics; Technical Report* (Oak Ridge National Laboratory (ORNL): Oak Ridge, TN, USA) (2018).
10. X. Huang et al., *Nanotechnology*, **30**, 215201 (2019).
11. F. F. Wang and Z. Zhang, *CPSS Trans. Power Electron. Appl.*, **1**, 13 (2016).
12. H. Fu, K. Fu, and Y. Zhao, *Vertical GaN-on-GaN Power Devices, in Wide Bandgap Semiconductor-Based Electronics*, ed. F. Ren and S. J. Pearton (IOP, Bristol, UK) (2020).
13. M. Kim, J. H. Seo, U. Singiseti, and Z. Ma, *J. Mater. Chem. C*, **5**, 8338 (2017).
14. J. Ballestín-Fuertes, J. Muñoz-Cruzado-Alba, J. F. Sanz-Osorio, and E. Laporta-Puyal, *Electronics*, **10**, 677 (2021).
15. K. J. Chen, O. Haberen, A. Lidow, C. L. Tsai, T. Ueda, Y. Uemoto, and Y. Wu, *IEEE Trans. Electron Devices*, **64**, 779 (2017).
16. R. J. Kaplar, A. A. Allerman, A. M. Armstrong, M. H. Crawford, J. R. Dickerson, A. J. Fischer, A. G. Baca, and E. A. Douglas, *ECS J. Solid State Sci. Technol.*, **6**, Q3061 (2017).
17. H. Fu, X. Zhang, X. Huang, I. Baranowski, H. Chen, Z. Lu, J. Montes, and Y. Zhao, *IEEE Electron Device Lett.*, **38**, 1286 (2017).
18. H. Umezawa, *Mater. Sci. Semicond. Process.*, **78**, 147 (2018).
19. M. Kasu, *Prog. Cryst. Growth Charact. Mater.*, **2016**, 317 (2016).
20. H. Zhang, L. Yuan, X. Tang, J. Hu, J. Sun, Y. Zhang, Y. Zhang, and R. Jia, *IEEE Trans. Power Electron.*, **35**, 5157 (2020).
21. S. Sharma, K. Zeng, S. Saha, and U. Singiseti, *IEEE Electron Device Lett.*, **41**, 836 (2020).
22. United States Space Force, Space Power, Space Capstone Publication, June 2020. [https://www.spaceforce.mil/Portals/1/Space%20Capstone%20Publication\\_10%20Aug%202020.pdf](https://www.spaceforce.mil/Portals/1/Space%20Capstone%20Publication_10%20Aug%202020.pdf).
23. United States Air Force, Science and Technology Strategy, April 2019, <https://cdn.afresearchlab.com/wp-content/uploads/2019/01/13192817/Air-Force-Science-and-Technology-Strategy.pdf>.
24. D. M. Fleetwood, “Radiation effects in a post-moore world.” *IEEE Trans. Nucl. Sci.* (in Press) (2021).
25. R. S. Averbach and T. Diaz de la Rubia, “Displacement damage in irradiated metals and semiconductors.”, ed. H. Ehrenfest and F. Spaepen *Solid State Phys.* vol 51, pages 281 (Academic, New York) (1998).
26. M. D. McCluskey and A. Janotti, *J. Appl. Phys.*, **127**, 190401 (2020).
27. K. Nordlund et al., *J. Nucl. Mater.*, **512**, 450 (2018).
28. A. V. Krashenninnikov and K. Nordlund, *J. Appl. Phys. (Applied Physics Reviews)*, **107**, 071301 (2010).
29. K. Nordlund, *J. Nucl. Mater.*, **520**, 273 (2019).
30. G. Was, *Fundamentals of Radiation Materials Science* (Springer, Berlin) (2012).
31. M. C. Sequeira et al., *Commun. Phys.*, **4**, 51 (2021).
32. S. M. Seltzer, D. Bartlett, D. Burns, G. Dietze, H. Menzel, H. Paretzke, and A. Wambersie, “Fundamental quantities and units for ionizing radiation revised.” *Journal of the International Commission of Radiation Units and Measurements*, **11**, 1 (2011), ICRU Report 85a.

33. Y. Richard, D. Guzman, and D. Smith, "In-flight experience and results of the PROBA-V low cost X-Band HDR-TM Transmitter." *The 45 Symposium 2014I-14* (2014).
34. W. J. Weber, D. M. Duffy, L. Thomé, and Y. Zhang, *Curr. Opin. Solid State Mater. Sci.*, **19**, 1 (2015).
35. Y. Zhang, X. Xiang, J. L. Rausch, X. T. Zu, and W. J. Weber, *IEEE Trans. Nuclear Sci.*, **56**, 920 (2009).
36. M. Sall, I. Monnet, F. Moisy, C. Grygiel, S. Jublot-Leclerc, S. Della-Negra, M. Toulemonde, and E. Balanzat, *J. Mater. Sci.*, **50**, 5214 (2015).
37. L. Nuckols, M. L. Crespillo, Y. Yang, J. Li, E. Zarkadoulas, Y. Zhang, and W. J. Weber, *Materialia*, **15**, 101023 (2021).
38. L. B. Bayu Aji, J. B. Wallace, and S. O. Kucheyev, *J. Applied Phys.*, **125**, 235706 (2019).
39. P. P. Hu et al., *Nucl. Instrum. Methods Phys. Res. B*, **430**, 59 (2018).
40. J. Montes, T. H. Yang, H. Fu, H. Chen, X. Huang, K. Fu, I. Baranowski, and Y. Zhao, *IEEE Trans. Nucl. Sci.*, **66**, 91 (2019).
41. A. Debelles, L. Thomé, I. Monnet, F. Garrido, O. H. Pakarinen, and W. J. Weber, *Phys. Rev. Mater.*, **3**, 063609 (2019).
42. L. Scheick, L. Selva, and H. Becker, *IEEE Trans. Nucl. Sci.*, **51**, 3193 (2004).
43. S. Kuboyama, C. Kamezawa, N. Ikeda, T. Hirao, and H. Ohyama, *IEEE Trans. Nucl. Sci.*, **53**, 3343 (2006).
44. S. Kuboyama, C. Kamezawa, Y. Satoh, T. Hirao, and H. Ohyama, *IEEE Trans. Nucl. Sci.*, **54**, 2379 (2007).
45. T. Makino, M. Deki, N. Iwamoto, S. Onoda, N. Hoshino, H. Tsuchida, T. Hirao, and T. Ohshima, *IEEE Trans. Nucl. Sci.*, **60**, 2647 (2013).
46. A. Kuramata, K. Koshi, S. Watanabe, Y. Yamaoka, T. Masui, and S. Yamakoshi, *Jpn. J. Appl. Phys.*, **55**, 1202A2 (2016).
47. S. J. Pearton, F. Ren, M. Tadjer, and J. Kim, *J. Appl. Phys.*, **124**, 220901 (2018).
48. A. Hassa, P. Storm, M. Kneiß, D. Splith, H. von Wenckstern, M. Lorenz, and M. Grundmann, *Physica Status Solidi (b)*, **258**, 2000394 (2020).
49. A. Hassa, M. Grundmann, and H. von Wenckstern, "Progression of Group-III sesquioxides: epitaxy, solubility and desorption." *J. Phys. D: Appl. Phys.* (2020).
50. N. Ueda, N. Ikenaga, K. Koshi, K. Iizuka, A. Kuramata, K. Hanada, T. Moribayashi, S. Yamakoshi, and M. Kasu, *Jpn. J. Appl. Phys.*, **55**, 1202BD1 (2016).
51. Z. Galazka, R. Uecker, D. Klimm, K. Imscher, M. Naumann, M. Pietsch, A. Kwasniewski, R. Bertram, S. Ganschow, and M. Bickermann, *ECS J. Solid State Sci. Technol.*, **6**, Q3007 (2017).
52. S. I. Stepanov, V. I. Nikolaev, V. E. Bougrov, and A. E. Romanov, *Rev. Adv. Mater. Sci.*, **44**, 63 (2016).
53. M. A. Mastro, A. Kuramata, J. Calkins, J. Kim, F. Ren, and S. J. Pearton, *ECS J. Solid State Sci. Technol.*, **6**, 356 (2017).
54. M. Baldini, M. Albrecht, A. Fiedler, K. Imscher, R. Schewski, and G. Wagner, *ECS J. Solid State Sci. Technol.*, **6**, Q3040 (2017).
55. M. J. Tadjer et al., *J. Electr. Mater.*, **45** (2016), 2031 (2016).
56. S. Rafique, L. Han, M. J. Tadjer, J. A. Freitas Jr, N. A. Mahadik, and H. Zhao, *Appl. Phys. Lett.*, **108**, 182105 (2016).
57. J. B. Varley, J. R. Weber, A. Janotti, and C. G. Van de Walle, *Appl. Phys. Lett.*, **97**, 142106 (2010).
58. S. Rafique, L. Han, and H. Zhao, *ECS Trans.*, **80**, 203 (2017).
59. C. Abbate, G. Busatto, D. Tedesco, A. Sanseverino, L. Silvestrin, F. Velardi, and J. Wyss, *IEEE Trans. Electron Dev.*, **66**, 4235 (2019).
60. J. McPherson, *Mater. Sci. Forum*, **1004**, 889 (2020).
61. S. Kuboyama, *IEEE Trans. Nucl. Sci.*, **66**, 688 (2019).
62. H. Xue, Y. Zhang, and W. J. Weber, *Mater. Res. Lett.*, **5**, 494 (2017).
63. J.-M. Lauenstein, "Getting SiC power devices off the ground: design, testing, and overcoming radiation threats." *Microelectronics Reliability and Qualification Working (MRQW) Meeting*, El Segundo, CA, February 2018, <https://ntrs.nasa.gov/search.jsp?R=20180006113>.
64. L. B. Bayu Aji, J. B. Wallace, and S. O. Kucheyev, *Sci. Rep.*, **7**, 44703 (2017).
65. E. Mizuta, S. Kuboyama, H. Abe, Y. Iwata, and T. Tamura, *IEEE Transactions on Nuclear Sci.*, **61**, 1924 (2014).
66. K.-M. Lee and B.-G. Park, *IEEE Trans. Nuclear Science*, **67**, 1374 (2020).
67. R. D. Harris, A. J. Frasca, and M. O. Patton, *IEEE Trans Nuclear Science*, **52**, 2408 (2005).
68. S. J. Pearton, J. Yang, P. H. Cary IV, F. Ren, J. Kim, M. J. Tadjer, and M. A. Mastro, *Appl. Phys. Rev.*, **5**, 011301 (2018).
69. H. Von Wenckstern, *Adv. Electron. Mater.*, **3**, 1600350 (2017).
70. P. Hazdra, P. Smrkovský, J. Vobecký, and A. Mihaila, *IEEE Trans. Electron Devices*, **68**, 202 (2021).
71. L. Pengwei, Z. Liang, L. Xingji, Y. Jianqun, M. Bo, L. V. He, Y. Qingkui, T. Mi, and X. Weixin, "The investigation on drain-source on-state resistance of SiC power MOSFETs from single event effects experiment." *2018 International Conference on Radiation Effects of Electronic Devices (ICREED)*, Beijing, China p. 1 (2018), (10.1109/ICREED.2018.8905074).
72. S. S. Suvanam, L. Lanni, B. G. Malm, C. Zetterling, and A. Hallén, "Total dose effects on 4H-SiC bipolar junction transistors." *2016 European Conference on Silicon Carbide & Related Materials (ECSCRM)*, Halkidiki, p. 1 (2016), (10.4028/www.scientific.net/MSF.897.579).
73. P. P. Dong, X. Yan, L. Zhang, S. Jin, F. Dai, Y. Zhang, Y. Cui, X. Yu, and B. Huang, *IEEE Trans Nuclear Sci*, **68**, 312 (2021).
74. R. Devanathan, W. J. Weber, and F. Gao, *J. Appl. Physics*, **90**, 2303 (2001).
75. R. Devanathan, T. D. de la Rubia, and W. J. Weber, *J. Nuclear Materials*, **253**, 47 (1998).
76. R. K. Sharma, P. Hazdra, and S. Popelka, *IEEE Trans Nuclear Sci*, **62**, 534 (2015).
77. Y. Zhang, R. Sachan, O. H. Pakarinen, M. F. Chisholm, P. Liu, H. Xue, and W. J. Weber, *Nat. Commun.*, **6**, 1 (2015).
78. K. Imada, M. Ishimaru, H. Xue, Y. Zhang, S. C. Shannon, and W. J. Weber, *J. Nuclear Materials*, **478**, 310 (2016).
79. D. R. Ball et al., *IEEE Trans. Nuclear Science*, **66**, 337 (2018).
80. A. Khachatryan, N. J.-H. Roche, S. Buchner, A. D. Koehler, T. J. Anderson, V. Ferlet-Cavrois, M. Muschitiello, D. McMorro, B. Weaver, and K. D. Hobart, *IEEE Trans Nuclear Sci*, **62**, 2743 (2015).
81. A. Khachatryan, N. J.-H. Roche, S. P. Buchner, A. D. Koehler, T. J. Anderson, D. McMorro, S. D. Lalumondiere, J. P. Bonsall, E. C. Dillingham, and D. L. Brew, *IEEE Trans Nuclear Sci*, **66**, 368 (2019).
82. J. M. Hales et al., *IEEE Trans Nuclear Sci.*, **67**, 81 (2020).
83. A. Khachatryan, S. Buchner, A. Koehler, C. Affouda, D. McMorro, S. D. Lalumondiere, E. C. Dillingham, J. P. Bonsall, A. C. Scofield, and D. L. Brew, *IEEE Trans Nuclear Sci*, **66**, 1682 (2019).
84. A. Khachatryan, N. J. Roche, L. B. Ruppalt, J. G. Champlain, S. Buchner, A. D. Koehler, T. J. Anderson, K. D. Hobart, J. H. Warne, and D. McMorro, *IEEE Trans. Nucl. Sci.*, **65**, 269 (2018).
85. J. M. Hales et al., *IEEE Trans Nuclear Sci*, **64**, 1006 (2017).
86. A. Khachatryan et al., *2017 17th European Conference on Radiation and Its Effects on Components and Systems (RADECS)*.
87. A. Khachatryan, N. J.-H. Roche, S. P. Buchner, A. D. Koehler, J. D. Greenlee, T. J. Anderson, J. H. Warner, and D. McMorro, *IEEE Trans Nuclear Sci*, **63**, 1995 (2016).
88. J. M. Hales et al., *IEEE Trans Nuclear Sci*, **62**, 2867 (2015).
89. A. Akturk, J. M. McGarrity, S. Potbhare, and N. Goldsman, *IEEE Trans Nuclear Sci*, **59**, 3258 (2012).
90. R. D. Harris, A. J. Frasca, and M. O. Patton, *IEEE Trans. Nucl. Sci.*, **52**, 2408 (2005).
91. K. F. Galloway, A. F. Witulski, R. D. Schrimpf, A. L. Sternberg, D. R. Ball, D. R. Ball, A. Javanainen, R. A. Reed, and B. D. Sierawski, *Jean-Marie Lauenstein, Aerospace*, **5**, 67 (2018).
92. D. R. Ball et al., *IEEE Trans Nuclear Sci*, **67**, 22 (2020).
93. A. Javanainen et al., *IEEE Trans. Nuclear Sci*, **64**, 2031 (2017).
94. A. Javanainen, K. F. Galloway, V. Ferlet-Cavrois, and J. M. Lauenstein, *IEEE Trans. Device and Materials Reliability*, **16**, 208 (2016).
95. R. A. Johnson et al., *IEEE Trans. Nuclear Sci*, **67**, 135 (2020).
96. J. Lauenstein, P. G. Neudeck, K. L. Ryder, E. P. Wilcox, L. Chen, M. A. Carts, S. Y. Wrbanek, and J. D. Wrbanek, *2019 IEEE Radiation Effects Data Workshop, San Antonio, TX, USA*, p. 1 (2019).
97. A. F. Witulski et al., *Mater. Sci. Forum*, **1004**, 1066 (2020).
98. A. F. Witulski, D. R. Ball, K. F. Galloway, A. Javanainen, J.-M. Lauenstein, A. L. Sternberg, R. D. Schrimpf, R. A. Reed, and A. Virtanen, *IEEE Trans. Nuclear Sci*, **65**, 1951 (2018).
99. A. F. Witulski, R. Arslanbekov, A. Raman, R. D. Schrimpf, A. L. Sternberg, K. F. Galloway, A. Javanainen, D. Grider, D. J. Lichtenwalner, and B. Hull, *IEEE Trans Nuclear Sci*, **65**, 256 (2017).
100. J. Kim, S. Nigam, F. Ren, D. Schoenfeld, C. Y. Chung, and S. J. Pearton, *Electrochem. Solid-State Lett.*, **6**, G105 (2003).
101. R. A. Johnson et al., *IEEE Trans. Nucl. Sci.*, **66**, 1694 (2019).
102. S. Nigam et al., *Appl. Phys. Lett.*, **81**, 2385 (2002).
103. J. B. Wallace, L. Bayu Aji, T. Li, L. Shao, and S. O. Kucheyev, *J. Appl. Phys.*, **118**, 105705 (2015).
104. E. Wendler, M. Schulling, and L. Wendler, *Vacuum*, **105**, 102 (2014).
105. A. Azarov, A. Titov, P. A. Karasev, and A. Hallen, "Effect of collision cascade density on radiation damage in SiC." *Nucl. Instr. and Meth. B*, **267**, 1247 (2009).
106. W. J. Weber, L. Wang, N. Yu, and N. Hess, *Mater. Sci. Eng. A*, **253**, 62 (1998).
107. W. J. Weber and L. M. Wang, *Nucl. Instr. and Meth. B*, **106**, 298 (1995).
108. B. J. Cowen, M. S. El-Genk, K. Hattar, and S. A. Briggs, *J. Applied Phys.*, **126**, 135902 (2019).
109. S. J. Pearton, F. Ren, E. Patrick, M. E. Law, and A. Y. Polyakov, *ECS J. Solid State Sci. Technol.*, **5**, Q35 (2016).
110. C. Fares, F. Ren, S. J. Pearton, G. Yang, J. Kim, C. F. Lo, and J. Wayne Johnson, *J. Vac. Sci. Technol. B*, **36**, 052202 (2018).
111. I. H. Lee, A. Y. Polyakov, N. B. Smirnov, I. V. Shchemerov, P. B. Lagov, R. A. Zinov'ev, E. B. Yakimov, K. D. Shcherbachev, and S. J. Pearton, *J. Appl. Phys.*, **122**, 115704 (2017).
112. G. Yang, S. Jang, F. Ren, S. J. Pearton, and J. Kim, *ACS Applied Mater. Interfaces*, **9**, 04071 (2017).
113. A. Chatterjee, S. K. Khamari, S. Porwal, S. Kher, and T. K. Sharma, *J. Appl. Phys.*, **123**, 161585 (2018).
114. J. Xi, B. Liu, Y. Zhang, and W. J. Weber, *J. Applied Phys*, **123**, 045904 (2018).
115. Z. Bian et al., *J. Phys. Appl. Phys.*, **53**, 045103 (2020).
116. G. A. Umana-Membreno, J. M. Dell, G. Parish, B. D. Nener, and L. Faraone, *J. Appl. Phys.*, **101**, 054511 (2007).
117. S. A. Vitusevich et al., *Phys. Status Solidi a*, **195**, 101 (2003).
118. P. J. Martínez, E. Maset, P. Martín-Holgado, Y. Morilla, D. Gilabert, and E. Sanchis-Kilders, *Materials*, **12**, 17 (2019).
119. A. M. Kurakin, S. A. Vitusevich, S. V. Danylyuk, H. Hardtdegen, N. Klein, Z. Bougriva, B. A. Danilchenko, R. V. Konakova, and A. E. Belyaev, *J. Appl. Phys.*, **103**, 083707 (2008).
120. G. A. Umana-Membreno, J. M. Dell, T. P. Hessler, B. D. Nener, G. Parish, L. Faraone, and U. K. Mishra, *Appl. Phys. Lett.*, **80**, 4354 (2002).
121. V. V. Emtsev et al., *Semicond. Sci. Technol.*, **15**, 73 (2000).
122. C. Sharma, R. Singh, D.-S. Chao, and T.-L. Wu, *Semicond. Sci. Technol.*, **34**, 065024 (2019).



123. G. Gu Wenping, C. Chi, D. Huantao, and H. Yue, *J. Semicond.*, **30**, 044002 (2009).
124. O. Aktas, A. Kulieva, V. Kumara, R. Schwindt, S. Toshkov, D. Costescu, J. Stubbin, and I. Adesida, *Solid-State Electron.*, **48**, 471 (2004).
125. C. Schwartz, A. Yadav, M. Shatkin, E. Flitsiyan, L. Chernyak, V. Kasiyan, L. Liu, Y. Xi, F. Ren, and S. J. Pearton, *Appl. Phys. Lett.*, **102**, 062102 (2013).
126. I. H. Lee, A. Y. Polyakov, E. B. Yakimov, N. B. Smirnov, I. V. Shchemerov, S. A. Tarelkin, S. I. Didenko, K. I. Tapero, R. A. Zinovyev, and S. J. Pearton, *Appl. Phys. Lett.*, **110**, 112102 (2017).
127. S. Ahn, B. J. Kim, Y. H. Lin, F. Ren, S. J. Pearton, G. Yang, J. Kim, and I. Kravchenko, *J. Vac. Sci. Technol.*, **B34**, 051202 (2016).
128. B. J. Kim, S. Ahn, F. Ren, S. J. Pearton, G. Yang, and J. Kim, *J. Vac. Sci. Technol.*, **B34**, 041231 (2016).
129. Y. S. Hwang et al., *J. Vac. Sci. Technol. B*, **31**, 022206 (2013).
130. L. Liu, C. V. Cuervo, Y. Xi, F. Ren, S. J. Pearton, H. Y. Kim, J. Kim, and I. Kravchenko, *J. Vac. Sci. Technol. B*, **31**, 042202 (2013).
131. A. Y. Polyakov, S. J. Pearton, P. Frenzer, F. Ren, L. Liu, and J. Kim, *J. Mater. Chem. C*, **1**, 877 (2013).
132. S. J. Pearton, R. Deist, F. Ren, L. Liu, A. Y. Polyakov, and J. Kim, *J. Vac. Sci. Technol. A*, **31**, 050801 (2013).
133. H. Y. Kim, J. Kim, L. Liu, C. F. Lo, F. Ren, and S. J. Pearton, *J. Vac. Sci. Technol. B*, **31**, 051210 (2013).
134. Y. Xi et al., *J. Vac. Sci. Technol. B*, **32**, 012201 (2014).
135. X. Hu et al., *IEEE Trans Nuclear Sci*, **50**, 1791 (2003).
136. J. Kim, F. Ren, D. Schoenfeld, S. J. Pearton, A. G. Baca, and R. D. Briggs, *J. Semicond. Technol. Sci.*, **4**, 124 (2004).
137. R. Khanna, K. Allums, C. R. Abernathy, S. J. Pearton, J. Kim, F. Ren, R. Dwivedi, T. N. Fogarty, and R. Wilkins, *Appl. Phys. Lett.*, **85**, 3131 (2004).
138. A. Y. Polyakov, N. B. Smirnov, A. V. Govorkov, A. V. Markov, S. J. Pearton, N. G. Kolin, D. I. Merkurisov, and V. M. Boiko, *J. Appl. Phys.*, **98**, 033529 (2005).
139. R. Khanna, S. Y. Han, S. J. Pearton, D. Schoenfeld, W. V. Schoenfeld, and F. Ren, *Appl. Phys. Lett.*, **87**, 218547 (2005).
140. X. Hu, B. K. Choi, H. J. Barnaby, D. M. Fleetwood, R. D. Schrimpf, S. Lee, S. Shojah-Ardalan, and R. Wilkins, *Umesh K Mishra, Ross W Dettmer, IEEE Trans Nuclear Science*, **51**, 293 (2004).
141. A. P. Karmarkar, B. Jun, D. M. Fleetwood, R. D. Schrimpf, R. A. Weller, and B. D. White, *IEEE Trans Nuclear Sci.*, **51**, 3801 (2004).
142. A. Kalavagunta, M. Silvestri, M. J. Beck, S. K. Dixit, R. D. Schrimpf, R. A. Reed, D. M. Fleetwood, L. Shen, and U. K. Mishra, *IEEE Trans Nuclear Sci.*, **56**, 3192 (2009).
143. A. Polyakov, N. Smirnov, A. Govorkov, S. J. Pearton, and J. M. Zavada, *J. Appl. Phys.*, **94**, 3069 (2003).
144. A. Polyakov, N. Smirnov, A. Govorkov, N. Pashkova, S. J. Reicher, J. M. Zavada, and R. G. Wilson, *J. Vac. Sci. Technol.*, **B21**, 2500 (2003).
145. A. Y. Polyakov et al., *Appl. Phys. Lett.*, **93**, 152101 (2008).
146. A. Y. Polyakov, N. B. Smirnov, A. V. Govorkov, I.-H. Lee, J. H. Baek, N. G. Kolin, V. M. Boiko, D. I. Merkurisov, and S. J. Pearton, *J. Electrochem. Soc.*, **155**, H31 (2008).
147. K. K. Allums, M. Hlad, A. P. Gerger, B. P. Gila, C. R. Abernathy, S. J. Pearton, F. Ren, R. Dwivedi, T. N. Fogarty, and R. Wilkins, *J. Electron. Mater.*, **36**, 519 (2007).
148. O. Lopatiuk-Tirpak, L. Chernyak, Y. L. Wang, F. Ren, S. J. Pearton, K. Gartsman, and Y. Feldman, *Appl. Phys. Lett.*, **90**, 172111 (2007).
149. A. Y. Polyakov et al., *J. Electron. Mater.*, **36**, 1320 (2007).
150. C. F. Lo et al., *J. Vac. Sci. Technol. B*, **28**, L47 (2010).
151. E. Patrick, M. Choudhury, F. Ren, S. Pearton, and M. Law, *ECS J. Solid State Science and Technology*, **4**, Q21 (2015).
152. J. Chen, Y. S. Puzyrev, C. X. Zhang, E. X. Zhang, M. W. McCurdy, and D. M. Fleetwood, *IEEE Trans Nuclear Sci.*, **60**, 4080 (2013).
153. A. Kalavagunta, A. Touboul, L. Shen, R. D. Schrimpf, R. A. Reed, D. M. Fleetwood, R. K. Jain, and U. K. Mishra, *IEEE Trans. Nuclear Science*, **55**, 2106 (2008).
154. E. Mizuta, *IEEE Trans Nuclear Science*, **65**, 1956 (2018).
155. NASA SBIR 2021 Phase I Solicitation, Z1.06 Radiation-Tolerant High-Voltage, High-Power Electronics, <https://www.sbir.gov/node/1836217>.
156. A. Y. Polyakov et al., *J. Vac. Sci. Technol. B*, **24**, 2256 (2006).
157. A. Y. Polyakov, N. B. Smirnov, A. V. Govorkov, N. G. Kolin, D. I. Merkurisov, V. M. Boiko, A. V. Korulin, and S. J. Pearton, *J. Vac. Sci. Technol. B*, **28**, 608 (2010).
158. A. Y. Polyakov et al., *J. Appl. Phys.*, **100**, 093715 (2006).
159. A. Y. Polyakov, N. B. Smirnov, A. Govorkov, A. Markov, S. J. Pearton, N. Kolin, D. Merkurisov, V. Boiko, C. Lee, and I. H. Lee, *J. Vac. Sci. Technol.*, **B25**, 436 (2007).
160. A. Y. Polyakov et al., *J. Vac. Sci. Technol. B*, **30**, 061207 (2012).
161. C. Lo, L. Liu, F. Ren, H. Kim, J. Kim, S. J. Pearton, O. Laboutin, Y. Cao, J. W. Johnson, and I. Kravchenko, *J. Vac. Sci. Technol. B*, **29**, 061201 (2011).
162. C. F. Lo et al., *J. Vac. Sci. Technol. B*, **30**, 041206 (2012).
163. I. Lee, A. Polyakov, N. Smirnov, A. Govorkov, E. Kozhukhova, E. Yakimov, N. G. Kolin, V. Boiko, A. Korulin, and S. J. Pearton, *Appl. Phys. Lett.*, **98**, 212107 (2011).
164. I. Lee, A. Y. Polyakov, N. Smirnov, A. V. Govorkov, E. A. Kozhukhova, N. G. Kolin, V. M. Boiko, A. V. Korulin, and S. J. Pearton, *J. Electrochem. Soc.*, **158**, H866 (2011).
165. S. Li, Y. H. Hwang, Y. L. Hsieh, F. Ren, S. J. Pearton, E. Patrick, M. E. Law, C. V. Cuervo, and D. J. Smith, *J. Vac. Sci. Tech.*, **32**, 201203 (2014).
166. L. Liu, H. H. Hwang, Y. Xi, F. Ren, V. Craciun, S. J. Pearton, G. Yang, H. Y. Kim, and J. Kim, *J. Vac. Sci. Technol. B*, **32**, 022202 (2014).
167. A. Y. Polyakov, I.-H. Lee, N. B. Smirnov, A. V. Govorkov, E. A. Kozhukhova, N. G. Kolin, A. V. Korulin, V. M. Boiko, and S. J. Pearton, *J. Appl. Phys.*, **109**, 123703 (2011).
168. Y. H. Hwang et al., *J. Vac. Sci. Technol. B*, **32**, 031203 (2014).
169. I.-H. Lee, A. Y. Polyakov, N. B. Smirnov, A. V. Govorkov, E. A. Kozhukhova, N. G. Kolin, V. M. Boiko, A. V. Korulin, and S. J. Pearton, *J. Vac. Sci. Technol. B*, **29**, 041201 (2011).
170. M. Zerarka, *IEEE Trans Nuclear Science*, **64**, 2242 (2017).
171. C. Abbate, *Microelectron. Reliab.*, **55**, 1496 (2015).
172. K. F. Galloway, C. Nicklaw, A. L. Bossler, V. Ferlet-Cavrois, J.-M. Lauenstein, F. Pintacuda, R. A. Reed, R. D. Schrimpf, R. A. Weller, and A. Virtanen, *IEEE Trans Nuclear Science*, **64**, 415 (2016).
173. B. Luo et al., *Appl. Phys. Lett.*, **80**, 604 (2002).
174. B. Luo et al., *J. Electron. Mater.*, **31**, 437 (2002).
175. J. Kim et al., *Electrochem. Sol. State Lett.*, **5**, G57 (2002).
176. B. Luo et al., *Electrochem. Solid-State Lett.*, **6**, G31 (2003).
177. B. Luo et al., *Appl. Phys. Lett.*, **82**, 1428 (2003).
178. B. Luo et al., *Solid-State Electron.*, **47**, 1015 (2003).
179. T. J. Anderson, A. D. Koehler, J. D. Greenlee, B. D. Weaver, M. A. Mastro, J. K. Hite, C. R. Eddy, F. J. Kub, and K. D. Hobart, *IEEE Electron Device Lett.*, **35**, 826 (2014).
180. S. J. Pearton, Y.-S. Hwang, and F. Ren, *J. Mater.*, **67**, 1359 (2015).
181. E. B. Yakimov, P. S. Vergeles, A. Y. Polyakov, I.-H. Lee, and S. J. Pearton, *Appl. Phys. Lett.*, **106**, 132101 (2015).
182. B. D. Weaver, T. J. Anderson, A. D. Koehler, J. D. Greenlee, J. K. Hite, D. I. Shahin, F. J. Kub, and K. D. Hobart, *ECS J. Solid State Sci. Technology*, **5**, Q208 (2016).
183. E. Patrick, M. Choudhury, F. Ren, S. J. Pearton, and M. E. Law, *ECS J. Solid State Sci. Technol.*, **4**, Q21 (2015).
184. L. Chernyak, A. Yadav, E. Flitsiyan, Y.-H. Hwang, Y.-L. Hsieh, L. Lei, F. Ren, and S. J. Pearton, *Rad. Effects and Defects in Solids*, **170**, 225 (2015).
185. J. D. Greenlee, P. Specht, T. J. Anderson, A. D. Koehler, B. D. Weaver, M. Luysberg, O. D. Dubon, F. J. Kub, T. R. Weatherford, and K. D. Hobart, *Appl. Phys. Lett.*, **107**, 083504 (2015).
186. T. Anderson, A. Koehler, Y.-H. Hwang, Y.-L. Hsieh, S. Li, F. Ren, J. W. Johnson, and S. J. Pearton, *J. Vac. Sci. Technol. B*, **32**, 051203 (2014).
187. A. D. Koehler, T. J. Anderson, M. J. Tadjer, B. D. Weaver, J. D. Greenlee, D. I. Shahin, K. D. Hobart, and F. J. Kub, *IEEE Electron Dev. Lett.*, **37**, 545 (2016).
188. Y. S. Puzyrev, T. Roy, E. X. Zhang, D. M. Fleetwood, R. D. Schrimpf, and S. T. Pantelides, *IEEE Trans Nuclear Science*, **58**, 2918 (2011).
189. A. D. Koehler et al., *IEEE Electron Device Lett.*, **35**, 1194 (2015).
190. J. Chen, Y. S. Puzyrev, R. Jiang, E. X. Zhang, M. W. McCurdy, and D. M. Fleetwood, *IEEE Trans Nuclear Science*, **62**, 2423 (2015).
191. Z. Zhang, A. R. Arehart, E. Cinkilic, J. Chen, E. X. Zhang, D. M. Fleetwood, R. D. Schrimpf, B. McSkimming, J. S. Speck, and S. A. Ringel, *Appl. Phys. Lett.*, **103**, 042102 (2013).
192. K. Ahn, Y. K. Ooi, F. Mirkhosravi, J. Gallagher, A. Lintereur, D. Feezell, E. K. Mace, and M. A. Scarpulla, "Differences in electrical responses and recovery of GaN p-n diodes on sapphire and freestanding GaN subjected to high dose 60Co gamma-ray irradiation." *J. Appl. Phys.*, .
193. The Stopping and Range of Ions in Matter, <http://www.srim.org/index.htm>.
194. P. H. Carey IV, F. Ren, J. Bae, J. Kim, and S. J. Pearton, *ECS J. Solid State Sci. Technol.*, **9**, 025003 (2020).
195. J. C. Petrosky, *IEEE Trans. Nucl. Sci.*, **56**, 2905 (2009).
196. P. H. Carey IV, F. Ren, A. M. Armstrong, B. A. Klein, A. A. Allerman, E. A. Douglas, A. G. Baca, J. Bae, J. Kim, and S. J. Pearton, *ECS J. Solid State Sci. Technol.*, **9**, 035008 (2020).
197. Z. Islam, N. Glavin, and A. Haque, "Potentials and challenges of in situ microscopy on electronic devices and materials." *Wide Bandgap Semiconductor-Based Electronics*, ed. F. Ren and S. J. Pearton (IOP Publishing, Bristol, UK) (2020).
198. Z. Islam, A. Haque, and N. Glavin, *Appl. Phys. Lett.*, **113**, 183102 (2018).
199. Z. Islam, A. L. Paoletta, A. M. Monterrosa, J. D. Schuler, T. J. Rupert, K. Hattar, N. Glavin, and A. Haque, *Microelectron. Rel.*, **102**, 113493 (2019).
200. B. Wang, Z. Islam, A. Haque, K. Chabak, M. Snure, E. Heller, and N. Glavin, *Nanotechnology*, **29**, 3131LT01 (2018).
201. P. H. Carey, F. Ren, E. Flitsiyan, and S. J. Pearton, *ECS J. Solid State Sci. Technol.*, **9**, 065007 (2020).
202. O. Ochedowski, O. Osmani, M. Schade, B. K. Bussmann, B. Ban-d'Etat, H. Lebius, and M. Schleberger, "Graphitic nanostripes in silicon carbide surfaces created by swift heavy ion irradiation." *Nat. Commun.*, **5**, 3913 (2014).
203. Y. Zhang, R. Sachan, O. H. Pakarinen, M. F. Chisholm, P. Liu, H. Xue, and W. J. Weber, *Nat. Commun.*, **6**, 8049 (2015).
204. A. Debelle et al., *Phys. Rev. B Condens. Matter Mater. Phys.*, **86**, 100102(R) (2012).
205. M. Backman, M. Toulemonde, O. H. Pakarinen, and N. Juslin, *Comput. Mater. Sci.*, **67**, 261 (2013).
206. D. Szalkai, Z. Galazka, K. Irmscher, P. Tüttő, A. Klix, and D. Gehre, *IEEE Trans. Nucl. Sci.*, **64**, 1574 (2017).
207. J. Yang, F. Ren, S. J. Pearton, G. Yang, J. Kim, and A. Kuramata, *J. Vac. Sci. Technol. B*, **35**, 031208 (2017).
208. P. Hazdra, P. Smrkovský, J. Vobecký, and A. Mihaila, *IEEE Trans Electron Dev.*, **68**, 202 (2021).



209. A. Akturk, J. M. McGarrity, N. Goldsman, D. J. Lichtenwalner, B. Hull, D. Grider, and R. Wilkins, *IEEE Trans. Nuclear Sci.*, **66**, 1828 (2019).
210. K. Niskanen, A. D. Touboul, R. Coq Germanicus, A. Michez, A. Javanainen, F. Wrobel, J. Boch, V. Pouget, and F. Saigné, *IEEE Trans Nuclear Sci*, **67**, 1365 (2020).
211. S. Cao, Q. Yu, H. Wang, Y. Sun, H. Lv, B. Mei, Morigen, P. Li, H. Zhang, and M. Tang, "Radiation effects on silicon carbide junction Barrier Schottky diodes caused by high energy proton." 2020 IEEE 5th International Conference on Integrated Circuits and Microsystems (ICICM), p. 81 (2020), (10.1109/ICICM50929.2020.9292288).
212. J. Lee, E. Flitsiyen, L. Chernyak, S. Ahn, F. Ren, L. Yuna, S. J. Pearton, J. Kim, B. Meyler, and J. Salzman, *ECS J. Solid State Sci. Technol.*, **6**, Q3049 (2017).
213. S. Ahn et al., *J. Vac. Sci. Technol.*, **B34**, 041213 (2016).
214. E. Wendler, E. Treiber, J. Baldauf, S. Wolf, and C. Ronnig, *Nucl. Instr. Methods in Physics Res.*, **B379**, 85 (2016).
215. A. A. Arehart, E. Farzana, T. E. Blue, and S. A. Ringel, *Presented at 2nd International Workshop on Ga2O3 and Related Materials*, Parma, Italy, September 2017.
216. H. Gao et al., *Appl. Phys. Lett.*, **112**, 242102 (2018).
217. H. J. von Bardeleben, S. Zhou, U. Gerstmann, D. Skachkov, W. R. L. Lambrecht, Q. Duy Ho, and P. Deak, *APL Mater.*, **7**, 022521 (2019).
218. G. Yang, S. Jang, F. Ren, S. J. Pearton, and J. Kim, *ACS Appl. Mater. Interfaces*, **9**, 40471 (2017).
219. J. Yang et al., *J. Vac. Sci. Technol. B*, **35**, 051201 (2017).
220. M. E. Ingebrigtsen, A. Y. Kuznetsov, B. G. Svensson, G. Alfieri, A. Mihaila, U. Badstübner, A. Perron, L. Vines, and J. B. Varley, *APL Mater.*, **7**, 022510 (2019).
221. B. E. Kananen, L. E. Halliburton, K. T. Stevens, G. K. Foundos, K. B. Chang, and N. C. Giles, *Appl. Phys. Lett.*, **110**, 202104 (2017).
222. F. Tuomisto, A. Karjalainen, V. Prozheeva, I. Makkonen, G. Wagner, and M. Baldini, "Oxide-based materials and devices X." ed. D. J. Rogers et al. *Proc. of SPIE*, **10919**, 1091910.
223. E. Korhonen, F. Tuomisto, D. Gogova, G. Wagner, M. Baldini, Z. Galazka, R. Schewski, and M. Albrecht, *Appl. Phys. Lett.*, **106**, 242103 (2015).
224. B. E. Kananen, N. C. Giles, L. E. Halliburton, G. K. Foundos, K. B. Chang, and K. T. Stevens, "Self-trapped holes in  $\beta$ -Ga<sub>2</sub>O<sub>3</sub> crystals." *J. Appl. Phys.*, **122**, 215703 (2017).
225. A. Y. Polyakov, N. B. Smirnov, I. V. Shchemerov, S. J. Pearton, F. Ren, A. V. Chernykh, P. B. Lagov, and T. V. Kulevoy, *APL Mater.*, **6**, 096102 (2018).
226. A. Janotti and C. G. Van de Walle, *Nat. Mater.*, **6**, 44 (2007).
227. A. Y. Polyakov, N. B. Smirnov, I. V. Shchemerov, D. Gogova, S. A. Tarelkin, and S. J. Pearton, *J. Applied Phys.*, **123**, 115702 (2018).
228. P. D. C. King and T. D. Veal, *J. Phys. Condens. Matter*, **23**, 334214 (2011).
229. S. Ahn, F. Ren, E. Patrick, M. E. Law, S. J. Pearton, and A. Kuramata, *Appl. Phys. Lett.*, **109**, 242108 (2016).
230. J. M. Johnson et al., *Phys. Rev. Mater.* (2020).
231. A. Kyrtos, M. Matsubara, and E. Bellotti, *Phys. Rev. B*, **95**, 245202 (2017).
232. S. Ahn, F. Ren, E. Patrick, M. E. Law, and S. J. Pearton, *ECS J. Solid State Sci. Technol.*, **6**, Q3026 (2017).
233. P. Weiser, M. Stavola, W. B. Fowler, Y. Qin, and S. Pearton, *Appl. Phys. Lett.*, **112**, 232104 (2018).
234. A. Luchechko, V. Vasylytsya, L. Kostyka, O. Tsvetkova, and A. I. Popovb, *Nuclear Inst. and Methods in Physics Research B*, **441**, 12 (2019).
235. A. Y. Polyakov et al., *APL Mater.*, **7**, 061102 (2019).
236. A. Y. Polyakov et al., *J. Phys. D*, **53**, 445111 (2020).
237. T. Roy et al., *Appl. Phys. Lett.*, **99**, 203501 (2011).
238. N. E. Ives, J. Chen, A. F. Witulski, R. D. Schrimpf, D. M. Fleetwood, R. W. Bruce, M. W. McCurdy, E. X. Zhang, and L. W. Massengill, *IEEE Trans. Nucl. Sci.*, **62**, 2417 (2015).
239. M. J. Martinez, M. P. King, A. G. Baca, A. A. Allerman, A. A. Armstrong, B. A. Klein, E. A. Douglas, R. J. Kaplar, and S. E. Swanson, *IEEE Trans Nuclear Sci*, **66**, 344 (2019).
240. A. Y. Polyakov, N. Smirnov, A. Govorkov, A. Markov, N. Kolin, V. Baikov, D. Merkurisov, and S. J. Pearton, *J. Vac. Sci. Technol.*, **B24**, 1094 (2006).
241. M. H. Wong, A. Takeyama, T. Makino, T. Ohshima, K. Sasaki, A. Kuramata, S. Yamakoshi, and M. Higashiwaki, *Appl. Phys. Lett.*, **112**, 023503 (2018).
242. S. Buchner et al., *IEEE Trans. Nucl. Sci.*, **59**, 988 (2012).
243. S. P. Buchner, F. Miller, V. Pouget, and D. P. McMorro, *IEEE Trans. Nucl. Sci.*, **60**, 1852 (2013).
244. J. Kim, S. J. Pearton, C. Fares, J. Yang, F. Ren, S. Kim, and A. Y. Polyakov, *J. Materials Chem., C*, **7**, 10 (2018).
245. N. Donato, N. Rouger, J. Pernot, G. Longobardi, and F. Udrea, *J. Phys. D: Appl. Phys.*, **53**, 093001 (2020).
246. R. S. Sussmann, *CVD Diamond for Electronic Devices and Sensors* (Wiley, New York, NY) 26 (2009).
247. L. Bäni et al., *Sensors*, **20**, 6648 (2020).
248. J. T. Buchan, M. Robinson, H. J. Christie, D. L. Roach, D. K. Ross, and N. A. Marks, *J. Appl. Phys.*, **117**, 245901 (2015).
249. L. Bäni, A. Alexopoulos, M. Artuso, F. Bachmair, M. Bartosik, H. Beck, V. Bellini, and V. Belyaev, *B. Bentel. J. Phys. D Appl. Phys.*, **52**, 465103 (2019).
250. The RD42 Collaboration et al., *Nucl. Phys. B Proc., Suppl.*, **78**, 675 (1999).
251. J. F. Prins, *Diamond Relat. Mater.*, **9**, 1275 (2000).
252. J. W. Tsung, M. Havranek, F. Hügging, H. Kagan, H. Krüger, and N. Wermes, *J. Instrum.*, **7**, P09009 N (2012).
253. S. Baccaro et al., *IEEE Trans. Nuclear Sci*, **65**, 2046 (2018).
254. M. Guthoff, W. de Boer, and S. Müller, *Nucl. Instruments Methods Phys. Res. Sect. A Accel. Spectrometers Detect. Assoc. Equip.*, **2014**, 735223N (2014).
255. S. Seidel, *J. Instrumentation*, **9**, C01013 (2014).
256. A. Mainwood, M. Newton, and B. Campbell, "The mechanisms of radiation damage of diamond, presented at." *1st Workshop on Radiation Hard Semiconductor Devices for Very High Luminosity Colliders, November, 2001* (CERN), 28, <https://ssd-rd.web.cern.ch/rd/default.htm>.
257. A. Mainwood and A. M. Stoneham, *J. Phys. Condens. Matter*, **9**, 2453 (1997).
258. B. Campbell, W. Choudhury, A. Mainwood, M. Newton, and G. Davies, *Nuclear Instr. Meth. In Physics Research Section A, Accelerators, Spectrometers, Detectors and Associated Equipment.*, **476**, 680 (2002).
259. B. Campbell and A. Mainwood, *Phys. Stat Solidi A.*, **181**, 99 (2000).
260. W. Adam, E. Berdermann, P. Bergonzo, G. Bertuccio, and M. Zoeller, *Nucl. Instr. Meth. In Physics Res.*, **476**, 686 (2002).
261. A. Oh et al., "Latest results on radiation tolerance of diamond detectors." *39th International Conference on High Energy Physics*, Seoul, South Korea Jul 2018 p. 597.
262. M. Zou, J. Bohon, J. Smedley, J. Distel, K. Schmitt, R.-Y. Zhu, L. Zhang, and E. M. Muller, *AIP Adv.*, **10**, 025004 (2020).
263. V. A. Nikolaenko, E. A. Krasikov, and A. D. Amayev, *At Energy*, **114**, 122 (2013).
264. A. A. Martin, J. Filevich, M. Straw, S. Randolph, A. Botman, I. Aharonovich, and M. Toth, *ACS Appl. Mater. Interfaces*, **945**, 39790 (2017).
265. S. M. Horszowski, *Radiat. Eff.*, **30**, 213 (1976).
266. S. R. Messenger, E. A. Burke, R. J. Walters, J. H. Warner, and G. P. Summers, *Prog. Photovolt. Res. Appl.*, **13**, 115 (2005).
267. M. W. Dale, "Color centers on demand in diamond." *PhD Thesis*, University of Warwick (2015), <http://wrap.warwick.ac.uk/80044/>.
268. N. Simosa, Z. Kotsinad, D. Sprouster, Z. Zhonga, H. Zhongb, and P. Hurh, *Nucl. Instrum. Methods Phys. Res., Sect. B*, **479**, 110 (2020).
269. Y. V. Borodin, D. S. Ermolaev, V. Pak, and K. Zhang, *3Mater. Sci. Eng.*, **110**, 012072 (2016).
270. A. V. Krashenninnikov and K. Nordlund, *J. Applied Phys*, **107**, 071301 (2010).
271. R. G. Klein, "Swift heavy ion irradiated boron nitride with and without the application of high pressure." *Dissertation*, Ruperto-Carola University of Heidelberg (Germany) (2010).
272. O. Lehtinen, E. Dumur, J. Kotakoski, A. V. Krashenninnikov, K. Nordlund, and J. Keinonen, *Nucl. Instrum. Methods Phys. Res. B*, **269**, 1327 (2011).
273. F. Cataldo and S. Iglesias-Groth, *J. Radioanal. Nucl. Chem.*, **313**, 1 (2017).
274. N. Simos, P. Hurth, N. Mokhov, and J. Hylen, Irradiation Effects on Graphite, C/C and BeNBI-2012, CERN, Geneva, [https://indico.cern.ch/event/193710/contributions/355782/attachments/279603/390994/NBI2012\\_Simos\\_et\\_al\\_NBI2012.pdf](https://indico.cern.ch/event/193710/contributions/355782/attachments/279603/390994/NBI2012_Simos_et_al_NBI2012.pdf).
275. D. Chen et al., *IEEE Trans Nuclear Sci*, **58**, 2983 (2011).
276. K. Nordlund and S. O. Kucheyev, "Ion-beam modification of semiconductors." *Characterization and Control of Defects in Semiconductors*, ed. Filip Tuomisto (IET, Oxford) (2019).
277. Y. Zhang and W. J. Weber, *Appl. Phys. Rev.*, **7**, 041307 (2020).
278. L. Nuckols, M. L. Crespillo, C. Xu, E. Zarkadoulou, Y. Zhang, and W. J. Weber, *Acta Mater.*, **199**, 96 (2020).
279. W. J. Weber and Y. Zhang, *Curr. Opin. Solid State Mater. Sci.*, **23**, 100757 (2021).
280. D. J. Knipp, "Essential science for understanding risks from radiation for airline passengers and crews." *Space Weather*, **15**, 549 (2017).
281. W. K. Tobiska, "Global real-time dose measurements using the Automated Radiation Measurements for Aerospace Safety (ARMAS) system." *Space Weather*, **14**, 1053 (2016).
282. National Academies of Sciences, Engineering, and Medicine, *Testing at the Speed of Light: The State of U.S. Electronic Parts Space Radiation Testing Infrastructure* (The National Academies Press, Washington, DC) (2018).
283. NASA SBIR 2021 Phase I Solicitation Z1.06 Radiation-Tolerant High-Voltage, High-Power Electronics.
284. J.-M. Lauenstein, M. C. Casey, R. L. Ladbury, A. D. Topper, A. M. Phan, and H. S. Kim, "Space Radiation effects on SiC power device reliability." *to be published in the IEEE International Reliability Physics Symposium (IRPS) Proceedings*, March 2021 (2021).
285. K. Boomer, L. Scheick, and A. Hammoud, Body of knowledge for GaN Power Electronics, NASA Electronic Parts and Packaging (NEPP) Program Office of Safety and Mission Assurance, November 9, 2020, <https://nepp.nasa.gov/docs/tasks/281-Wide-Bandgap-Reliability-and-Application-Guidelines/NEPP-BOK-2020-Boomer-Gallium-Nitride-Power-Electronics-20205007412.pdf>.
286. L. Scheick, "GaN HEMT power applications: the road to space qualification." *Proc. 9th NASA Electronic Parts and Packaging (NEPP) Program Electronic Technology Workshop*, June 20, 2018, Greenbelt Maryland.
287. J. R. Scarpulla and C. M. Gee, Guidelines for Space Qualification of GaN HEMT Technologies, Aerospace Corp. Report TOR-2018-00691, Rev A, March 2020.
288. G. D. Samolyuk, Y. N. Osetsky, and R. E. Stoller, *J. Nuclear Mater.*, **465**, 83 (2015).
289. F. Gao, H. Xiao, X. Zu, M. Posselt, and W. J. Weber, *Phys. Rev. Lett.*, **103**, 027405 (2009).
290. F. Gao and W. J. Weber, *Nucl. Instr. Meth. In Physics Research B*, **191**, 504 (2002).
291. E. Zarkadoulou, G. Samolyuk, Y. Zhang, and W. J. Weber, *J. Nuclear Materials*, **540**, 152371 (2020).
292. J. Xi, B. Liu, Y. Zhang, and W. J. Weber, *J. Appl. Phys.*, **123**, 045904 (2018).
293. H. Y. Xiao, F. Gao, X. T. Zu, and W. J. Weber, *J. Appl. Phys.*, **105**, 123527 (2009).
294. H. Y. Xiao, X. T. Zu, F. Gao, and W. J. Weber, *J. Appl. Phys.*, **103**, 123529 (2008).

- 295. J. Chen, E. X. Zhang, C. X. Zhang, M. W. McCurdy, D. M. Fleetwood, and R. D. Schrimpf, *IEEE Trans Nuclear Science*, **61**, 2959 (2014).
- 296. Z. Zhang et al., *J. Appl. Phys.*, **119**, 165704 (2016).
- 297. R. Jiang et al., *IEEE Trans Nuclear Science*, **64**, 218 (2016).
- 298. Z. Zhang et al., *J. Applied Physics*, **118**, 155701 (2015).
- 299. S. Ahn et al., *J. Vac. Sci. Technol. B*, **33**, 051208 (2015).
- 300. B. J. Kim, Y. H. Hwang, S. Ahn, F. Ren, S. J. Pearton, and J. Kim, *J. Vac. Sci. Technol. B*, **33**, 051215 (2015).
- 301. J. M. Osheroff, J.-M. Lauenstein, and R. L. Ladbury, *IEEE Trans Nuclear Sci.* (2021).